THE INTERACTION BETWEEN TOROIDAL SWIMMERS IN STOKES FLOW

AN ABSTRACT
SUBMITTED ON THE THIRTEENTH DAY OF JUNE, 2014
TO THE DEPARTMENT OF MATHEMATICS
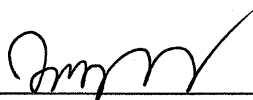OF THE GRADUATE SCHOOL OF
TULANE UNIVERSITY
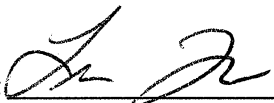IN PARTIAL FULFILLMENT OF THE REQUIREMENTS
FOR THE DEGREE OF
DOCTOR OF PHILOSOPHY
BY

_____

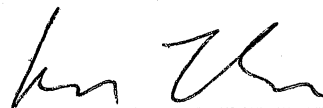JIANJUN HUANG

APPROVED: _____
LISA FAUCI, PH.D.
CHAIRMAN

_____
RICARDO CORTEZ, PH.D.

_____
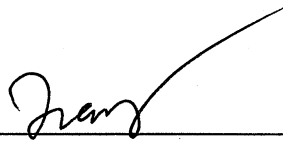JAMES HYMAN, PH.D.

_____
MORRIS KALKA, PH.D.

_____
KUN ZHAO, PH.D.

Abstract

The focus of this research has been devoted to study the interaction between two or more self-propelled toroidal swimmers in Stokes flow by applying the method of regularized Stokeslets and also study the effect of a nearby wall to the movement of a helical ring by using the method of regurlarized Stokeslets with images. In the study of the interaction between two or more toroidal swimmers, we interpret these as three-dimensional, zero Reynolds number analogues of finite vortex dipoles in an ideal fluid. Then, we examine the stability of relative equilibria that can form for these swimmers when they are initially placed in tandem or abreast. In addition, we examine the dynamics of the torus when a spherical cell body is placed at its center. This gives us an insight into the mechanical role of the transverse flagellum of dinoflagellates. Moreover, we show that the torus with a sphere moves more efficiently than one without. Lastly, we model the transverse flagellum of a dinoflagellate as a helical ring and study the effect of a nearby wall on its movement. The numerical results show that the wall baffles the movement of the helical ring, which is consistent with the phenomenon of sperm accumulation near surfaces.

THE INTERACTION BETWEEN TOROIDAL SWIMMERS IN STOKES FLOW

A DISSERTATION
SUBMITTED ON THE THIRTEENTH DAY OF JUNE, 2014
TO THE DEPARTMENT OF MATHEMATICS
OF THE GRADUATE SCHOOL OF
TULANE UNIVERSITY
IN PARTIAL FULFILLMENT OF THE REQUIREMENTS
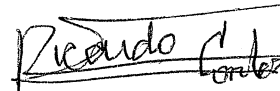FOR THE DEGREE OF
DOCTOR OF PHILOSOPHY
BY

_____

JIANJUN HUANG

APPROVED: _____
LISA FAUCI, PH.D.
CHAIRMAN

_____
RICARDO CORTEZ, PH.D.

_____
JAMES HYMAN, PH.D.

_____
MORRIS KALKA, PH.D.

_____
KUN ZHAO, PH.D.

Acknowledgments

I would like to dedicate this dissertation to my parents, Qingyuan Huang and Meiping Lu, who believed in my capabilities and gave me unconditional support and freedom to fly without a shadow. I would like to thank my brother, Jiansheng Huang, and my sister, Linli Huang, for their continued love and support to our family and me. It is because of you that I have the courage and the confidence to overcome all odds in life. I am extremely thankful to my advisor Dr. Lisa Fauci for her continued guidance, help and encouragement in research. Without her, I would have been lost in the forest of the science. I would also like to thank Dr. Ricardo Cortez and Dr. James Hyman for their insightful comments on the research. I also appreciate the financial support provided by the Mathematics department for the duration of my study. I would like to thank Dr. Hoa Nguyen for her assistance and guidance in the third year of my graduate study. To Dr. Jacek Wrobel, I feel so glad to have known you at Tulane and I am so appreciative for your patience everytime I bother you with my troubles. I also appreciate the help from Dr. Hideki Fujioka with my C++ codes and his guidance in programming. Lastly, I want to thank Ms. Geralyn, Pam and Mr. Mark Brown for their help and encouraging conversations. For proofreading, I also want to thank Dr. Lisa Fauci, Dr. Ricardo Cortez and Dr. Jeremy Dewar. Lastly, many thanks to all my friends, it is you guys that make my life in New Orleans so interesting and so fruitful.

Contents

Chapter 1

Introduction

Plankton are divided into three functional groups, phytoplankton, zooplankton and bacterioplankton. These microorganisms move around due to both their self motilities and the ocean current, and they form an essential part of the oceanic ecosystem. They provide a crucial source of food to many large aquatic animals. However, the bloom of some microorganisms in the ocean may be harmful to the oceanic ecosystem because of toxin production, which kills marine life and also could be passed on to humans who consume them. Among the plankton, there is one special type of phytoplankton called dinoflagellates, which are unicellular micoorganisms notorious for causing the "red tide" phenomenon in coastal region of the ocean.

Dinoflagellates [1–7] swim due to two flagella, a transverse flagellum and a longitudinal flagellum. The transverse flagellum emanates from the cell body's midsection, and wraps around the cell like a belt inside a furrow on the body. It beats counterclockwise when seen from the cell apex, which rotates the cell body but also acts as a forward-propelling device [3, 6, 7]. The longitudinal flagellum trails behind the cell body, much like a sperm flagellum. The longitudinal flagellum beats sinusoidally and propels the body forward, but also behaves as a rudder [6] to steer the direction of the dinoflagellate. Although it was observed that dinoflagellates move up-

wards without a longitudinal flagellum, Gaines & Taylor in [3], Cachon et al. in [4], and Fenchel in [5] still asserted that the tranverse flagellum only produces torque. Miyasaka et al. in [6] used resistive force theory and found that 'The transverse flagellum works as a propelling device that provides the main driving force or thrust to move the cell along the longitudinal axis of its helical swimming path'. Recent research [7] examined the motility of a helical ring as a model of a dinoflagellate transverse flagellum, and suggested that an even simpler model would be the rotating torus. This simplication can be easily understood from the fact that as the number of pitches of the helical ring increases, the helical ring would be more like a torus. Therefore, the simpler model, a torus whose surface is rotating, will be of interest in analyzing the function of the transverse flagellum of dinoflagellate, along with its hydrodynamical interaction of a pair of dinoflagellates.

The cross-sectional rings of a torus are centered about a circle of larger radius. We imagine that each cross section is rotating along the centerline circle at constant angular velocity. G. I. Taylor proposed this mechanism as an idealized non-reciprocal swimmer in Stokes flow [8]. He described this possibility as a rubber ring threaded on a solid cylinder. Purcell [9] later proposed this toroidal swimmer in his famous lecture "Life at low Reynolds number" as a mechanism which breaks the time-reversal symmetry, resulting in net movement. After G.I. Taylor [8] and Purcell [9], an approximation to the analytical solution to the Stokes equations outside a rotating torus with constant angular velocity was given by A.T. Chwang and W. Hwang in [10], with linear order in slenderness, which is defined as the ratio between the radius of the tube of the torus and the radius of the centerline circle of the torus. The slenderness ratio sometimes is presented by its reciprocal named aspect ratio. Then the result in [10] was improved by R.M. Thaokar et al. [11] with quadratic order in slenderness.

Boundary integral methods are then used to study larger slenderness ratios [11]. Recently, a rigorous theory of propulsion of the toroidal swimmer has been given by L.A. Leshansky and O. Kenneth [12]. The swimming speed and hydrodynamic efficiency were determined from the exact solution of the Stokes equation outside a toroidal swimmer.

Although it has an idealized geometry, the toroidal swimmer can give insight to many aspects of microorganism motility. First, a bacterial flagellum, such as E. Coli, rotates with a rotary motor in or within the cell wall. The study of the motion of such rotating flagella, tracing out a cylindrical shape, would be similar to the motion of a rotating torus [10]. Moreover, the rotating torus appoximates the waving action of a dinoflagellate transverse flagellum. Secondly, the stiff and semiflexible polymer rings such as DNA mini-plasmid, shaped like a torus, should be best modeled as a torus [13]. Lastly, nanomachines shapped like a torus as an artificial robot [13] could potentially be inserted into the arteries, digestive system, etc. to transmit images, deliver microscopic payloads to parts of the body or perform minimally invasive microsurgeries outside the reach of existing technologies [12].

The presence of nearby surfaces, in both biological settings and microfluidic devices, affects microorganism motility. In reproductive biology, the phenomenon of spermatozoa surface accumulation was obseved in 1886 [14]. Then, Rothschild [15] asserted, through the study of bull spermatozoa, that the accumulation is caused by hydrodynamic interaction rather than by chemical interaction. From this point of view, studying the hydrodynamic interaction between microorganisms could shed light on some phenonomena in biology. Moreover, in order to study the movement of microorganisms and their effect on the oceanic environment, the hydrodynamic

interactions between collections of microbes should be examined. Smith [16] applied finite element methods to illustrate the surface accumulation behavior of spermatozoa.

The hydrodynamic interaction of swimming microorganisms has been an active area of research [17–19]. Here we focus on the details of the interaction between two toroidal swimmers. In the past half century, several methods have been used to study the hydrodynamic interaction of two swimming microorganisms. Stokesian-dynamic simulations are used to study the particle stress tensor or diffusion tensor of inert spheres [20–25]. In Stokesian-dynamics, the motility matrix and the inverted motility matrix are essential to study the force, torque and stress of interacting objects. Ishikawa et al. used boundary element methods to study the interactions between two bottom-heavy squirmers in Stokes flow [18] and the interaction of two swimming Paramecia [19]. The boundary integral method [26] has been used to study the interaction of two rotating tori in Stokes flow [27]. Analytically, Faxen relations are used to analyze the far-field flow properties [18], and lubrication theory is applied to show the near-field flow properties [18]. Here we use the method of regularized Stokeslets [28], which couples regularized surface forces with the Stokesian fluid. Our numerical results will be validated by comparison with previous analytic solutions [12].

In order to model the dinoflagellate and to study their hydrodynamic interactions, several assumptions have been made. First, the flow around the swimming body is taken to be the incompressible Stokes flow. This assumption is reasonable because of the microorganism's small size, about $1 - 500\mu m$, and slow moving speed, up to several hundred $\mu m/s$. The small Reynold number (10^{-2}) allows us to treat the flow as the quasi-static, time reversable flow or Stokes flow. Secondly, the body of the dinoflagellate is assumed to be a sphere. Although its shape might change in

different species or in different stages, this assmuption is made only for mathematical convenience. Thirdly, in the force free case, mentioned hereafter, the swimming body is assumed to exert zero net force and zero net torque instantaneously, which implies that there is no external forces other than force from fluid exerted on the body to cause the rigid translation and rigid rotation of the object. Lastly, as mentioned in [18], no gravitational force will be taken into consideraton since its sedimentary velocity is much less than its translational velocity.

Using our simplified model, we hope to gain insight in the interaction of dinoflagellates. In [27], the interaction of co- and counter-rotating tori in a viscous flow have been studied both analytically and numerically. Thaokar gives the approximated analytical solution for the slender torus and far field limit, and then extends it to the non-slender torus and small separation by implementing a boundary integral method [26]. However, only axisymmetric arrangements of the two tori are considered where other configurations, such as two tori kept abreast, or staggered tori without alignment are not considered. Here, "alignment" means the line connecting two centers of the tori is parallel to the normal of each torus, which is the unit vector perpendicular to the plane of the centerline. Here we investigate these arrangements as well as the interaction of three tori. We also give intuitive explanations for the dynamics of the observed moving pattern of tori.

In this thesis, we give an overview in Chapter 2 of mathematical and numerical tools needed to examine the toroidal swimmers. We present notations, the method of regularized Stokeslets, the method of regularized Stokeslets with images, some matrices related to rigid rotation and a distance-preserving numerical scheme. We also discuss the formulation of finite vortex dipole in two dimensional space, since the

interaction between finite vortex dipoles in a 2D ideal fluid is qualitatively related to the interaction of toroidal swimmers in a 3D viscous fluid. Chapter 3 will concentrate on the study of the interaction between two toroidal swimmers and modeling the motility of dinoflagellate. Moreover, we will also show the similarity of interaction patterns of 2D finite vortex dipoles and of tori. In Chapter 4, several models of dinoflagellates will be examined. The efficiency of each model will be studied and the effect of a nearby wall on the movement of a helical ring in Stokes flow will be discussed by applying the method of regularized Stokeslet with images. Lastly, we summarize our main results in Chapter 5 and discuss the future work in Chapter 6.

Chapter 2

Model and Methods

2.1 Introduction

The self-propulsion of an idealized toroidal swimmer was first discussed by G.I. Taylor in his classic paper [8] of 1952. Also, a torus is a simple model of the transverse flagellum of a dinoflagellate. The shape of a torus resembles a donut, and is formed by rotating a small circle about an axis, where both the circle and the axis are coplanar. The radius of the circle, denoted by r_h, is called the **radius of the tube**, the trajectory of the center of the circle after the rotation along the line is called the **centerline of the torus**, and the **radius of the centerline** is denoted by r_c. On the surface of each torus, we impose a fixed rotational velocity $\mathbf{u}_0$ about the centerline. The **normal vector** of the torus $\mathbf{n}$ lies in parallel with the axis perpendicular to the centerline plane. We choose the direciton of the normal vector $\mathbf{n}$ by the direction of the velocity at the inner surface of the torus. An illustration of the torus with surface tangential velocity $\mathbf{u}_0$ is shown in figure 2.1.

Because the length and speed scales at the microscopic level are so small, the fluid dynamics of microorganisms are governed by the Stokes equations with
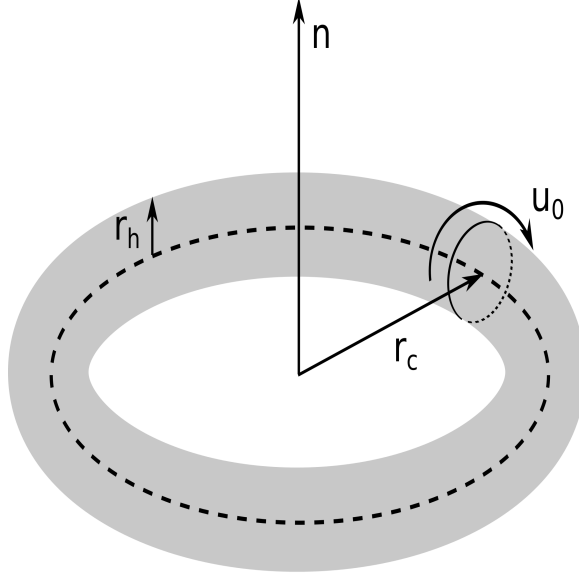
Figure 2.1: A schematic diagram of the rotating torus with radius of the tube r_h, radius of the centerline r_c, normal direction $\mathbf{n}$ and surface tangential velocity $\mathbf{u}_0$. The dashed line is the centerline of the torus.

dimensionless formulation (see section 2.3):

$$-\nabla p + \Delta \mathbf{u} + \mathbf{f} = 0$$
$$\nabla \cdot \mathbf{u} = 0$$

(2.1)

In general, $\mathbf{u}$ is the fluid velocity, p is pressure and $\mathbf{f}$ represents the external force. The force $\mathbf{f}$ comes from the surface force of the immersed microorganisms. When the force is taken to be a point force with direction and magnitude $\mathbf{f}_0 = (f_1, f_2, f_3)$ at $\mathbf{x}_0$ i.e. $\mathbf{f} = \mathbf{f}_0 \delta(\mathbf{x} - \mathbf{x}_0)$, the velocity field due to the point force in three dimensional space is:

$$u_i(\mathbf{x}) = \frac{1}{8\pi} S_{ij}(\mathbf{x}, \mathbf{x}_0) f_j$$

(2.2)

where $S_{ij}(\mathbf{x}, \mathbf{x}_0) = \frac{\delta_{ij}}{r} + \frac{\tilde{x}_i \tilde{x}_j}{r^3}$, is called the Stokeslet (see [29] or section 2.4), δ_{ij} is the Kronecker delta, $r = |\mathbf{x} - \mathbf{x}_0|$ and $\tilde{x}_i = x_i - x_{0,i}$. The formula (2.2) is given according

to the Einstein summation convention (see section 2.2). This Stokeslet S_{ij} can be used to represent the fluid velocity due to forces applied on the surface ∂D of an object D using the boundary integral formulation (see [26] and section 2.5):

$$u_i(\mathbf{x}) = \frac{1}{8\pi} \int_{\partial D} S_{ij}(\mathbf{x}, \mathbf{y}) \tilde{f}_j(\mathbf{y}) dS(\mathbf{y}) \tag{2.3}$$

where $\tilde{\mathbf{f}} = (\tilde{f}_1, \tilde{f}_2, \tilde{f}_3)$ are the differences between the outer surface forces and the inner surface forces of a rigid body. The integrand of the solution, however, is singular at the spatial points where the forces are applied. In my research, I choose a regularized Stokeslet formulation where, rather than Dirac point forces $\mathbf{f}_0 \delta(\mathbf{x} - \mathbf{x}_0)$, I consider regularized forces $\mathbf{f}_0 \psi_d(\mathbf{x} - \mathbf{x}_0)$, where $\psi_d(\mathbf{x} - \mathbf{x}_0)$ is a blob function centered at $\mathbf{x}_0$ with blob size d. A specific blob function from [29] is shown in formula (2.20). The boundary integral formulation (see section 2.5) of the solution to Stokes equation (2.1) with these regularized forces is given :

$$\int_{\mathbb{R}^3} u_j(\mathbf{y}) \psi_d(\mathbf{x} - \mathbf{y}) d\mathbf{y} = \frac{1}{8\pi} \int_{\partial D} S_{ij}^d(\mathbf{x}, \mathbf{y}) \tilde{f}_i dS(\mathbf{y}) \tag{2.4}$$

where S_{ij}^d corresponding to the specific blob function is the reguralized Stokeslet [29]. A specific regularized Stokeslet derived in [29] for a given blob function (shown in formula 2.20) will be presented in Section 2.4.

Two models of viscous flow around a torus have been studied [12]: The **toroidal glider** and the **force free** torus. The toroidal glider, which is equivalent to the well-known problem of the axisymmetric flow past a rigid body, models the rigid object immersed in the fluid moving due to the stress from the surrounding fluid and the external forces. However, the surface force in the force free case, sometimes called propulsion velocity case, is assumed to ensure the conservation of linear

and angular momentum, which guarantee that no external force is causing the rigid translation and rotation of the immersed body.

In this thesis, we study the toroidal glider, where the torus is dragged through the fluid at a specified velocity. Then the drag force will be found. For the force free case, with prescibed surface tangential velocity, the torus will move and rotate under the fluid-torus interaction. In a third model, we fix the position of the torus and at the same time let the surface of the torus rotate along its centerline. We calculate the force needed to keep it unmoved. We will show that the last model actually is a combination of the toroidal glider and the force free case in a certain way.

The discretization of the right hand side of the equation (2.4) with N points and a regularization approximation of its left hand side result in $3N$ equations simply expressed as

$$\mathbb{L}(\mathbf{f}) = \mathbf{u} \tag{2.5}$$

where $\mathbb{L}$ is a linear operator,

$$\mathbf{f} = (f_1^1, f_2^1, f_3^1, \cdots, f_1^N, f_2^N, f_3^N)^T$$

and

$$\mathbf{u} = (u_1^1, u_2^1, u_3^1, \cdots, u_1^N, u_2^N, u_3^N)^T.$$

Here f_j^i and u_j^i are the j-th $(j = 1, 2, 3)$ component of the surface force of the i-th $(i = 1, 2, \cdots, N)$ point and the j-th $(j = 1, 2, 3)$ component of the velocity of the i-th $(i = 1, 2, \cdots, N)$ point respectively. In the case that the velocity on the surface of the boundary $\mathbf{u}$ is known, the surface force $\mathbf{f}$ can be obtained immediately from

equation (2.5) by applying a linear equation solver, such as Gaussian elimination for general matrices, or an iterative method such as conjugate gradient, minimal residual or generalized minimal residual. In the cases of the free swimmer, the veolocity of the immersed object is given as $\mathbf{u} = \mathbf{u}_0 + \mathbf{U} + \mathbf{\Omega} \times \mathbf{x}$, where $\mathbf{u}_0$ is a given surface tangential velocity, $\mathbf{U}$ is the induced translational velocity from $\mathbf{u}_0$ and $\mathbf{\Omega}$ is the induced rotational velocity from $\mathbf{u}_0$. Here, we have an additional 6 unknowns: 3 unknowns from the translational velocity $\mathbf{U}$ and 3 unknowns from the rotational velocity $\mathbf{\Omega}$. The added six equations come from the constraints that the force free immersed boundary must exert zero net force and zero net torque instantaneously, i.e.

$$\int_{\partial D} \tilde{\mathbf{f}}(\mathbf{x})d\mathbf{x} = \mathbf{0} \quad \text{and} \quad \int_{\partial D} \mathbf{x} \times \tilde{\mathbf{f}}(\mathbf{x})d\mathbf{x} = \mathbf{0} \tag{2.6}$$

This conservation of linear and angular momentum in equation (2.6) gives 6 more equations after discretization and we balance the number of equations and the number of unknowns. The equations (2.5) together with the equations after the discretization of equation (2.6) can be presented as:

$$A\tilde{\mathbf{f}} = \tilde{\mathbf{u}} \tag{2.7}$$

Here, A is a $(3N + 6)$ by $(3N + 6)$ symmetric matrix, and

$$\tilde{\mathbf{f}} = (f_1^1, f_2^1, f_3^1, \cdots, f_1^N, f_2^N, f_3^N, \mathbf{U}, \mathbf{\Omega})^T$$

$$\tilde{\mathbf{u}} = (u_1^1, u_2^1, u_3^1, \cdots, u_1^N, u_2^N, u_3^N, 0, 0, 0, 0, 0, 0)^T$$

where f_j^i and u_j^i are the j-th ($j = 1, 2, 3$) components of the surface force of the i-th ($i = 1, 2, \cdots, N$) point and the j-th ($j = 1, 2, 3$) components of the velocity of the

i-th $(i = 1, 2, \cdots, N)$ point respectively. This equation will be solved numerically with an iterative method to find out the translational velocity $\mathbf{U}$ and the rotational velocity $\boldsymbol{\Omega}$ for specified surface velocities $\mathbf{u}_0$. Then, with the translational velocity $\mathbf{U}$ and rotational velocity $\boldsymbol{\Omega}$, the points $\mathbf{x}$ on the torus and the center of the torus $\mathbf{x}_c$ will be updated from the equations,

$$
\begin{aligned}
\mathbf{x}'(t) &= \mathbf{U}(t) + \boldsymbol{\Omega} \times (\mathbf{x} - \mathbf{x}_c) \\
\mathbf{x}_c'(t) &= \mathbf{U}(t)
\end{aligned}
\tag{2.8}
$$

which will be solved numerically with either Euler's method or Runge-Kutta methods. Details of solving equation (2.8) with a distance-preserving numerical scheme will be discussed in section 2.9.

2.2 Notations

A typical convention is to denote a vector in boldface, otherwise it is a scalar variable. For example, a vector $\mathbf{u}$ contains three components u_i $(i = 1, 2, 3)$, where each u_i is a scalar. Before introducing the product involving vectors and matrices, several notations are introduced in fluid mechanics to simplify the expressions or to avoid the use of transpose notation T in matrix calculus. First is the **repeated-index summation convention**, usually called **Einstein's summation convention**. This convention asserts that the repeated subscript in a term or a term involving products implies the summation over the repeated subscript. For example

$$
S_{ii} = \sum_i S_{ii} = \mathbf{Tr}(S)
$$

$$
S_{ij} f_j = \sum_j S_{ij} f_j
$$

Using the convention, if $\mathbf{u}$, $\mathbf{v}$ and $\mathbf{w}$ are vectors, the inner product is:

$$\mathbf{u} \cdot \mathbf{v} = u_i v_i,$$

the outer product is:

$$(\mathbf{u} \times \mathbf{v})_i = \varepsilon_{ijk} u_j v_k$$

and the triple product is:

$$\mathbf{u} \cdot (\mathbf{v} \times \mathbf{w}) = \varepsilon_{ijk} u_i v_j w_k$$

Here, ε_{ijk} is the alternating matrix , where $i, j, k = 1, 2, 3$, is defined as $\varepsilon_{ijk} = 0$ if any two indices are the same; $\varepsilon_{ijk} = 1$ if (i,j,k) is in cyclic order; Otherwise, $\varepsilon_{ijk} = -1$. The vector product

$$(\mathbf{uv})_{ij} = u_i v_j$$

is a two dimensional matrix with (i,j) entry equal to $u_i v_j$. For example, if $\mathbf{u} = (1, 0, 0)$, then

$$\mathbf{uu} = \begin{bmatrix} 1 & 0 & 0 \\ 0 & 0 & 0 \\ 0 & 0 & 0 \end{bmatrix}$$

More notations in fluid mechanics are shown in Appendix A of Pozrikidis' book [30].

2.3 Stokes equation

Newtonian flow is characterized by the continuity equation, which comes from the conservation of mass:

$$\rho_t + \nabla \cdot (\rho \mathbf{u}) = 0 \tag{2.9}$$

and the Navier-Stokes equation obtained from the conservation of momentum

$$\rho \left(\mathbf{u}_t + (\mathbf{u} \cdot \nabla)\mathbf{u} \right) = \nabla \cdot \sigma + \mathbf{f} \tag{2.10}$$

where $\mathbf{u}$ represents the flow velocity, ρ is the density and $\mathbf{f}$ is the external force respectively. σ is the stress tensor, which is a three dimensional symmetric matrix, and has the form

$$\sigma = -p\mathbf{I} + \lambda(\nabla \cdot \mathbf{u}) + \mu(\nabla\mathbf{u} + \nabla\mathbf{u}^T) \tag{2.11}$$

where p is the pressure, λ is the second coefficient of viscosity or called dilational viscosity coefficient and μ is the first coefficient of viscosity or called dynamic viscosity. $\nabla \cdot \sigma$ in equation (2.10) is a vector defined with its i-th component $(\nabla \cdot \sigma)_i = \frac{\partial \sigma_{ij}}{\partial x_j}$. Here we assume the density ρ to be a constant. Then the continuity equation (2.9) is:

$$\nabla \cdot \mathbf{u} = 0. \tag{2.12}$$

This equation is also called the incompressibility condition. The stress tensor is then

$$\sigma = -p\mathbf{I} + \mu(\nabla\mathbf{u} + \nabla\mathbf{u}^T), \tag{2.13}$$

which implies that the Navier-Stokes equation (2.10) will have the form

$$\rho \left(\mathbf{u}_t + (\mathbf{u} \cdot \nabla)\mathbf{u} \right) = -\nabla p + \mu \Delta \mathbf{u} + \mathbf{f} \tag{2.14}$$

We define a characteristic length L related to the size of the torus, a characteristic velocity U determined by the particular mechanism driving the flow, and a character-

istic time T that is either imposed by external forcing or simply defined as L/U [26]. Then, we scale the velocity by U, the length by L, the time by $T = L/U$, the pressure by P and the force by F, i.e. $\tilde{\mathbf{u}} = \frac{\mathbf{u}}{U}$, $\tilde{l} = \frac{l}{L}$, $\tilde{t} = \frac{t}{T}$, $\tilde{p} = \frac{p}{P}$ and $\tilde{\mathbf{f}} = \frac{\mathbf{f}}{F}$, the incompressibility condition becomes

$$\nabla \cdot \tilde{\mathbf{u}} = 0 \tag{2.15}$$

and from the Navier-Stokes equation (2.14),

$$
\begin{aligned}
\rho \frac{U^2}{L} \left(\tilde{\mathbf{u}}_t + (\tilde{\mathbf{u}} \cdot \nabla)\tilde{\mathbf{u}} \right) &= -\frac{P}{L}\nabla\tilde{p} + \mu\frac{U}{L^2}\Delta\tilde{\mathbf{u}} + F\tilde{\mathbf{f}} \\
\frac{\rho U L}{\mu} \left(\tilde{\mathbf{u}}_t + (\tilde{\mathbf{u}} \cdot \nabla)\tilde{\mathbf{u}} \right) &= -\frac{PL}{\mu U}\nabla\tilde{p} + \Delta\tilde{\mathbf{u}} + \frac{FL^2}{\mu U}\tilde{\mathbf{f}}
\end{aligned}
\tag{2.16}
$$

Let $\frac{PL}{\mu U} = 1$, $\frac{FL^2}{\mu U} = 1$ and $Re = \frac{\rho U L}{\mu}$, which is the Reynolds number, then the Navier-Stokes equation will turn out to be

$$Re\left(\tilde{\mathbf{u}}_t + (\tilde{\mathbf{u}} \cdot \nabla)\tilde{\mathbf{u}} \right) = -\nabla\tilde{p} + \Delta\tilde{\mathbf{u}} + \tilde{\mathbf{f}} \tag{2.17}$$

The Reynolds number Re expresses the magnitude of inertial convective forces relative to viscous forces. Instead of adding tilde to each variable, we still use originial variables for simplicity. As discussed in the introduction, microorganisms are small in size and also move with slow velocity, so the Reynold number will be small enough that the left hand side of the equation (2.17) can be set equal to 0. Such flow with low Reynolds number is referred to as Stokes flow, and the dimensionless equations to characterize the incompressible Stokes flow in three dimensions are:

$$-\nabla p + \Delta\mathbf{u} + \mathbf{f}(\mathbf{x}) = 0$$

$$\nabla \cdot \mathbf{u} = 0$$

where $\mathbf{u}$ represents the flow velocity, p is the pressure and $\mathbf{f}$ represents the external force. The advantage of the Stokes equations is that a linear relationship exists between velocity and forces. If the external force $\mathbf{f}$ is taken as a point force located at $\mathbf{x}_0$ i.e. $\mathbf{f}(\mathbf{x}) = \mathbf{f}_0 \delta(\mathbf{x} - \mathbf{x}_0)$, where $\mathbf{f}_0 = (f_1, f_2, f_3)$ is a constant force, the solution to the Stokes equation (2.1) in three-dimensional space is:

$$p(\mathbf{x}) = -\frac{\mathbf{f}_0 \cdot (\mathbf{x} - \mathbf{x}_0)}{4\pi r^3}$$
$$\mathbf{u}(\mathbf{x}) = \frac{\mathbf{f}_0}{8\pi r} + \frac{(\mathbf{f}_0 \cdot (\mathbf{x} - \mathbf{x}_0))(\mathbf{x} - \mathbf{x}_0)}{8\pi r^3}$$

$$(2.18)$$

where $r = |\mathbf{x} - \mathbf{x}_0|$. This velocity field also could be written as in equation (2.2).

$$u_i(\mathbf{x}) = \frac{1}{8\pi} S_{ij}(\mathbf{x}, \mathbf{x}_0) f_j$$

where $S_{ij}(\mathbf{x}, \mathbf{x}_0) = \frac{\delta_{ij}}{r} + \frac{\tilde{x}_i \tilde{x}_j}{r^3}$, is called the Stokeslet, δ_{ij} is the Kronecker delta, $r = |\mathbf{x} - \mathbf{x}_0|$ and $\tilde{x}_i = x_i - x_{0,i}$. Applying the notation introduced in section 2.2, it can also be represented as

$$\mathbf{u} = \frac{1}{8\pi r} \left(\mathbf{I} + \tilde{\mathbf{r}}\tilde{\mathbf{r}} \right) \mathbf{f}_0$$

where $\tilde{\mathbf{r}} = \mathbf{r}/r$, $\mathbf{r} = \mathbf{x} - \mathbf{x}_0$, and $r = |\mathbf{r}|$.

2.4 Method of regularized Stokeslets

The fundamental solution (2.18) to the Stokes equations is singular at the point $\mathbf{x}_0$ where the force is applied. These fundamental solutions will be integrated over a surface to be a solution to Stokes flow outside the surface. However, to evaluate an integral with a sigularity is not an easy task. The idea of the method of regularized Stokeslets is to replace the point forces by regularized forces concentrated at a point [28, 29]. Replacing $\mathbf{f}(\mathbf{x})$ by $\mathbf{f}_0 \psi_d(\mathbf{x} - \mathbf{x}_0)$ in equation (2.1), where $\psi_d(\mathbf{x})$ is

referred to as blob function, the solution will be

$$p(\mathbf{x}) = \mathbf{f}_0 \cdot \nabla G_d(|\mathbf{x} - \mathbf{x}_0|)$$

$$\mathbf{u}_s(\mathbf{x}) = (\mathbf{f}_0 \cdot \nabla)\nabla B_d(|\mathbf{x} - \mathbf{x}_0|) - \mathbf{f}_0 G_d(|\mathbf{x} - \mathbf{x}_0|) \tag{2.19}$$

where $\mathbf{u}_s$, $\mathbf{f}$ and p are velocity, external forces and pressure respectively, G_d satisfies $\Delta G_d = \psi_d(\mathbf{x})$ and B_d satisfies $\Delta B_d = G_d$. The subscript 's' is used to mark that the solution is related to 'Stokeslets', which will be discussed in detail with other concepts, like doublet, rotlet and stresslet, in section 2.6.

In [28, 29], a specific blob function used to derive the pressure and the velocity formula to the Stokes equation is chosen as:

$$\psi_d = \frac{15d^4}{8\pi(r^2 + d^2)^{7/2}} \tag{2.20}$$

Then, the corresponding Stokeslets with regularized point force will be given as

$$S_{ij}^d(\mathbf{x}, \mathbf{x}_0) = \delta_{ij}\frac{r^2 + 2d^2}{(r^2 + d^2)^{3/2}} + \frac{(\mathbf{x}_i - \mathbf{x}_{0,i})(\mathbf{x}_j - \mathbf{x}_{0,j})}{(r^2 + d^2)^{3/2}}$$

in three dimensional space [29]. Consequently, the velocity field will be given as

$$u_i = \frac{1}{8\pi}S_{ij}^d f_j \tag{2.21}$$

in three dimensional space.

2.5　Boundary integral methods

In order to introduce the boundary integral method [26], let D be the region occupied by the rigid body immersed in the fluid, $\mathbf{u}(\mathbf{x})$ is the flow velocity at position $\mathbf{x} = (x_1, x_2, x_3)$ in $\mathbb{R}^3$ and $\mathbf{f}(\mathbf{x})$ is the surface traction on the boundary ∂D of the domain D. Since the flow around the microorganism is characterized by the Stokes equation (2.1), the velocities $\mathbf{u}$ and the stress tensor σ to Stokes flow with boundary D satisfy the reciprocal identity,

$$\nabla \cdot (\mathbf{u} \cdot \sigma' - \mathbf{u}' \cdot \sigma) = 0 \tag{2.22}$$

where $\mathbf{u}'$ and σ' are another solutions to Stokes flow. Let $\mathbf{u}'$ be the solution to the Stokes equation due to point force $\mathbf{f}_0 \delta(\mathbf{x} - \mathbf{x}_0)$ in 3D, the formula of $\mathbf{u}'$ expressed in (2.21). Then the corresponding stress tensor σ' is

$$\sigma'_{ij} = \frac{1}{8\pi} T_{ijk}(\mathbf{x}, \mathbf{x}_0) f_k$$

where $T_{ijk} = -\frac{6 \hat{x}_i \hat{x}_j \hat{x}_k}{r^5}$. Plug $\mathbf{u}'$ and corresponding σ' into the reciprocal identity (2.22), then integrate it over domain D if the point force is not in the domain or integrate over domain D excluding the point $\mathbf{x}_0$ if it is in the domain, then the boundary integral formula gives:

$$u_j(\mathbf{x}) = -\frac{1}{8\pi} \int_{\partial D} S_{ij}(\mathbf{x}, \mathbf{y}) f_i dS(\mathbf{y}) + \frac{1}{8\pi} \int_{\partial D} u_i(\mathbf{y}) T_{ijk}(\mathbf{x}, \mathbf{y}) n_k dS(\mathbf{y}) \quad \text{if} \quad \mathbf{x} \in D \tag{2.23}$$

$$0 = -\frac{1}{8\pi} \int_{\partial D} S_{ij}(\mathbf{x}, \mathbf{y}) f_i dS(\mathbf{y}) + \frac{1}{8\pi} \int_{\partial D} u_i(\mathbf{y}) T_{ijk}(\mathbf{x}, \mathbf{y}) n_k dS(\mathbf{y}) \quad \text{if} \quad \mathbf{x} \notin \bar{D} \tag{2.24}$$

where surface force f_i is defined as $\sigma_{ik}n_k$. Assume that there is an external flow outside the domain D with the same boundary velocity as the inside flow and 0 at infinity, then the velocity in the domain D satisfies

$$0 = \frac{1}{8\pi}\int_{\partial D} S_{ij}(\mathbf{x},\mathbf{y})f_i'dS(\mathbf{y}) + \frac{1}{8\pi}\int_{\partial D} u_i(\mathbf{y})T_{ijk}(\mathbf{x},\mathbf{y})n_k dS(\mathbf{y}) \quad \text{if} \quad \mathbf{x} \in D \quad (2.25)$$

since the domain D is located outside of the external flow. Here, n_k is pointing outward of domain D. Subtracting the equation (2.25) from equation (2.23), we obtain

$$u_j(\mathbf{x}) = -\frac{1}{8\pi}\int_{\partial D} S_{ij}(\mathbf{x},\mathbf{y})\tilde{f}_i dS(\mathbf{y}) \tag{2.26}$$

where $\tilde{f}_i$ are the differences between the internal surface forces and the external surface forces. The solution (2.26), for an interior point $\mathbf{x}$, can be extended to boundary points (see section 2.3 in [26]). Take toroidal glider case for example, the velocity of the flow on the surface of the object is assumed to have the form $\mathbf{U} + \mathbf{\Omega} \times \hat{\mathbf{x}}$, and then the velocity field of the flow inside the domain D is:

$$u_j(\mathbf{x}) = -\frac{1}{8\pi}\int_{\partial D} S_{ij}(\mathbf{x},\mathbf{y})f_i dS(\mathbf{y}) \tag{2.27}$$

where the negative sign indicates f_i are surface tractions, which relates to the drag force $\mathbf{F} = (F_1, F_2, F_3)$ in the way that (see equation (1.2.7) in [26])

$$F_i = -\int_{\partial D} f_i(\mathbf{y})dS(\mathbf{y}). \tag{2.28}$$

Moreover, not only is this formula true inside of the domain D, it is true for all points outside with an opposite sign.

Applying the regularized Stokeslets (see equation (2.21)) and corresponding σ^d

as $\mathbf{u}'$ and σ' to the reciprocal equation (see equation (2.22)), and integrating over the domain D and domain $\bar{D}^C$ respectively, we find that we actually solve the following equations numerically (see [29]):

$$\int_{\mathbb{R}^3} u_j(\mathbf{y})\phi_d(\mathbf{x}-\mathbf{y})d\mathbf{y} = -\frac{1}{8\pi}\int_{\partial D} S_{ij}^d(\mathbf{x},\mathbf{y})\tilde{f}_i dS(\mathbf{y}) \tag{2.29}$$

where $\tilde{f}$ are the differences between interior surface forces and outer surface forces. The linear equations after discretization and regularization with N points in the toroidal glider case with given rotational velocity $\mathbf{\Omega}$ and translational velocity $\mathbf{U}$ we solving are

$$\mathbf{Af} = \mathbf{U} + \mathbf{\Omega} \times \mathbf{x} \tag{2.30}$$

for surface traction $\mathbf{f}$. In the force free case with boundary velocity $\mathbf{u}$ equal $\mathbf{u}_0 + \mathbf{U} + \mathbf{\Omega} \times \mathbf{x}$, where $\mathbf{u}_0$ is the velocity of a certain prescribed surface motion such as the surface rotation, we are solving

$$\mathbf{Af} = \mathbf{u}_0 + \mathbf{U} + \mathbf{\Omega} \times \mathbf{x} \tag{2.31}$$

for $\mathbf{f}$, $\mathbf{U}$ and $\mathbf{\Omega}$ with two more conditions from the discretiztion of the equations of the conservation of linear and angular momentum (2.6):

$$\sum_{i=1}^{N} \mathbf{f}_i = 0 \quad \text{and} \quad \sum_{i=1}^{N} \mathbf{x}_i \times \mathbf{f}_i = 0 \tag{2.32}$$

where $\mathbf{f}_i = (f_i^1, f_i^2, f_i^3)$ is the average surface force at $\mathbf{x}_i$, and

$$\mathbf{f} = (\mathbf{f}_1, \mathbf{f}_2, \cdots, \mathbf{f}_N)^T$$

Morevoer, for both cases, the accuracy is $O(\frac{\varepsilon^2}{d^3}) + O(d^q)$ with $q = 1$ at points near boundary, or $q = 2$ at points far away from the boundary [29]. Here, ε is the discretization size and d is the blob size. The velocity, in this paper, we evaluate is on the boundary, so the error accuracy is $O(\frac{\varepsilon^2}{d^3}) + O(d)$. Taking the blob size $d = O(\sqrt{\varepsilon})$, the expected order of accuracy in our case will be $1/2$.

2.6   Method of regularized Stokeslets with images

Many microorganisms swim near surfaces. Here we include the presence of an infinite planar wall, where the non-slip condition will be enforced. Assume the wall is located at $x = w$, which is a plane parallel to y-z plane. Then the Stokes equation in the right half space is expressed as follows:

$$
\begin{aligned}
-\nabla p + \mu \Delta \mathbf{u} + \mathbf{F}(\mathbf{x}) = 0 \quad & \mathbf{x} \in \mathbb{R}^3 \cap \{x > w\} \\
\nabla \cdot \mathbf{u} = 0 \quad & \mathbf{x} \in \mathbb{R}^3 \cap \{x > w\} \\
\mathbf{u} = 0 \quad & \mathbf{x} \text{ on } \{x = w\}
\end{aligned}
\tag{2.33}
$$

Before showing the solution to the equation (2.33) with point force at $\mathbf{x}_0$ with strength $\mathbf{f}$, i.e. $\mathbf{F} = \mathbf{f}\delta(\mathbf{x} - \mathbf{x}_0)$, we introduce several forms of solutions to the Stokes equation: (point force) Stokeslet, Stokeslet doublet (or called point force dipole) and potential dipole. **Stokeslet** is the singular solution to Stokes equation (2.1) with point force, which is given in the second of equation (2.18) and usually denoted by $\mathbf{u}_s(\mathbf{x}, \mathbf{x}_0)$ or $S[\mathbf{f}, \mathbf{x}_0]$ for Stokeslet located at $\mathbf{x}_0$ with constant force $\mathbf{f}$. The **Stokeslet doublet**, sometimes called **point force dipole**, is the directional derivative of a Stokeslet, i.e. $(\mathbf{b} \cdot \nabla)\mathbf{u}_s$, in the direction of a constant vector $\mathbf{b}$, always denoted by $\mathbf{u}_{sd}(\mathbf{x}, \mathbf{x}_0)$ or $SD[\mathbf{f}, \mathbf{b}, \mathbf{x}_0]$. Here $\mathbf{f}$ is the constant force, which is the same as $\mathbf{f}$ in Stokeslet. The **potential dipole** is obtained by applying the negative Laplacian to $\mathbf{u}_s$ with a

constant force $\mathbf{q}$; Also, potential dipole can be obtained from the directional derivative to a potential solution in the direction of constant vector $\mathbf{q}$. It is always denoted by $\mathbf{u}_{pd}(\mathbf{x}, \mathbf{x}_0)$ or $PD[\mathbf{q}, \mathbf{x}_0]$, where $\mathbf{q}$ is the same as the force $\mathbf{f}$ in Stokeslet. Their formulae are given as follows (see [30] and [31]):

$$\mathbf{u}_s(\mathbf{x}, \mathbf{x}_0) = S[\mathbf{f}, \mathbf{x}_0] = \frac{\mathbf{f}}{8\pi r} + \frac{(\mathbf{f} \cdot (\mathbf{x} - \mathbf{x}_0))(\mathbf{x} - \mathbf{x}_0)}{8\pi r^3}$$

$$\mathbf{u}_{pd}(\mathbf{x}, \mathbf{x}_0) = PD[\mathbf{q}, \mathbf{x}_0] = \frac{\mathbf{q}}{4\pi r} - 3\frac{(\mathbf{q} \cdot (\mathbf{x} - \mathbf{x}_0))(\mathbf{x} - \mathbf{x}_0)}{4\pi r^5}$$

$$\mathbf{u}_{sd}(\mathbf{x}, \mathbf{x}_0) = SD[\mathbf{g}, \mathbf{b}, \mathbf{x}_0] = \frac{(\mathbf{g} \cdot \mathbf{b})(\mathbf{x} - \mathbf{x}_0)}{8\pi r^3} + \frac{(\mathbf{g} \cdot (\mathbf{x} - \mathbf{x}_0))\mathbf{b}}{8\pi r^3} - \frac{(\mathbf{b} \cdot (\mathbf{x} - \mathbf{x}_0))\mathbf{g}}{8\pi r^3}$$
$$- 3\frac{(\mathbf{g} \cdot (\mathbf{x} - \mathbf{x}_0))(\mathbf{b} \cdot (\mathbf{x} - \mathbf{x}_0))(\mathbf{x} - \mathbf{x}_0)}{8\pi r^5}$$

Then the solution to this system (2.33) with point force $\mathbf{f} = (f_1, f_2, f_3)$ at point $\mathbf{x}_0$ is:

$$S[\mathbf{f}, \mathbf{x}_0] - S[\mathbf{f}, \mathbf{x}_{0,im}] - h^2 PD[\tilde{\mathbf{f}}, \mathbf{x}_{0,im}] + 2hSD[\mathbf{e}_1, \tilde{\mathbf{f}}, \mathbf{x}_{0,im}] \tag{2.34}$$

where $\mathbf{x}_{0,im} = 2w - \mathbf{x}_0, \tilde{\mathbf{f}} = (f_1, -f_2, -f_3) = 2(\mathbf{f} \cdot \mathbf{e}_1)\mathbf{e}_1 - \mathbf{f}$ and $h = x_{0,1} - w$.

The above shows the singular case when the force is a point force at $\mathbf{x}_0$ [32]. When the point force is regularized with a given blob function, i.e. $\mathbf{F} = \mathbf{f}\psi_d(\mathbf{x} - \mathbf{x}_0)$, the regularized Stokeslet, regularized potential dipole and regularized Stokeslet doublelet are expressed as

$$S_d[\mathbf{f}, \mathbf{x}_0] = \mathbf{f}H_1(r) + (\mathbf{f} \cdot (\mathbf{x} - \mathbf{x}_0))(\mathbf{x} - \mathbf{x}_0)H_2(r)$$

$$PD_d[\mathbf{q}, \mathbf{x}_0] = \mathbf{q}D_1(r) + (\mathbf{q} \cdot (\mathbf{x} - \mathbf{x}_0))(\mathbf{x} - \mathbf{x}_0)D_2(r)$$

$$SD_d[\mathbf{g}, \mathbf{b}, \mathbf{x}_0] = (\mathbf{g} \cdot \mathbf{b})(\mathbf{x} - \mathbf{x}_0)H_2(r) + (\mathbf{g} \cdot (\mathbf{x} - \mathbf{x}_0))\mathbf{b}H_2(r)$$
$$+ (\mathbf{b} \cdot (\mathbf{x} - \mathbf{x}_0))\mathbf{g}\frac{H_1'(r)}{r} + (\mathbf{g} \cdot (\mathbf{x} - \mathbf{x}_0))(\mathbf{b} \cdot (\mathbf{x} - \mathbf{x}_0))(\mathbf{x} - \mathbf{x}_0)\frac{H_2'(r)}{r}.$$

Following [31], the final solution to the Stokes equation with velocity 0 on the wall

$x = w$ is:

$$S_d[\mathbf{f}, \mathbf{x}_0] - S_d[\mathbf{f}, \mathbf{x}_{0,im}] - h^2 P D_d[\tilde{\mathbf{f}}, \mathbf{x}_{im}] + 2hSD_d[\mathbf{e}_1, \tilde{\mathbf{f}}, \mathbf{x}_{im}] + 2h \left[\frac{H_1'(r)}{r} + H_2(r) \right] (\mathbf{L} \times \mathbf{x})$$

(2.35)

where $\tilde{\mathbf{f}} = (f_1, -f_2, -f_3)$ and $\mathbf{x}_0$ is the position of a point force, and $\mathbf{x}_{0,im}$ is the symmetric point of $\mathbf{x}_0$ with respect to wall $x = w$. The last term in the above formula is also referred as a **rotlet**. In summary, the solution to the Stokes equation with M regularized point forces is represented as follows:

$$\begin{aligned}
\mathbf{U}(\mathbf{x}) = \Sigma_{k=1}^M \, & [\mathbf{f}_k H_1(|\mathbf{x}_k^*|) + (\mathbf{f}_k \cdot \mathbf{x}_k^*)\mathbf{x}_k^* H_2(|\mathbf{x}_k^*|)] - [\mathbf{f}_k H_1(|\mathbf{x}_k|) + (\mathbf{f}_k \cdot \mathbf{x}_k)\mathbf{x}_k H_2(|\mathbf{x}_k|)] \\
& - h_k^2 \left[\tilde{\mathbf{f}}_k D_1(|\mathbf{x}_k|) + (\tilde{\mathbf{f}}_k \cdot \mathbf{x}_k)\mathbf{x}_k D_2(|\mathbf{x}_k|) \right] \\
& + 2h_k \left[(\tilde{\mathbf{f}}_k \cdot \mathbf{e}_1)\mathbf{x}_k H_2(|\mathbf{x}_k|) + (\mathbf{x}_k \cdot \mathbf{e}_1)\tilde{\mathbf{f}}_k H_2(|\mathbf{x}_k|) + (\tilde{\mathbf{f}}_k \cdot \mathbf{x}_k)\mathbf{e}_1 \frac{H_1'(|\mathbf{x}_k|)}{|\mathbf{x}_k|} \right] \\
& + \left[(\mathbf{x}_k \cdot \mathbf{e}_1)(\tilde{\mathbf{f}}_k \cdot \mathbf{x}_k)\mathbf{x}_k \frac{H_2'(|\mathbf{x}_k|)}{|\mathbf{x}_k|} \right] \\
& + 2h_k \left[\frac{H_1'(|\mathbf{x}_k|)}{|\mathbf{x}_k|} + H_2(|\mathbf{x}_k|) \right] (\mathbf{L}_k \times \mathbf{x}_k)
\end{aligned}$$

where the dipole strengths are $\tilde{\mathbf{f}}_k = 2(\mathbf{f}_k \cdot \mathbf{e}_1)\mathbf{e}_1 - \mathbf{f}_k$, $\mathbf{L}_k \times \mathbf{x}_k = (f_2 y + f_3 z, -hf_2, -hf_3)'$ and $\mathbf{x}_k^* = \mathbf{x} - \mathbf{x}_k$, $\mathbf{x}_k = \mathbf{x} - \mathbf{x}_{k,im}$. Moreover,

$$H_1(r) = \frac{1}{8\pi(r^2+d^2)^{1/2}} + \frac{d^2}{8\pi(r^2+d^2)^{3/2}} \qquad H_1'(r) = -\frac{r}{8\pi(r^2+d^2)^{3/2}} - \frac{3d^2 r}{8\pi(r^2+d^2)^{5/2}}$$

$$H_2(r) = \frac{1}{8\pi(r^2+d^2)^{3/2}} \qquad\qquad\qquad H_2'(r) = -\frac{3r}{8\pi(r^2+d^2)^{5/2}}$$

$$D_1(r) = \frac{1}{4\pi(r^2+d^2)^{3/2}} - \frac{3d^2}{4\pi(r^2+d^2)^{5/2}}$$

$$D_2(r) = \frac{3}{4\pi(r^2+d^2)^{5/2}}$$

For more details of the method of regularized Stokeslets with images, see [31].

2.7   Finite vortex dipole

When talking about the method of regularized Stokeslets with images, we mentioned the "dipole" solution to the Stokes equations. We remark that the dipole is different from the "finite vortex dipole" that is the subject of this section. This finite vortex dipole is a pair of counterrotating vortices constrained to be separated by a fixed distance in 2D inviscid flow [33].

When a point vortex with strength Γ in two dimensional, incompressible, inviscid flow is located at the origin, the velocity field at $\mathbf{x} = (x, y)$ is given by

$$\mathbf{u}(\mathbf{x}) = \frac{\Gamma}{2\pi} \frac{(-y, x)}{r^2}$$

where $r = |\mathbf{x}|$. If a group of vortices are introduced to the system, the velocity field at point $\mathbf{x} = (x, y)$ will be obtained from the supersition of the velocity fields produced by each vortex:

$$\mathbf{u}(\mathbf{x}) = \sum_j \frac{\Gamma_j}{2\pi} \frac{(y_j - y, x - x_j)}{r_j^2}$$

where $r_j = |\mathbf{x} - \mathbf{x}_j|$, $\mathbf{x}_j = (x_j, y_j)$ and Γ_j are the locations of the j-th vortex and the strength of this vortex respectively [34]. Moreover, the velocity of each vortex is equal to the velocity induced by all the other vortices. Hence, the equation that dominates the motion of each vortex is

$$\frac{d\mathbf{x}_n}{dt} = \sum_{j \neq n} \frac{\Gamma_j}{2\pi} \frac{(y_j - y_n, x_n - x_j)}{r_j^2}$$

This vortex system shows that the distance between any two of vortices changes in time. As a minimal model of a self-propelled swimmer, Tchieu et. al. [33] introduced a finite vortex dipole with a constraint that the pair of counter-rotating vortices remain

a fixed distance l apart. In [33], the velocity field is expressd using complex variables. Let $\omega = u - iv$, where (u, v) is the velocity in two dimensional space,

$$\omega(z) = \sum_{j=1}^{N} \frac{\Gamma_j}{2\pi i} \left(\frac{1}{z - z_{j,l}} - \frac{1}{z - z_{j,r}} \right)$$

where Γ_j, $z_{j,l}$ and $z_{j,r}$ are the vortex strengths, the locations of the left vortex and the locations of the right vortex of the j-th finite vortex dipole respectively. Then, each vortex in the n-th finite dipole will move with the following velocities:

$$\dot{z}_{n,l} = \omega_{n,s} + \omega_{n,o}(z_{n,l}) + i\lambda_n e^{-i\alpha_n} \tag{2.36}$$

and

$$\dot{z}_{n,r} = \omega_{n,s} + \omega_{n,o}(z_{n,r}) - i\lambda_n e^{-i\alpha_n} \tag{2.37}$$

where $\omega_{n,s}$ are the self-induced velocities from the other vortex in the finite vortex dipole,

$$\omega_{n,s} = \frac{\Gamma_n e^{-i\alpha_n}}{2\pi l_n}.$$

Here l_n is the fixed distance between two vortices of the n-th finite vortex dipole and $\omega_{n,o}(z)$, the velocity induced by the other finite vortex dipoles, is given as

$$\omega_{n,o}(z) = \sum_{j \neq n}^{N} \frac{\Gamma_j}{2\pi i} \left(\frac{1}{z - z_{j,l}} - \frac{1}{z - z_{j,r}} \right).$$

The last term in equation (2.36) and in equation (2.37) comes from the constraint of fixed distance between two vortices in a finite vortex dipole, where α_n is the angle between the vector from left vortex to right vortex and the x-axis. Here λ_n is

determined by the fixed length constraint, and is given as:

$$\lambda_n = \frac{1}{2}\text{Im}[(\omega_{n,o}(z_{n,l}) - \omega_{n,o}(z_{n,r}))e^{i\alpha_n}].$$

From this constaint, the evolution of the angle α_n will be determined by

$$\dot{\alpha}_n = \frac{\text{Re}[(\omega_{n,o}(z_{n,l}) - \omega_{n,o}(z_{n,r})]}{l_n} \tag{2.38}$$

Adding equation (2.36) and (2.37), we obtain

$$\dot{\bar{z}}_n = \frac{\dot{\bar{z}}_{n,l} + \dot{\bar{z}}_{n,r}}{2} = \omega_{n,s} + \frac{\omega_{n,o}(z_{n,l}) + \omega_{n,o}(z_{n,r})}{2} \tag{2.39}$$

where z_n is the center of the finite vortex dipole. The evolution of the finite vortex dipole system will be determined by equation (2.38) and (2.39).

2.8   Transformation matrix between two vectors

In studying the rigid translation and rotation of an object, expressing the rotation about a vector is central. Assume the initial normal vector of the plane of a certain object is parallel to z-axis, i.e. $(0, 0, 1)$. After a certain rotation to the plane, its normal vector is transferred to a unit vector $\mathbf{n} = (n_1, n_2, n_3)$. This rotation is unique up to a rotation around the vector $\mathbf{n}$, however, it would not change the result for some object like torus in our case, whose shape is axisymmetric with respect to its normal. A rotation matrix that rotates the normal of an axisymmetric object from direction $(0, 0, 1)$ to unit normal $\mathbf{n} = (n_1, n_2, n_3)$ is:

$$
T = \begin{bmatrix} \dfrac{n_1 n_3}{\sqrt{n_1^2+n_2^2}} & -\dfrac{n_2}{\sqrt{n_1^2+n_2^2}} & n_1 \\[3mm] \dfrac{n_2 n_3}{\sqrt{n_1^2+n_2^2}} & \dfrac{n_1}{\sqrt{n_1^2+n_2^2}} & n_2 \\[3mm] -\sqrt{n_1^2+n_2^2} & 0 & n_3 \end{bmatrix}
$$

The advantage of treating the problem in this way is to avoid a second rotation matrix, which does not make any difference to the result because of the axisymmetry of the object. However, in general, the other rotation matrix should be included. In our case, we will use this matrix to construct a torus with normal (n_1, n_2, n_3) from a given torus with unit normal $(0,0,1)$. The normal of the torus is the vector that is perpendicular to the plane containing its circular centerline.

2.9   Movement of rigid object

In this section, we introduce another rotation matrix about a given vector, and discuss a distance-preserving numerical method. Assume that the unit vector $\mathbf{n}$ is given in the form (n_1, n_2, n_3). We are going to study the matrix describing the rotation of a given vector $\mathbf{a}$ with an angle of θ with respect to the line parallel to normal vector $\mathbf{n}$ and passing through the origin: First, if $\mathbf{a}$ is perpendicular to $\mathbf{n}$, then, the vector after rotation is given as : $\mathbf{x} = \mathbf{a}\cos\theta - \mathbf{a} \times \mathbf{n}\sin\theta$. Secondly, if they are not perpendicular, take the perpendicular part of $\mathbf{a}$ as $\mathbf{x}_1 = \mathbf{a} - (\mathbf{a} \cdot \mathbf{n})\mathbf{n}$, apply the first case to vector $\mathbf{x}_1$ and find that the vector after rotation along $\mathbf{n}$ with angle θ from $\mathbf{x}_1$ is $\mathbf{x}_2 = \mathbf{x}_1 \cos\theta - \mathbf{x}_1 \times \mathbf{n}\sin\theta$. Thus, the vector after rotation from $\mathbf{a}$ will be $\mathbf{x} = (\mathbf{a} \cdot \mathbf{n})\mathbf{n} + \mathbf{x}_2$ i.e. $\mathbf{x} = \mathbf{a}\cos\theta + (1 - \cos\theta)(\mathbf{a} \cdot \mathbf{n})\mathbf{n} - (\mathbf{a} \times \mathbf{n})\sin\theta$ after plugging the fomula of $\mathbf{x}_2$. And the matrix form of this rotation is:

$$R(\theta) = \begin{bmatrix} n_1^2 + (n_2^2 + n_3^2)\cos\theta & n_1 n_2(1 - \cos\theta) - n_3\sin\theta & n_1 n_3(1 - \cos\theta) + n_2\sin\theta \\ n_1 n_2(1 - \cos\theta) + n_3\sin\theta & n_2^2 + (n_1^2 + n_3^2)\cos\theta & n_2 n_3(1 - \cos\theta) - n_1\sin\theta \\ n_1 n_3(1 - \cos\theta) - n_2\sin\theta & n_2 n_3(1 - \cos\theta) + n_1\sin\theta & n_3^2 + (n_1^2 + n_2^2)\cos\theta \end{bmatrix}$$

$$(2.40)$$

In this thesis, we seek to calculate the trajectory of a swimming torus, given a computed translational velocity $\mathbf{U}$ and rotational velocity $\mathbf{\Omega}$ at each time step. There are two approaches to update the material points of the torus. One is to update the position of its centroid and its normal vector. The centroid and its normal vector will determine the layout of torus since the torus is axisymmetric with respect to its normal. However, this property is not generally true for non-axisymmetric objects such as the helical ring. Thus, we try to use a generalized numerical method to update the positions of a rigid body with the requirement that the distance of any two points on the surface of the rigid body remains unchanged as the time evolves. This kind of numerical method is called distance-preserving. In the study of rigid movement, if the velocity of the rigid body $\mathbf{u}$ is given as $\mathbf{U} + \mathbf{\Omega} \times \mathbf{x}$, then the positons of all points on the rigid body will satisfy

$$\mathbf{x}'(t) = \mathbf{U} + \mathbf{\Omega} \times \mathbf{x}$$

with different initial conditions. Here the right hand side of the above equation tells that the rigid body moves with **translational velocity** equal to $\mathbf{U}$, at the same time rotates with **rotational velocity** $\mathbf{\Omega}$. The solution to such system of ODEs is rewritten in the matrix form,

$$\mathbf{x}'(t) = \mathbf{U} + A\mathbf{x}(t). \tag{2.41}$$

Here A is a skew-symmetric matrix, and its relation to $\boldsymbol{\Omega}$ is

$$
A = \begin{bmatrix} 0 & -\Omega_3 & \Omega_2 \\ \Omega_3 & 0 & -\Omega_1 \\ -\Omega_2 & \Omega_1 & 0 \end{bmatrix}
$$

From the physical interpretation, we know that the solution to the system (2.41) should preserve the distance for any two points on the rigid body. And indeed this can be validated mathematically (for simplicity, let $\mathbf{U} = 0$ and assume A is independent of time t): The solution to this system is $\mathbf{x}(t) = e^{At}\mathbf{x}_0$, thus for different initial points $\mathbf{x}_1$ and $\mathbf{x}_2$, the distance after time t is

$$
\begin{aligned}
\sqrt{< (e^{At}\mathbf{x}_1 - e^{At}\mathbf{x}_2, e^{At}\mathbf{x}_1 - e^{At}\mathbf{x}_2 >} &= \sqrt{< (e^{At})^T(e^{At}\mathbf{x}_1 - e^{At}\mathbf{x}_2), \mathbf{x}_1 - \mathbf{x}_2 >} \\
&= \sqrt{< (e^{At})^T e^{At}(\mathbf{x}_1 - \mathbf{x}_2), \mathbf{x}_1 - \mathbf{x}_2 >} \\
&= \sqrt{< \mathbf{x}_1 - \mathbf{x}_2, \mathbf{x}_1 - \mathbf{x}_2 >}
\end{aligned}
$$

Here, $< \cdot, \cdot >$ is the inner product with l^2 norm and the upperscript T means transpose of the matrix. The last equality is true because A is a skew-symmetric matrix, i.e. $A = -A^T$, which implies $(e^{At})^T e^{At} = I$.

The question is whether a numerical method that updates points on the surface of a rigid body will preserve the distance. Take forward Euler method for example to solve the system (2.41). The answer is no, because this method solves the ODEs in the way: $\mathbf{x}_{n+1} = \mathbf{x}_n + A\Delta t\mathbf{x}_n + \mathbf{U}\Delta t$. Since $I + A\Delta t$ is not an orthogonal matrix, it does not preserve the distance. One also can show that many common used numerical methods, such as multi-step methods, are not distance-preserving. Notice that when

A is independent of t, the exact solution to the system of ODEs (2.41) is given by:

$$\mathbf{x}(t) = e^{At}\left(\int_0^t e^{-A\tau}\mathbf{U}d\tau + \mathbf{x}_0\right) = R(|\mathbf{\Omega}|t)\mathbf{x}_0 + e^{At}\int_0^t e^{-A\tau}\mathbf{U}(\tau)d\tau$$

or

$$\mathbf{x}(t+\Delta t) = e^{A\Delta t}\left(e^{At}\int_t^{t+\Delta t} e^{-A\tau}\mathbf{U}(\tau)d\tau + \mathbf{x}(t)\right) = R(|\mathbf{\Omega}|\Delta t)\mathbf{x}(t) + e^{A(t+\Delta t)}\int_t^{t+\Delta t} e^{-A\tau}\mathbf{U}(\tau)d\tau$$

Where R is the rotation matrix given in formula (2.40). $|\mathbf{\Omega}|\Delta t$ is the rotation angle since

$$\Delta\theta = \frac{2\pi}{T}\Delta t = \frac{2\pi}{2\pi r/|\mathbf{v}|}\Delta t = \frac{2\pi}{2\pi r/(r\cdot|\mathbf{\Omega}|)}\Delta t = |\mathbf{\Omega}|\Delta t$$

If A is not independent of t, then

$$\mathbf{x}(t+\Delta t) = e^{\int_t^{t+\Delta t} A(\xi)d\xi}\left(e^{\int_0^t A(\xi)d\xi}\int_t^{t+\Delta t} e^{-\int_0^\tau A(\xi)d\xi}\mathbf{U}(\tau)d\tau + \mathbf{x}(t)\right)$$

Approximating the integrals over $[t,\ t+\Delta t]$ by using left endpoint multiplied by Δt, we obtain the following numerical scheme

$$\mathbf{x}(t+\Delta t) = e^{A\Delta t}\left(\mathbf{x}(t) + \mathbf{U}(t)\Delta t\right) = R(|\mathbf{\Omega}|\Delta t)\left(\mathbf{x}(t) + \mathbf{U}(t)\Delta t\right) \tag{2.42}$$

which is almost the same as the scheme using forwad Euler to the differential equation (2.41) with a difference of $O(\Delta t^2)$. Thus, the accumulated error at time t is $O(\Delta t)$. Another numerical scheme is

$$\mathbf{x}(t+\Delta t) = R(|\mathbf{\Omega}|\Delta t)\mathbf{x}(t) + \mathbf{U}(t)\Delta t \tag{2.43}$$

which is also first order numerical scheme. Each way has different physical interpretation. The positions updated with formula (2.42) first translate with translational

velocity $\mathbf{U}$ and then rotate with rotational velocity $\mathbf{\Omega}$ within each time step. That updated with the other formula (2.43) is performing rotation before translation in each time step.

The above is the case when the rotational axis is passing through the origin. There are situations that the rotational axis is moving with the object. For example, in our model of torus, it translates and rotates along the line passing through its center:

$$\mathbf{x}'(t) = \mathbf{U} + A(\mathbf{x}(t) - \mathbf{x}_c(t))$$
$$\mathbf{x}'_c(t) = \mathbf{U}$$

$$(2.44)$$

with some initial conditions. Here $\mathbf{x}(t)$ is the position of the point on the surface of the torus, and $\mathbf{x}_c(t)$ is the position of the center of the torus at time t. This algorithm consists of two steps: First, every point on the rigid body translates in the way characterized by differential equation $\mathbf{x}'_c(t) = \mathbf{U}$ and then rotates in the way characterized by differential equation $(\mathbf{x}(t) - \mathbf{x}_c(t))' = A(\mathbf{x}(t) - \mathbf{x}_c(t))$. Each step is a special case of the system (2.41), and applying the former theory to each case, we will obtain the distance-preserving numerical scheme with an accumulated error $O(\Delta t)$.

In summary, we have demonstrated that a modification of the forward Euler method results in a distance-preserving method with accumulated error $O(\Delta t)$. We are still investigating distance-preserving numerical schemes that attain higher order of convergence.

Chapter 3

Tori

3.1   Introduction

In this chapter, the toroidal swimmer will be used as a simplified model of the tranverse flagellum of dinoflagellates. The interaction of dinoflagellates in Stokes flow will be studied through the study of the interaction of tori. Based on the dimensionless analyis in section 2.3, the Stokes equations are expressed in dimensionless way. Therefore, all parameters shown here are dimensionless too. The radius of the centerline $r_c = 0.5$ and the surface tangential speed $u_0 = 100$. We take the radius of tube $r_h = 0.1$. Then the rotational velocity about its centerline, which can be obtained from $\mathbf{\Omega} = \frac{\mathbf{r}_h \times \mathbf{u}_0}{r_h^2}$, has its magnitude equal $\Omega = \frac{u_0}{r_h} = 1000$. The center and the normal of the torus are assumed to be $\mathbf{x}_c = (0,\ 0,\ 0)$ and $\mathbf{n} = (0, 0, 1)$ respectively. The aspect ratio s_0 is defined as the ratio between the radius of the centerline and the radius of the tube, i.e. $s_0 = 5$ in our case. When applying the method of regularized Stokeslets, the surface of each torus will be discretized with $M = 12$ points on each cross-sectional circle and $N = \frac{r_c}{r_h} \cdot M = 60$ cross-sectional circles along the centerline. The total number of points on the surface are $N_p = MN = 720$. Then, the discretization size $\varepsilon_0 = \frac{2\pi r_h}{M} = 0.0524$ and the blob size used in regularized Stokeslets is taken as $d = \frac{\sqrt{\varepsilon_0}}{12.4372} = 0.0184$. This choice will be explained below. The table 3.1

summarizes all parameters.

r_c	0.5	r_h	0.1
u_0	100	Ω	1000
$\mathbf{x}_c$	$(0,0,0)$	$\mathbf{n}$	$(0, 0, 1)$
M	12	N	60
s_0	5	ε_0	$\frac{2\pi r_h}{M}$
d	$\frac{\sqrt{\varepsilon_0}}{12.4372}$		

Table 3.1: Default parameters for a single torus

In the following section, we validate our method by comparing the results by Leshansky et el. in [12] that used analytical methods to compute the translational velocity of a single torus in Stokes flow. We also compare our results with those in [7] that studied the motion of a waving cylindrical helical tube in a viscous fluid. We consider the toroidal glider with prescribed translational velocity, a force free toroidal swimmer and an immobile toroidal swimmer with prescribed surface tangential velocity. Lastly, in order to study the convergence of our numerical method, we examine the effects of blob size and the discretization size on the motion of a single torus as a free swimmer. In section 3.3 and section 3.4, we will show the interaction between two tori and the interaction of three tori in Stokes flow. In the last section, the interaction of two-dimensional vortex dipoles and those of two tori will be compared qualitatively to show their similarity in interaction patterns.

3.2 Validation and choice of blob size

3.2.1 Single torus

In this sub-section, we introduce a model of a toroidal swimmer. Several cases are examined using the method of regularized Stokeslets: toroidal glider, a force free swimmer and an immobile rotating torus. The last case is a combination of a toroidal glider and a force free swimmer. A torus in the toroidal glider case is pulled with force $\mathbf{F}$, then will move with a translational velocity $\mathbf{U}$. At the same time, consider its surface rotated along its centerline in the force free case to produce an opposite translational velocity $-\mathbf{U}$. Combining with these two actions will result in the torus staying in place with surface rotating. The force $\mathbf{F}$ is the force needed to fix the torus, which is confirmed in our numerical experiment.

We also examine the convergence of the numerical method. The blob size of the method of regularized Stokeslets will be chosen from the comparison between the current theory with the approximation solution in [12] and [13] in the case that the torus is treated as a free swimmer.

1. Toroidal glider

In the toroidal glider case, a rigid torus is placed in a uniform flow with translational speed U. Figure 3.1(a) shows that the computed dimensionless drag force F (scaled with $6\pi\mu r_h U$) exerted on the torus as a function of aspect ratio $s_0 = \frac{r_c}{r_h}$ is in excellent agreement with the slender body approximation in [12] and [35], where the slender body approximation is given as follows:

$$\frac{F}{6\pi\mu a U} \sim \frac{4\pi s_0}{3(\log 8s_0 - \frac{1}{2})} \tag{3.1}$$

The experiment is carried out numerically by imposing the uniform velocity $\mathbf{U}$ at every point on the toroidal surface.

2. Force free swimmer with prescribed surface tangential velocity

In the force free or propulsion velocity case, the torus is treated as a free swimmer with a prescribed surface rotational speed $\mathbf{u}_0$. The conservation of linear and angular momentum as shown in equation (2.6) is imposed. This restriction results in the rigid motions of the torus with translational speed U and rotational speed Ω. From the axisymmetry of the shape of the torus, the torus will translate but not rotate, i.e. $\Omega = 0$. The dimensionless propulsion velocity $\frac{U}{u_0}$ is plotted as a function of aspect ratio $s_0 = \frac{r_c}{r_h}$ in figure 3.1(b). It shows that our results and the asymptotic solution ([12] and [13])

$$U \sim \frac{u_0}{2s_0}(\log(8s_0) - \frac{1}{2}) \tag{3.2}$$

are in excellent agreement when taking the same discretization size and blob size as in the toroidal glider case. The number 12.4372 is chosen intentionally to minimize the difference between current theory with the method of regularized Stokeslets and asymptotic result in [13] when the aspect ratio is equal to 20. Based on those parameters, when the aspect ratio is greater than 10, the relative error is less than .4% in both cases. The overall relative error is less than 3.5% when smaller aspect ratios (up to $s_0 \geq 2$) are taken into consideration.

A specific example of a free swimming torus with parameters in Table 3.1 is studied here too. We find that the torus moves upwards with the translational velocity (2.2149e-15, -8.0597e-15, 3.1338e+01), but no rotation at all. Figure 3.2(a) shows the velocity field and the streamlines of the flow generated by a single force-free
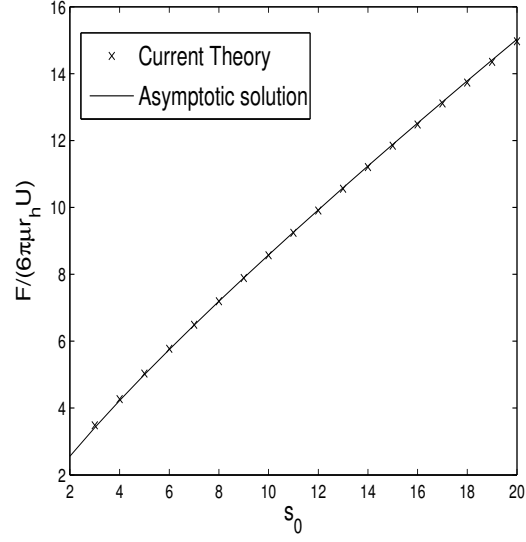
(a) Toroidal glider
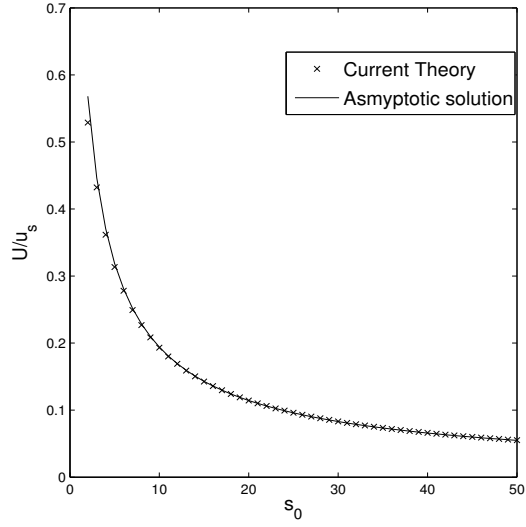
(b) Force free

Figure 3.1: (a) Toroidal glider case shows the dimensionless force $\frac{F}{6\pi\mu r_h U}$ exerted on the torus with respect to aspect ratio $s_0 = \frac{r_c}{r_h}$. Note that the current theory (star) is in excellent agreement with the asymptotic solution (solid line) given in formula (3.1). (b) Propulsion velocity case shows the dimensionless propulsion velocity $\frac{U}{u_s}$ with respect to aspect ratio $s_0 = \frac{r_c}{r_h}$. Again note that the current theory (star) and the asymptotic solution (solid line) given in formula (3.2) are in excellent agreement.

torus. A single torus with a prescribed surface tangential velocity will move in the certain direction that we define to be the normal vector of the torus.

3. Immobile torus with prescribed surface tangential velocities

The model introduced here is an immobile torus with a surface rotating speed $u_0 = 100$. As mentioned before, this model is a combination of a toroidal glider and a force free swimmer in a certain way, which is confirmed numerically: The torus with default parameters is treated here. On the one hand, we apply the surface tangential velocity to compute the transaltional velocity $\mathbf{U}$ in the force free case. Then we impose the translational velocity $-\mathbf{U}$ in toroidal glider case, and compute the surface forces $\mathbf{F}_1$. On the other hand, we compute the surface forces $\mathbf{F}_2$ similar to the glider case by assigning the velocity to be the surface tangential velocity at each discretization point on the surface of the torus. The results show that $\mathbf{F}_1 = \mathbf{F}_2$ at each point. Moreover, we find that the total drag force is (-4.4853e-14, -2.5258e-14, -2.9714e+02). This means that the necessary drag force is pointing downward, which in turn implies the torus has a tendency to move upward. The velocity field and the streamlines of the flow of the fluid on the cross-sectional plane $y = 0$ are shown in Figure 3.2(b).

4. Study of the convergence of the numerical method

In order to study the convergence of the numerical method, we ran several experiments of the force free torus by varying the discretization size or the blob size or both. The method of regularized Stokeslets involves two types of errors: the discretization error coming from the approximation of the surface integral and the regularization error coming from the replacement of the delta function by a certain blob function. Thus, to study the convergence of the method of regularized Stokeslets we need to
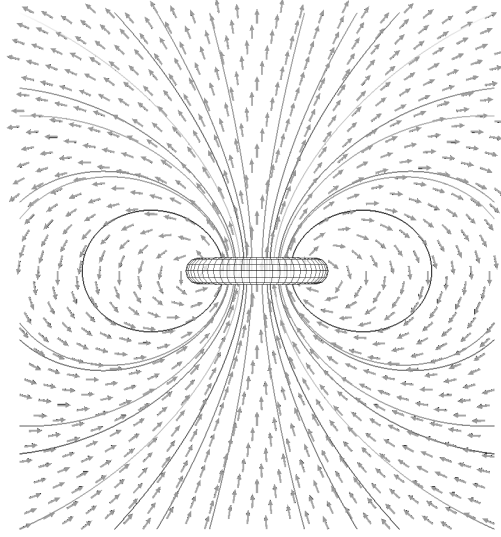
(a) Force free torus
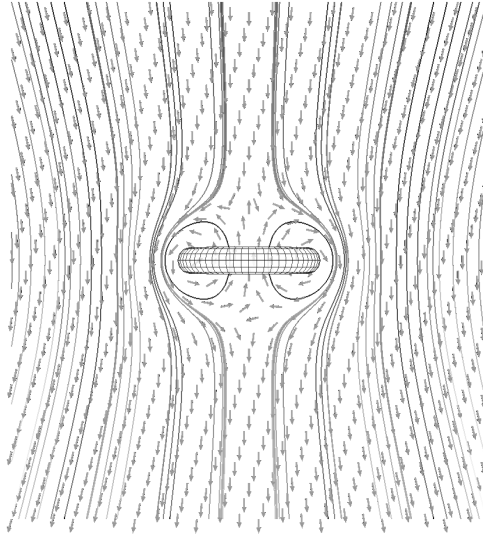
(b) Torus with fixed center

Figure 3.2: Streamlines and velocity field in the plane $y = 0$ around a force-free torus (figure 3.2(a)) and a torus with fixed center (figure 3.2(b)) are shown with aspect ratio $s_0 = 5$. The solid lines are the streamlines of the flow around the toroidal swimmer. The vectors indicate the direction of the flow at that point. Note that the length of the vectors are set to be uniformly equal regardless of the different magnitudes of the velocity at different points.

analyze the effect of each error.

Figure 3.3 shows the relative error of the speed, which is defined as $|\frac{u-u_a}{u_a}|$, is decreasing and then increasing when the blob size d decreasing. Since the error of the numerical method is $O(\frac{\varepsilon_0^2}{d^3}) + O(d^2)$, the error will be dominated by $O(d^2)$ when the blob size is large. The error will be dominated by $O(\frac{\varepsilon_0^2}{d^3})$ if the blob size is small. This figure also shows that the relative error of the speed goes toward 1 with decreasing blob size. Here, u is the computed translational speed with the method of regularized Stokeslet and u_a is the asymptotic speed given in formula (3.2) for four different aspect ratios. This phenomenon can be explained in this way: When the blob size approaches zero, the diagnoal elements of Stokeslet matrix $\frac{2}{d}$ is so large with small blob size d that the matrix A in equation (2.7) would approximately turn into

$$
A = \frac{2}{d}
\begin{bmatrix}
 & & & 0 & 0 & 0 & 0 & 0 & 0 \\
 & I_{3N\times 3N} & & \vdots & \vdots & \vdots & \vdots & \vdots & \vdots \\
 & & & 0 & 0 & 0 & 0 & 0 & 0 \\
0 & \cdots & 0 & 0 & 0 & 0 & 0 & 0 & 0 \\
0 & \cdots & 0 & 0 & 0 & 0 & 0 & 0 & 0 \\
0 & \cdots & 0 & 0 & 0 & 0 & 0 & 0 & 0 \\
0 & \cdots & 0 & 0 & 0 & 0 & 0 & 0 & 0 \\
0 & \cdots & 0 & 0 & 0 & 0 & 0 & 0 & 0 \\
0 & \cdots & 0 & 0 & 0 & 0 & 0 & 0 & 0 \\
\end{bmatrix}
\tag{3.3}
$$

where $I_{3N\times 3N}$ is a 3N by 3N identity matrix. An iterative method, such as conjugate gradient, to equation (2.7) with matrix (3.3) would result in the solution $\tilde{\mathbf{f}} = \frac{d}{2}\tilde{\mathbf{u}}$, which means that the translational velocity will be zero (see the structure of $\tilde{\mathbf{u}}$ in equation (2.7) for reason). However, the actual translational velocity is not zero if

the torus is prescribed with a non-zero surface tangential velocity. From this point of view, the blob size can not be taken too small relative to the discretization size. In fact, the blob size is usually chosen linearly or quadratically proportional to the square root of the discretizaion size.
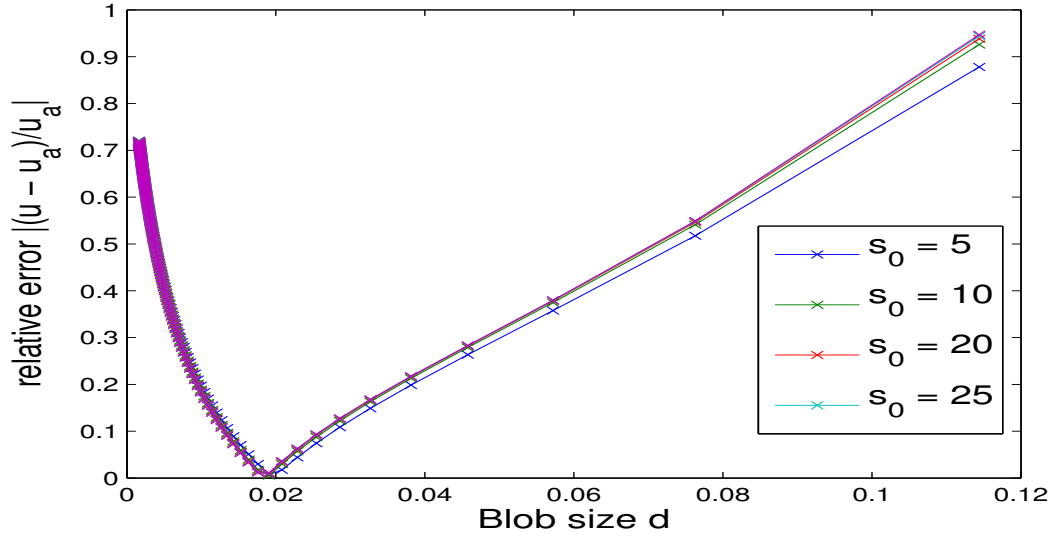

Figure 3.3: With different aspect ratios, $s_0 = 5, 10, 15, 20$ and 25, but fixed discretization size $\varepsilon_0 = 2\pi \cdot 0.1/12 = 5.2360e - 02$, the relative error of the translational velocity (given in absolute value) is shown with respect to varying blob sizes d. The error is given as $O(\frac{\varepsilon_0^2}{d^3}) + O(d^2)$. The relative error in the right branch, when the blob size is large, is dominated by $O(d^2)$. The relative error in the left branch, when the blob size is relative small, is dominated by $O(\frac{\varepsilon_0^2}{d^3})$. When the blob size d goes to 0, the relative error has a tendency to 1. Here, u and u_a are the computed translational velocity and the asymptotic translational velocity given in formula (3.2) respectively.

Next, for six different aspect ratio s_0, we fix the blob size $d = 1.8398e - 02$, but decrease the discretization size (i.e. increase the number of points, M, on each cross-sectional circle and the number of points, N, on the transverse section). Figure 3.4 shows the trend of the convergence of the relative error.
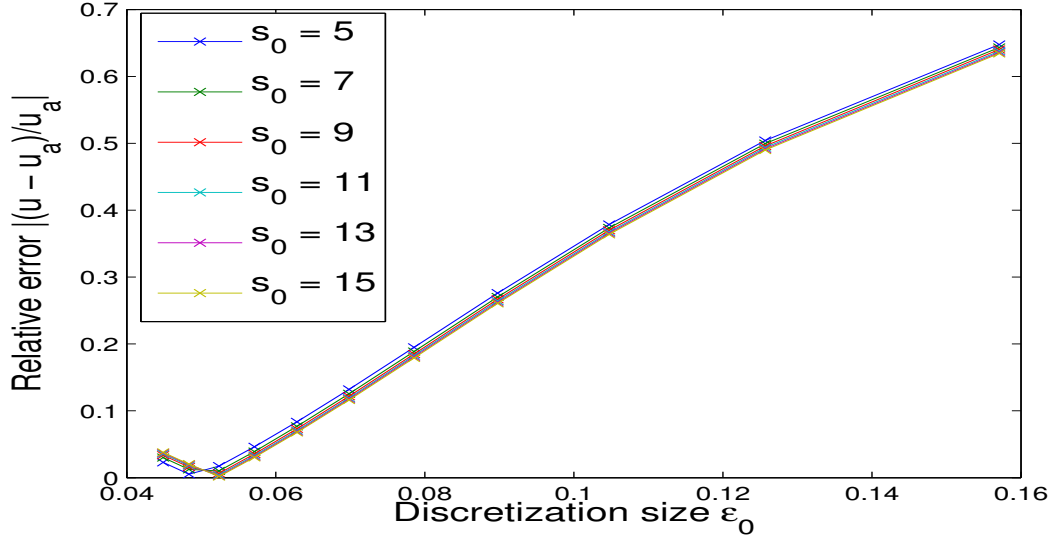
Figure 3.4: With different aspect ratio, $s_0 = 5, 7, 9, 11, 13$ and 15, but unchanged blob size $d = 1.8398e{-}02$, the relative error of the translational velocity (given in absolute value) is plotted against the discretization size ε_0. With the decreasing in discretization size, the relative error shows a tendency of convergence if a finer discretization size is implemented. Here, u and u_a are the computed translational velocity and the asymptotic translational velocity given in formula (3.2) respectively.

Lastly, we consider the torus with varying blob size d and varying discretization size ε_0 when aspect ratio $s_0 = 4$ with a relation:

$$d = \frac{\sqrt{\varepsilon_0}}{12.4372}.$$

Figure 3.5 shows that the relative error given in absolute value $\left|\frac{u - u_a}{u_a}\right|$ is decreasing when the discretization is small enough. This shows that $d \approx C\sqrt{\varepsilon_0}$ would be an appropriate choice of the blob size when applying method of regularized Stokeslets.

Above all, the blob size can not be taken arbitrary, but should be linearly or quadratically proportional to the square root of the discretization size. However, the
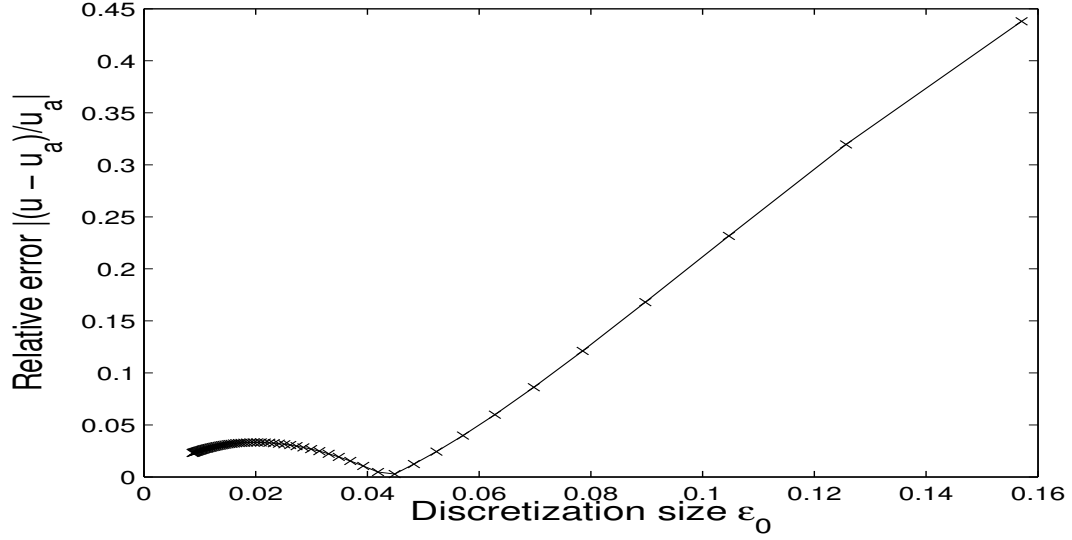
Figure 3.5: When aspect ratio $s_0 = 4$, fix blob size $\delta = \sqrt{\varepsilon_0}/12.4372$. The relative error between translational velocity u from current theory and that u_a from the asymptotic solution given in formula (3.2) is plotted with respect to the discretization size ε_0. From the tail close to the origin, the relative error shows a decreasing tendency.

regularization error could be observed as the discretization size goes to zero.

3.2.2 Waving helical tube

In this section, we reproduce the results in [7] to validate our code of method of regularized Stokeslets. The free swimmer studied here is the helical tube with centerline Γ, which is a closed circular helix described by

$$
\begin{cases}
x(s,t) & = \left[r - R\sin\left(\frac{2\pi s}{\lambda} - \omega t\right)\right]\cos\left(\frac{s}{r}\right) \\
y(s,t) & = \left[r - R\sin\left(\frac{2\pi s}{\lambda} - \omega t\right)\right]\sin\left(\frac{s}{r}\right) \\
z(s,t) & = R\cos\left(\frac{2\pi s}{\lambda} - \omega t\right).
\end{cases}
\tag{3.4}
$$

where $0 \leq s \leq 2\pi r = L$, and r is the radius of the baseline circle, which is on the plane that $z(s,t) = 0$. R and λ represent the helical amplitude and the wave length

respectively. The angular speed is denoted by ω. The number of pitches n_p is defined as $\frac{L}{\lambda} = \frac{2\pi r}{\lambda}$. Then, the wave speed denoted by ω_s is $\frac{\omega\lambda}{2\pi}$ as time progresses. The radius of the tube, which is the distance between the surface of the tube to the centerline, is denoted by r_h. A figure of helical ring with illustration of parameters is shown in Figure 3.6.
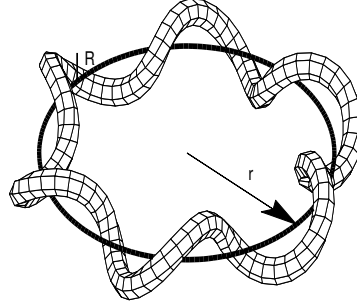

Figure 3.6: An illustration of the helical tube. The black circle is the baseline circle with radius r. The amplitude is R and the number of pitches is equal to 6.

Using the same parameters of the helical tube as in [7] by choosing the number of pitches $n_p = 3$, amplitude $R = 0.09$, radius of centerline $r = 0.5$, angular speed $\omega = 0.1$ and radius of tube $r_h = 0.035$, we also study the effect of wave amplitude on velocities, the effect of number of pitches on velocities, the effect of simultaneous change of slenderness and amplitude on velocities. The translational velocity and the rotational velocity are computed by applying the method of regularized Stokeslets. The helical tube is discretized using $M = 6$ points on each cross-sectional circle and $N = 110$ cross-sectional circles along the centerline. The blob size d for the method

of regularized Stokeslets is taken as $\frac{7}{12}\varepsilon_0$, where ε_0 is the average distance between linked points on the discretized surface. Since the helical ring here is treated as a free swimmer, the rigid motion with translational and rotational velocity will be calculated by equation (2.7).

1. Effect of wave amplitude on velocities

In [7], the effect of wave amplitude on velocities was studied under the comparison of several numerical methods. Here, we are going to reproduce the result by using the method of regularized Stokeslets. The rotational velocity is defined as the velocity tangential to the circular axis of the ring's centerline, and is denoted by VT. The translational velocity is the velocity in the z-direction, and is denoted by VB. The resulting VT and VB computed, normalized by the wave speed ω_s as a function of the amplitude normalized by the wave length λ, are shown in Figure 3.7, which correponds to the figure 6 in [7].

2. Effect of number of pitches around ring on velocities

The effect of number of pitches on the velocities of the waving helical tube is studied here. The number of the pitches is limited as the helical tube has finite thickness. The result is shown in figure 3.8 with the translational velocity and rotational velocity normalized by the wave speed ω_s with respect to the number of pitches n_p, which ranges from 2 to 8. This figure corresponds to the figure 8 in [7]. They show great agreement with each other.

3. Effect of simultaneous change of slenderness and amplitude on velocities

The effect of slenderness and amplitude of the the waving helical tube to the translational and rotational velocities is studied here. Non-dimensional helix amplitude
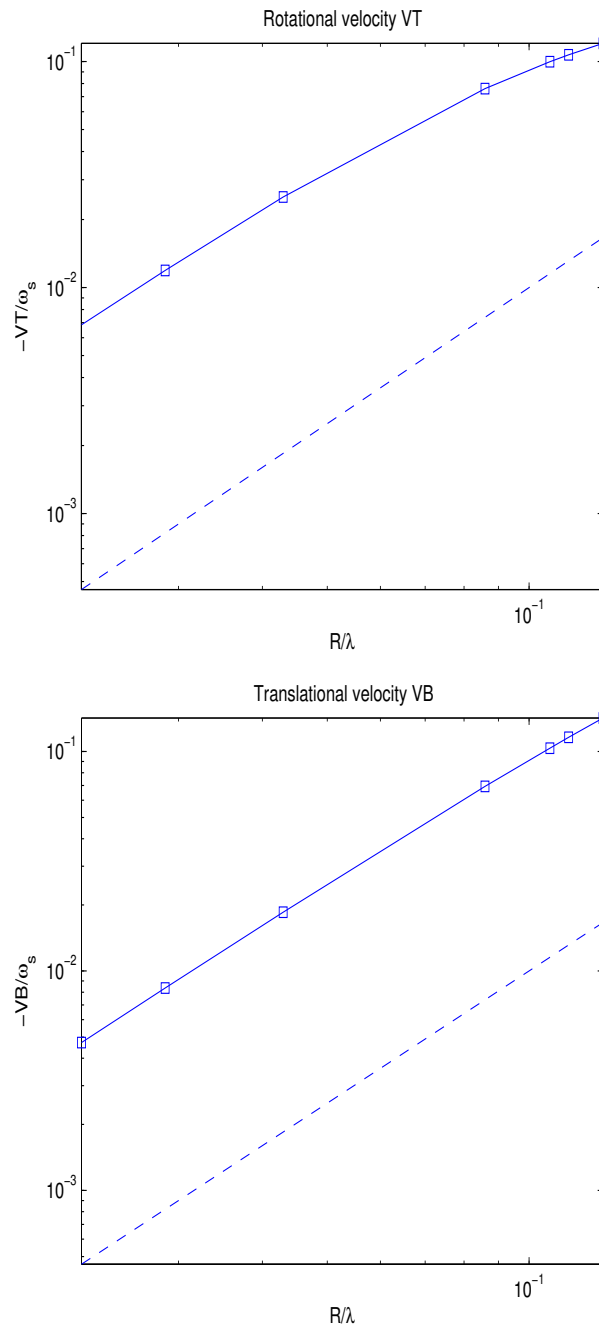
Figure 3.7: Log-log plot of (upper) normalized rotational velocity with respect to R/λ and (lower) normalized transaltional velocity with respect to R/λ. The dash line is $y = (R/\lambda)^2$ plotted for reference.
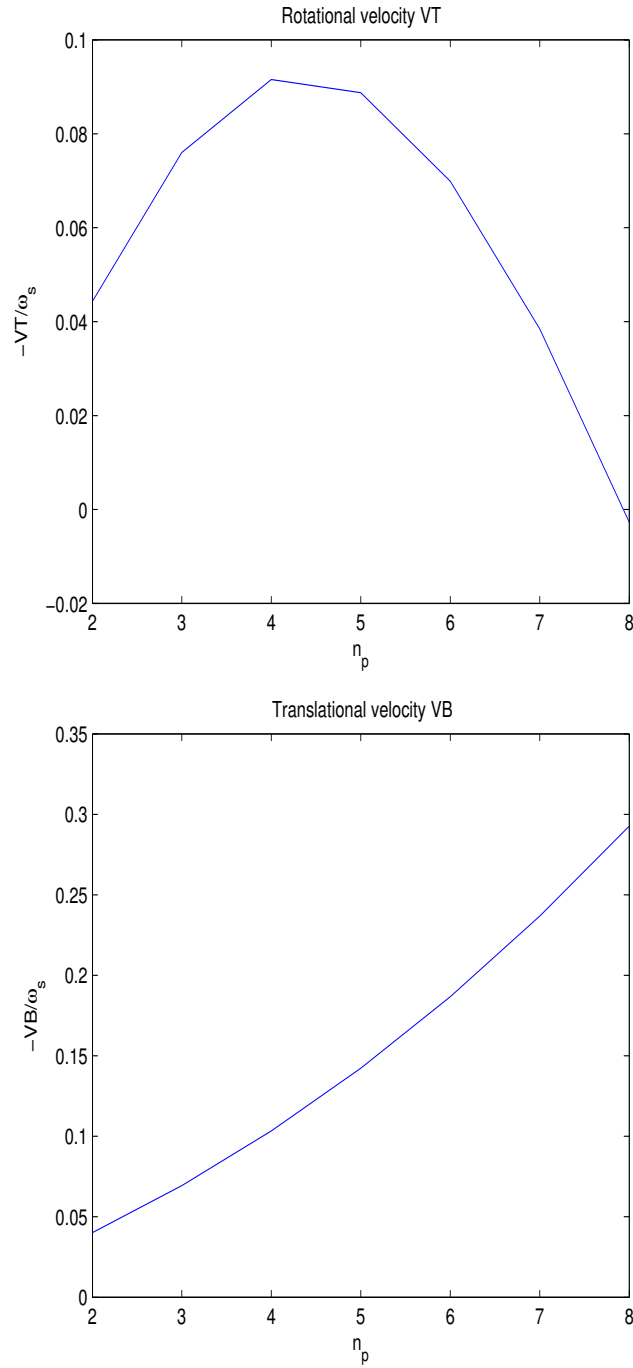
Figure 3.8: (upper) Normalized rotational velocity $-VT/\omega_s$ is plotted against the number of pitches n_p and (lower) normalized translational velocity VB/ω_s against n_p.

$R_\beta = \hat{R}/\beta$ and non-dimensional tube radius $r_\beta = \frac{\hat{r}}{\beta}$ are chosen with $\hat{R} = 0.09$ and $\hat{r} = 0.035$. The setup is equivalent to keeping the tube radius and helix amplitude fixed, but varing the radius of the baseline circle. Figure 3.9 shows the transaltional velocity and rotational velocity normalized by the wave speed ω_s with respect to β, which takes values $\frac{1}{3}, \frac{1}{2}, 1$ and $\frac{5}{4}$, the figure corresponding to the figure 10 in [7].

Above all, all results compared with those in [7] are in good agreement. The validation of the code for the method of regularized Stokeslets is evident. However, to use the method of regularized Stokeslets, the choice of the blob size d is essential and varied for different problems. Based on our experience, the blob size is chosen to be linearly or quadratically proportional to the square root of the discretization size with a constant less than 1.

3.3   Interaction of two tori

In this section, the interaction of two toroidal free-swimmers will be studied numerically. The parameters are taken as default values in the introduction of this chapter. Several initial arrangements of the two tori, including two tori in tandem or abreast, will be studied. Aside from the axisymmetric arrangement of tori, other configurations, such as staggered tori without alignment will be considered too. Here, "alignment" means that the line connecting the two centers of the tori is parallel to the normal of each torus.

3.3.1   Two tori placed in tandem

We consider two tori placed in tandem that are either co- or counter-rotating. For counter-rotating tori, there are two situations. One is two normals pointing towards each other, called 'face-to-face' in our context. The other one is two normals
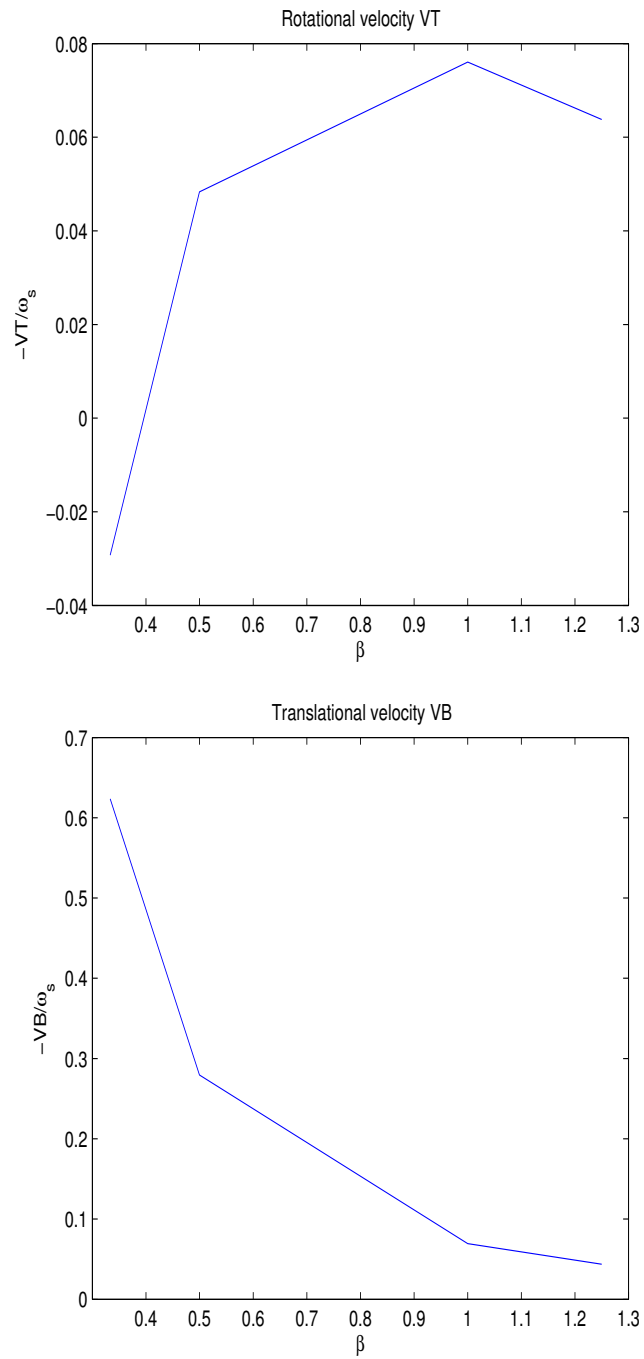
Figure 3.9: (upper) Normalized rotational velocity $-VT/\omega_s$ and (lower) normalized translational velocity are plotted against β.

pointing away from each other, which is called 'back-to-back' in our context. It is important to notice that face-to-face and back-to-back are actually the same moving mechanism but with time reversed. In the face-to-face case, two tori are moving toward each other (see Figure 3.10) with decreasing translational velocity(see Figure 3.12(a)). No rigid rotation is observed. In the back-to-back case, two tori are moving away from each other (see Figure 3.11) with increasing translational velocity (see Figure 3.12(a)). Rigid rotation is not observed. When moving away far enough from each other, they almost attain the maximum translational velocity, which is equal to the translational velocity of a single torus. This means that two tori are inhibiting each other when rotating in opposite direction.

When the surfaces of the two tori are moving in the same direction (co-rotating tori, but let's call it 'face-to-back'.), they both are moving with the same velocity, which is a little larger than that of a single torus in force free case. Their distance keeps the same as they moves (see figure 3.13). However, different distances result in different translational velocity, and the closer they are, the larger translational speed they attain (see figure 3.12(b)). Thus, when two tori move with the same direction, they will boost the movement of each other.

In the far field case, the translational velocity[1] of the tori is given [27],

$$U = \frac{u_o}{2s_0}\left(\log 8s_0 - \frac{1}{2}\right) \pm \frac{\pi u_o}{s_0}\left(\frac{11 + 2\tilde{d}^2}{2(4 + \tilde{d}^2)^{5/2}}\right) \tag{3.5}$$

for co- and counter-rotating tori respectively. Here, s_0 is the aspect ratio, $\tilde{d}$ is the normalized distance between the centers of two tori by the radius of centerline r_c and

---

[1]The formula (31) for the translational velocity in [27] is given with ε^2, where $\varepsilon = \frac{1}{s_0}$, outside each parenthesis, however, comparing with formula (12) in [12], this term should be ε.

(a) t = 0.00000

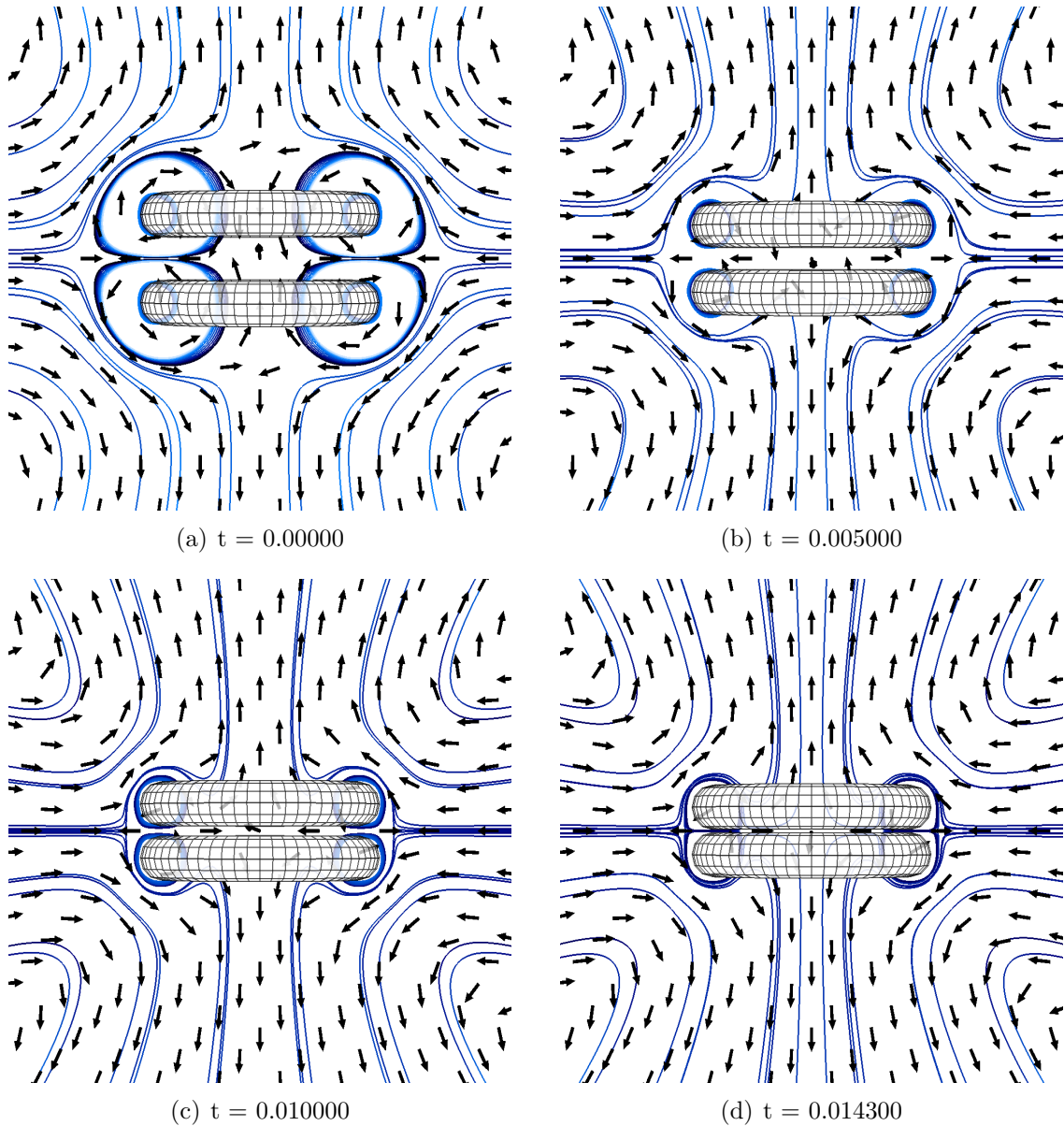(b) t = 0.005000

(c) t = 0.010000

(d) t = 0.014300

Figure 3.10: Two tori are placed face to face. They are approaching each other without rigid rotation. The closer they are, the smaller translational velocity they attain (see figure 3.12(a)). The arrows, which are set with equal length, only imply the direction of the fluid at each point. The streamlines are shown as solid lines.
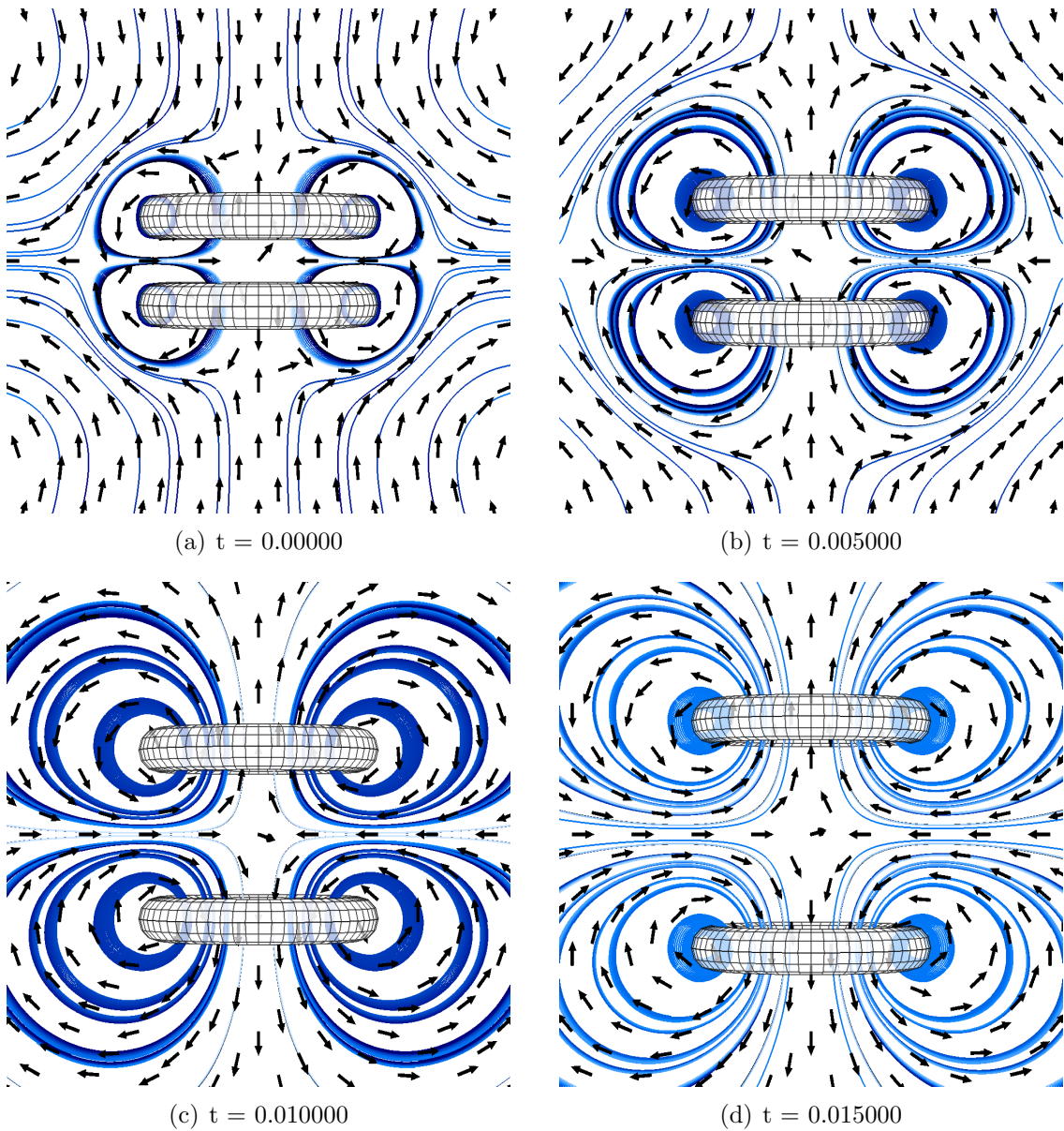
(a) t = 0.00000

(b) t = 0.005000

(c) t = 0.010000

(d) t = 0.015000

Figure 3.11: Two tori are placed back to back. They are moving away from each other without any rotation, and the further they are, the larger translational velocity they attain (see figure 3.12(a)). The arrows imply the direction of the fluid at that point, and not the magnitude of the velocity. The streamlines are shown as solid lines.
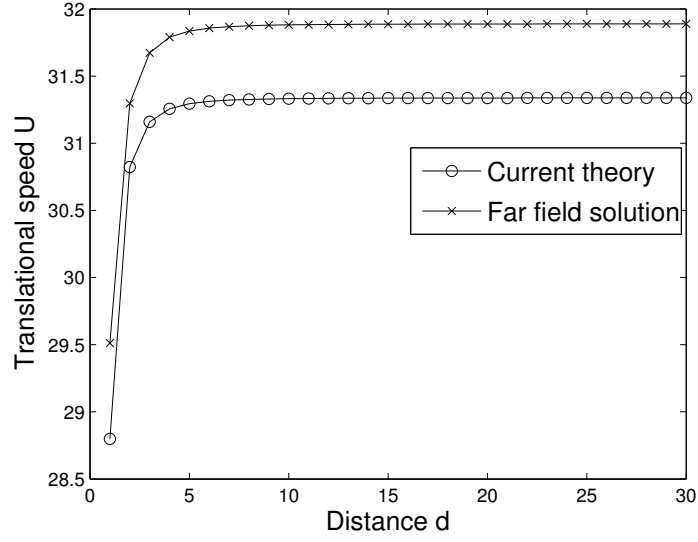
(a) Counter-rotating tori. The translational velocity increases as the distance increases, and no rotation has been observed. Both theory show the same tendency when the distance is increasing.
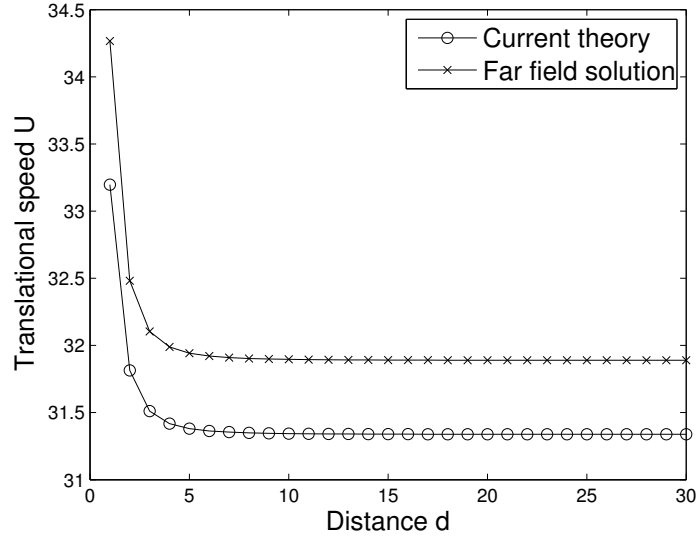
(b) Co-rotating tori. The translational velocity decreases as the distance increases, and no rotation velocity has been observed too. Both theory show the same tendency when the distance is increasing.

Figure 3.12: Two tori in tandem and moving with opposite direction (figure 3.12(a)) or same direction(figure 3.12(b)). The current theory we use is the method of regurlarized Stokeslets. The far field solution is given in formula (3.5) for two co- or counter-rotating tori in the far field limit. Although, both figures show the gap between the current theory and the far field solution, the relative errors in both cases are less than 2%.

(a) t = 0.00000

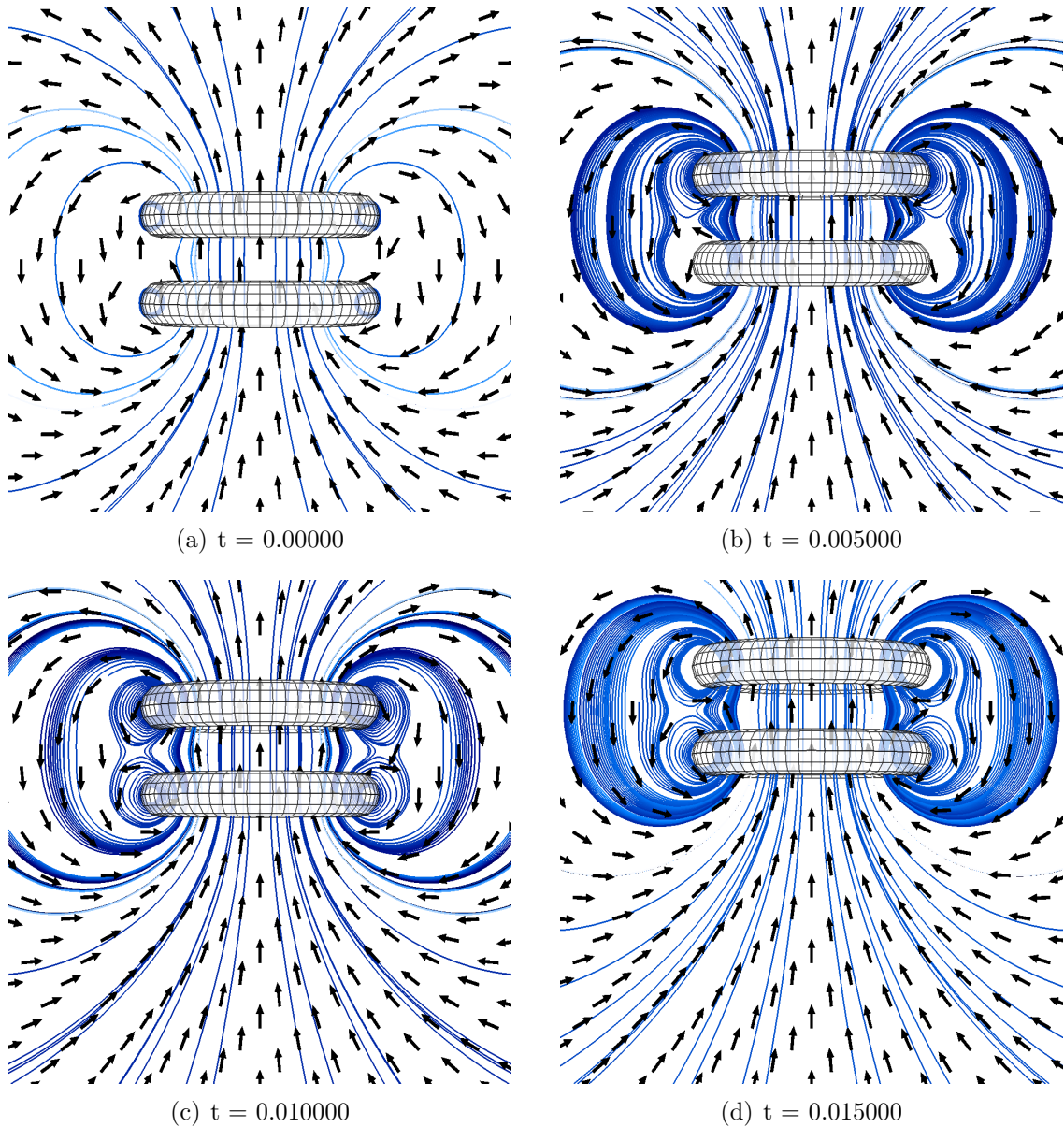(b) t = 0.005000

(c) t = 0.010000

(d) t = 0.015000

Figure 3.13: Two tori are placed face to back. They move in the same direction and at the same speed, but with no rotation. The distance between the two tori is the same all the time. However, the magnitude of translational velocity is larger than that of a single torus in the free force case (see 3.12(b)). The arrow implies the direction of the fluid at that location and the length does not mean the magnitude of the velocity. The streamlines are shown as solid lines. The visual differences are due to the plotting method used. Theoretically the streamlines and vector fields are the same at each time.

u_0 is the surface rotational speed. A comparison between this approximation theory with current theory is shown in figure 3.12(a) and 3.12(b). The distance in graph is the distance between two tori. In our case, $\tilde{d} = \frac{d+0.2}{0.5}$. The same tendency is observed in both figures. Although the gap between current theory and the far field solution is observed in both figures, the relative error in both co- and counter-rotating cases are less 2%.

Furthermore, we also find that the translational velocities of two tori in tandem obey a bilinear relationship with their surface tangential velocities, i.e.

$$U_1 = a(d)\Omega_1 + b(d)\Omega_2 \qquad U_2 = c(d)\Omega_1 + e(d)\Omega_2$$

where $a(d)$, $b(d)$, $c(d)$ and $e(d)$ are functions of the distance d between two tori. Ω_1 and Ω_2 are the surface rotational speeds of two tori respectively. After switching the rotational velocities of two tori, their velocities swap. This fact implies that $a(d) = e(d)$ and $b(d) = c(d)$. So, the formula for translational velocities are

$$U_1 = a(d)\Omega_1 + b(d)\Omega_2 \qquad U_2 = b(d)\Omega_1 + a(d)\Omega_2$$

Moreover, $a(d)\Omega_1$ is increasing to U_0 and $b(d)$ is decreasing to 0 as $d \to +\infty$, where U_0 is the translational velocity of a single torus with surface rotational speed Ω_1. These relations have been validated in our experiments.

3.3.2   Two tori without alignment

In the axisymmetric case of tori placed in tandem, the line connecting the centers of the tori is co-linear with the normal vector of each torus. We now consider perturbations of this axi-symmetric case in which we restrict the initial placement

such that the normal vectors of each tori are parallel. We can assume that the plane spanned by the line connecting the torus centers and the parallel normal directions is the plane y=0. The advantage of this assumption is that both tori will yield zero translational velocity in y-direction and rotate only about the y-axis. All figures with tori shown below are observed from the negative y axis, which is pointing out of the page, and the x-axis and the z-axis are pointing to the right and upward respectively.

Before showing the numerical results, a way of predicting the evolution of each torus in two-tori interaction is presented. The induced velocity for one is determined by its position in the flow fields caused by the other one. However, the induced rotational velocity comes from the relative positions, which directly affects the force distributions from the other one. For perturbations to the counter-rotating tori (Figure 3.14(a) and 3.14(b)), the other-induced velocities of the tori will be opposite to each other since both of them move upstream but the stream directions are opposite. Together with opposite self-induced velocity in the direction of the normal vector, this fact implies that two translational velocities will be opposite. However, since the relative positions of one tori to the other one are the same, the uneven force distributions causing the rotation will be the same, which means they will rotate in the same direction. The same reason can be applied to the perturbation to the co-rotating tori (Figure 3.14(c)). With the same self-induced translational velocity and same other-induced translational velocity but opposite relative positions, the two tori will translate with the same translational velocity but rotate in opposite directions. These symmetry arguments will be validated with the following numerical results.

Let's go back to the discussion of the numerical results. First, a small perturbation to the face-to-face case (Figure 3.15) will cause the pair move close to each
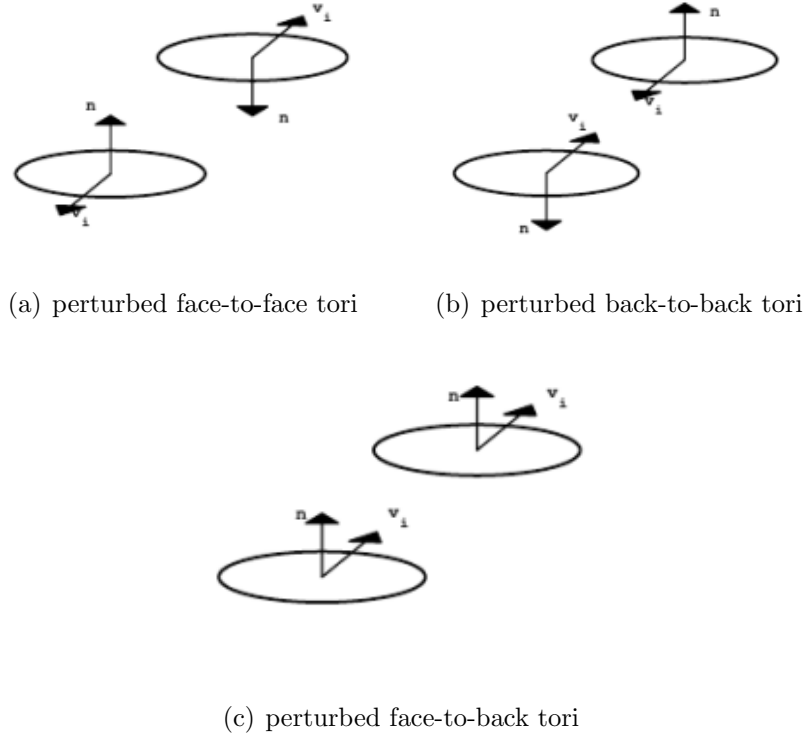
(a) perturbed face-to-face tori   (b) perturbed back-to-back tori

(c) perturbed face-to-back tori

Figure 3.14: Illustration of perturbation to the three axisymmetric cases: face-to-face, back-to-back and face-to-back. The normal direction, n, is the direction of the self-induced translational velocity, and v_1 denote the induced velocity from the other torus.

other and to rotate clockwise from the view of negative y axis. The closer they are, the smaller translational velocity is. However, the rotational velocity is increasing as the distance gets closer (see figure 3.19(a)). Figure 3.18(a) shows the distance between the normals of two tori with respect to time decreases even though the translational velocity components in the direction perpendicular to normal direction and y-axis (let it called **perpendicular direction**) are pointing away from each other. A tendency of alignment is observed in this case.

Secondly, we consider a small perturbation to the back-to-back case (Figure 3.16). Two tori move away from each other in the normal direction and also move away from in the perpendicular direction (Figure 3.18(b)). Moreover, the pair rotates

counterclockwise at the same time with the same magnitudes.

Next, we consider a small perturbation to the face-to-back case. Here the pair does not rotate in unison, but rotate in opposite direction (Figure 3.17). The top one rotates clockwise and the bottom one rotates counterclockwise. Figure 3.17 shows the case that two tori rotate in opposite way all the time. The lower one is rotating faster than the top one that its right end goes into the hole of the top one (see figure (d), which is shown in figure 3.22(a) from other angle of view). Collision might occur when two tori are too close.

Furthermore, we plane two tori abreast on the plane $z = 0$ with both going upward at the intial time $t = 0$ (see figure 3.20). At this time, from the symmetry of their positions, they will move with the same translational velocities. As for rotation, for the right torus, since its leftmost end is pushed down more than its rightmost end, it will rotate counterclockwise. The same analysis can be applied to the left torus, and it will rotate clockwise. Thus, the relative positions of these two tori decides that they will rotate in opposite direction. As time progesses, since preserving its symmetry with respect to the y-z plane, these two tori will move with the same speed but in a symmetric direction with respect to the plane $x = 0$ and rotate in opposite way. The combination of transaltion and rotation to each torus results that these two tori will moving toward each other almost like folding wings of a butterfly with two wings approaching each other in x-direction (see figure 3.19(b)).

Lastly, one interesting perturbation to the face-to-back case is placing the center of one of the torus at $(-0.8, 0, -0.1)$ and that of the other at $(0.8, 0, 0.1)$. The initial velocities of both tori are upward, but the rotational velocity of the lower one is
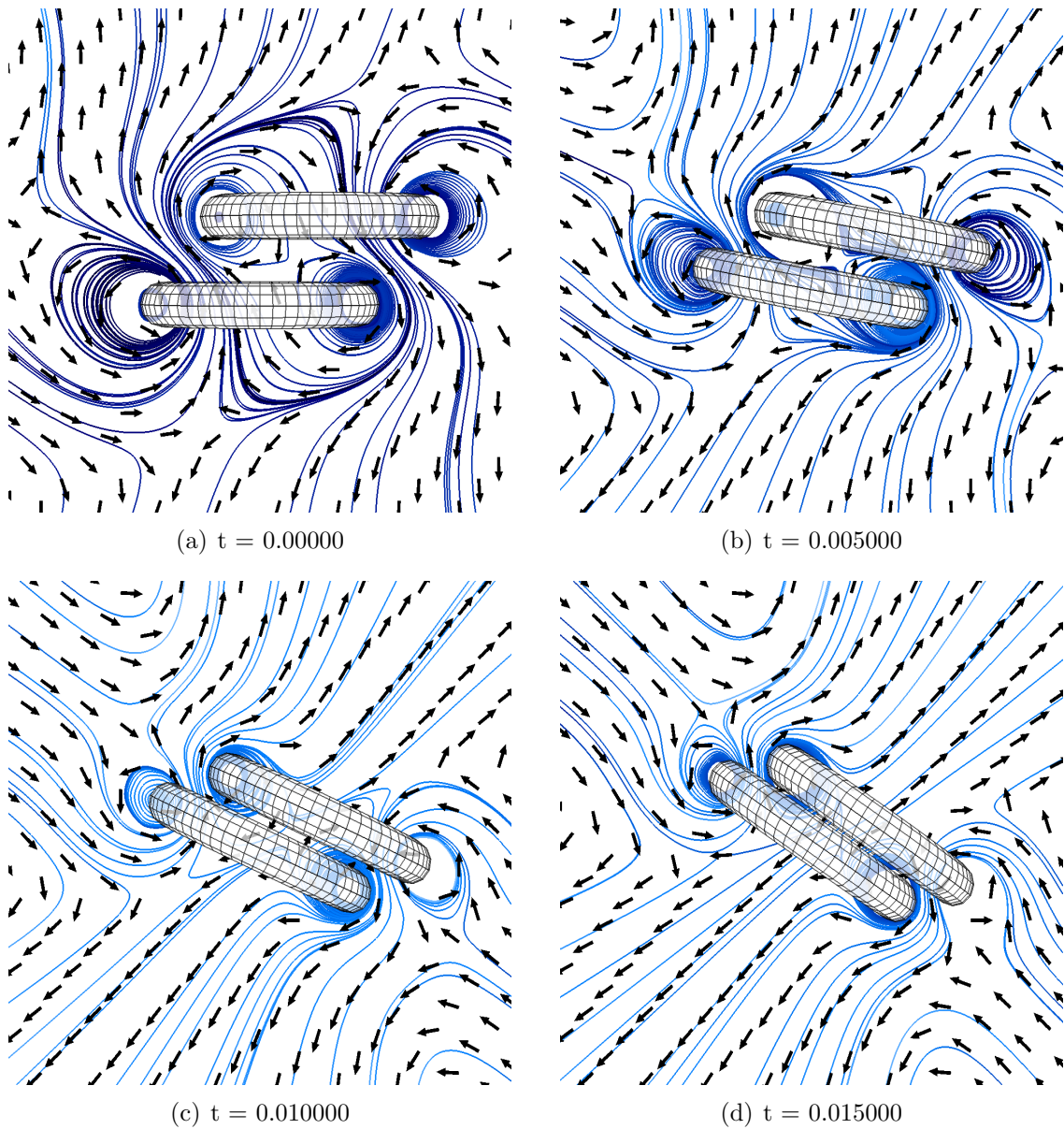
(a) t = 0.00000

(b) t = 0.005000

(c) t = 0.010000

(d) t = 0.015000

Figure 3.15: Two tori are placed face to face with a perturbation to the right in the x direction. They move toward each other with same translational velocity and same rotational velocity(clockwise). They also show a tendency to align themselves (see figure 3.18(a)). The arrows imply the direction of the fluid at each point, and not the magnitude of the velocity. The streamlines are showed as solid lines.
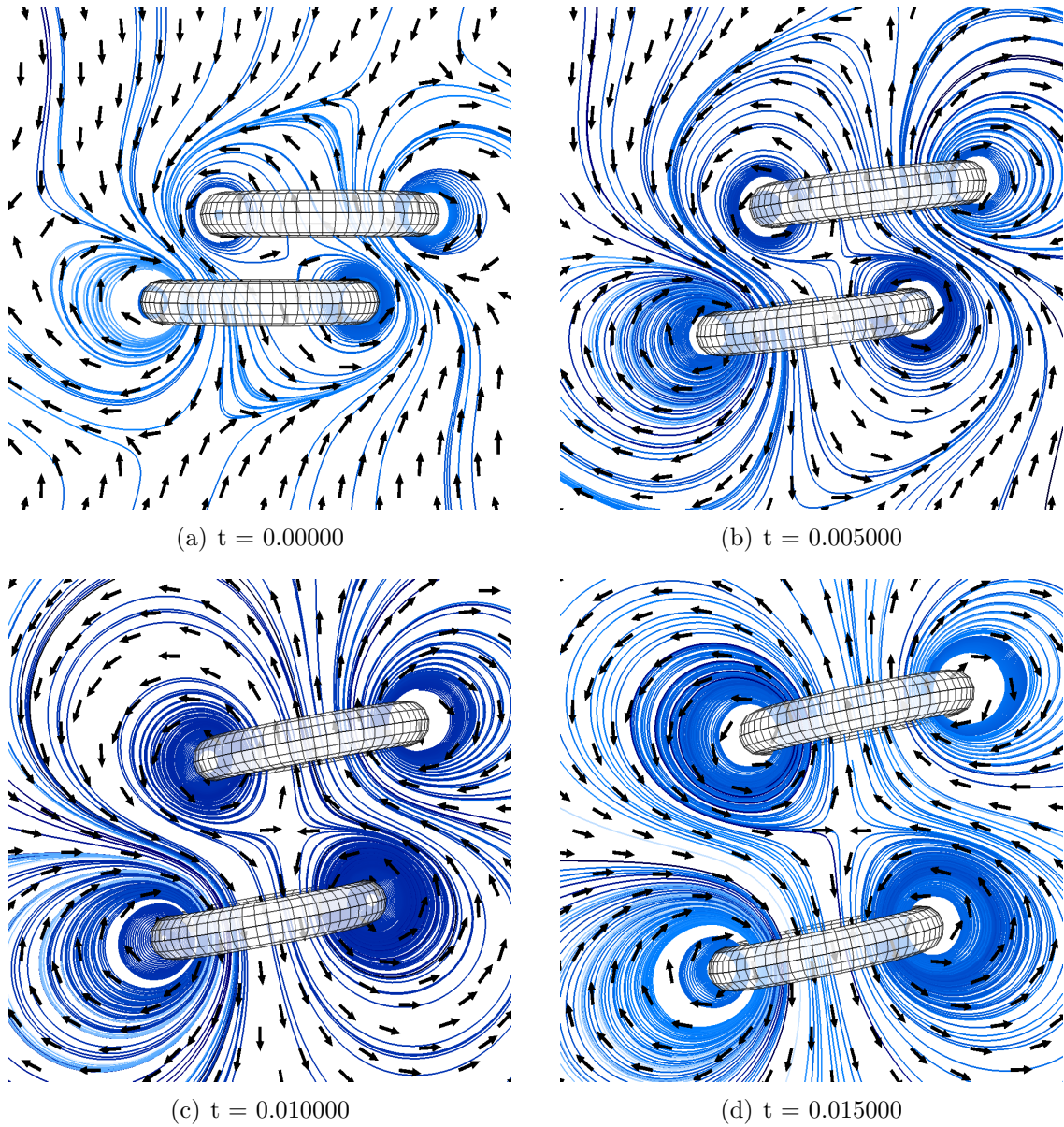
(a) t = 0.00000

(b) t = 0.005000

(c) t = 0.010000

(d) t = 0.015000

Figure 3.16: Two tori are placed back to back with a perturbation to the right in the x direction. They move away from each other with opposite translational velocity but same rotational velocity (counter-clockwise). Moreover, they show a tendency of getting away from the alignement (see figure 3.18(b)). This experiment is exactly the same as the experiment in figure 3.15 with time reversed. The arrows imply the direction of the fluid at that point, and not the magnitude of the velocity. The streamlines are shown as solid lines.
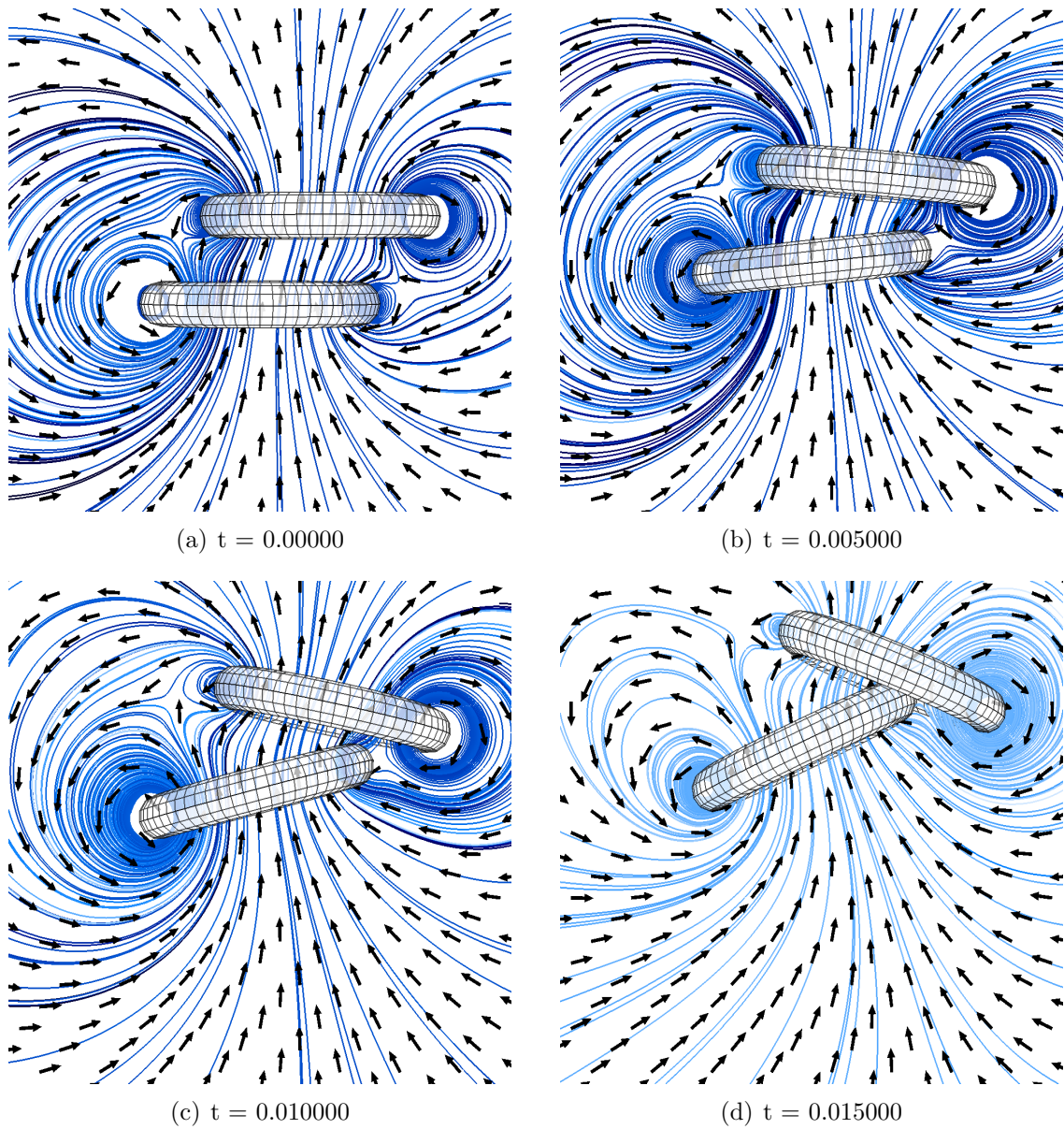
(a) t = 0.00000

(b) t = 0.005000

(c) t = 0.010000

(d) t = 0.015000

Figure 3.17: Two tori are placed face to back with a perturbation to the right in the x direction. They move with opposite rotational velocities until they are far away from each other or they collide. The two tori in figure (d) do not collide with each other, which is confirmed in figure 3.22(a). Figure 3.22(a) shows the figure (d) from another view point. The arrows imply the direction of the fluid at each point, and not the magnitude of the velocity. The streamlines are shown as solid lines.
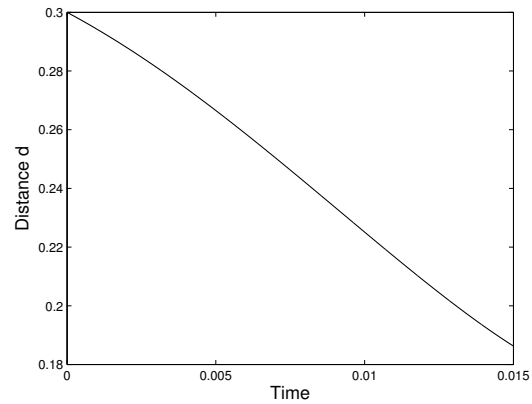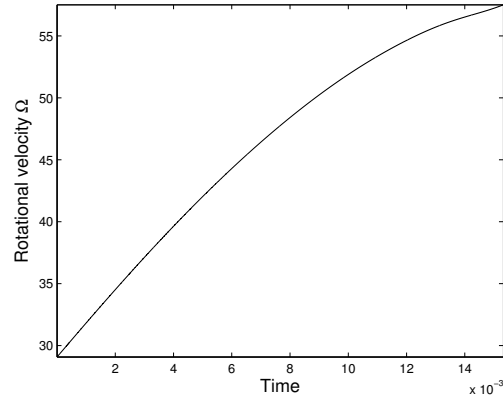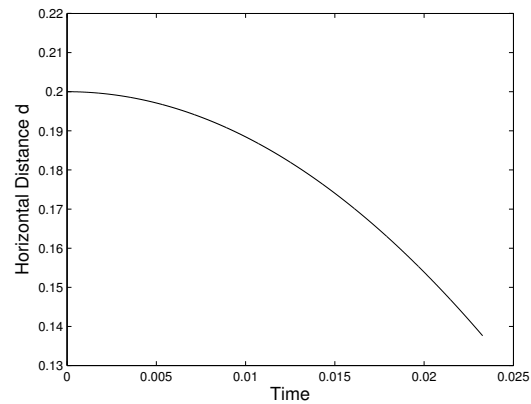
(a) perturbed face-to-face case
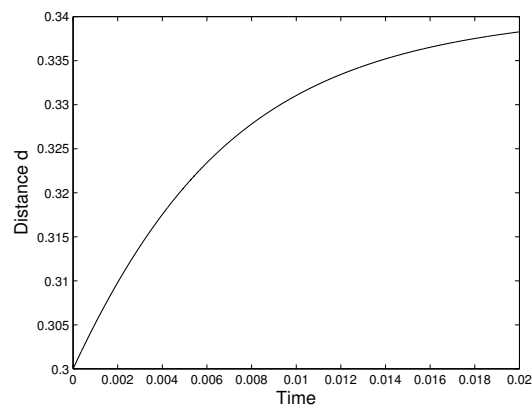
(b) perturbed back-to-back case

Figure 3.18: The distance d between the normals of two tori is shown with respect to time here. In perturbed face-to-face case (figure 3.18(a)), the initial distance is 0.3, and as time passes, the distance decreases. Centers of two tori are approaching to each other in the perpendicular direction. Therefore, alignment is observed in this case. In the perturbed back-to-back case (figure 3.18(b)), the initial distance is 0.3 too, but as time passes, the distance increases. Centers of two tori are moving away from each other in the perpendicular direction.

(a) The rotatonal velocity in perturbed face-to-face case.

(b) The horizontal distance between two side by side tori.

Figure 3.19: (a) The rotational velocity is shown with respect to time in the perturbed face-to-face case. As time evolves, the rotational velocity increases. (b) The horizontal distance between two side-by-side tori is shown with respect to time. It shows that the distance in x direction is decreasing as the time evolves. This implies that the tori are moving toward each other in x direction.
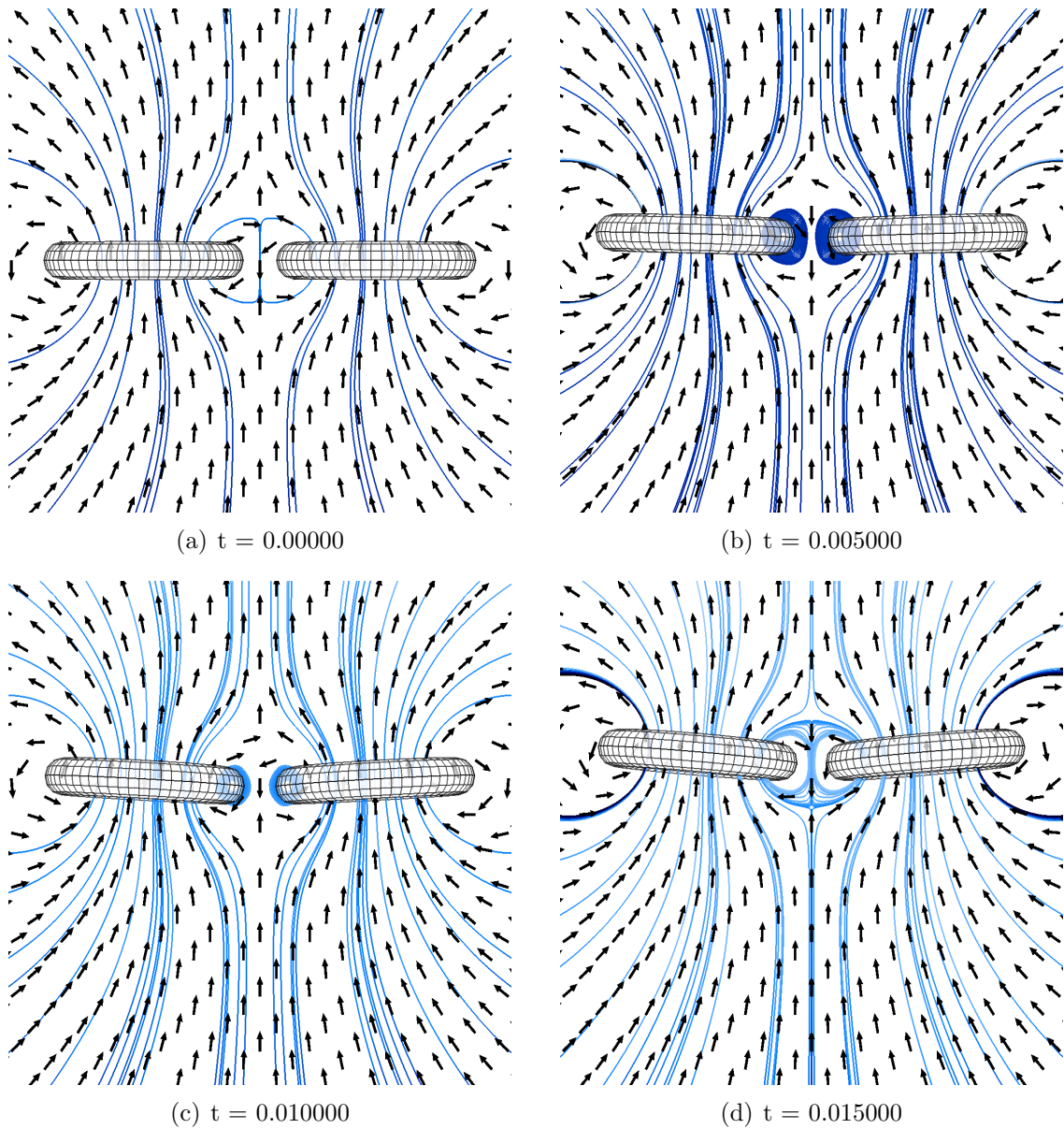
(a) t = 0.00000

(b) t = 0.005000

(c) t = 0.010000

(d) t = 0.015000

Figure 3.20: Two tori are placed side by side. They move toward each other with translational velocities symmetric w.r.t. y-z plane but with opposite rotational velocity. They have a tendency to align themselves, which means they will turn into the face-to-face case eventually. The arrows imply the direction of the fluid at each point, and not the magnitude of the velocity. The streamlines are shown as solid lines.

clockwise, and that of the upper one is counterclockwise (seen from negative y axis). The tori are folding like the case of two side-by-side tori (see figure 3.21(b) and (c)). The two tori do not collide in figure 3.21(c). This can be observed from the figure 3.22(b), which is the figure 3.21(c) with camera zoomed in. As they get close, the upper one and the lower one experience increasing clockwise push and the increasing counterclockwise push respectively. The upper one and the lower one finally start rotating clockwise and counterclockwise respectively (see figure 3.21 from (c) to (d)). Then they move away with decreasing rotational speeds. With the rotational velocities turn back as their originial directions, the two tori return back to their original alignment (see figure 3.21 from (g) to (h)). As one can see from figure 3.21, the trajectory of these two tori are periodic.

3.4 Interaction of three tori

In this section, we consider the interaction between three tori. In figure 3.23(a), we place the three tori abreast facing upward. From the discussion in previous sections, any two of them will translate and rotate toward each other. Since the effect from the rightmost torus to the middle one is neutralized by that from the leftmost one, the middle one will translate without rigid rotation. The other two tori rotate toward the middle one. We are expecting the outermost two tori to rotate until the three of them form an equilateral triangle from the view of the negative y axis. However, the results with a limited time can be shown in figure 3.23(b) since the tori are too close that a finer discretization and a smaller time step are required from then on.

Figure 3.24 shows another configuration of the three-tori with their centerline planes located on the x-y plane and their centers forming an equilateral triangle.

(a) t = 0.00000

(b) t = 0.13000

(c) t = 0.05000

(d) t = 0.15000

(e) t = 0.10000
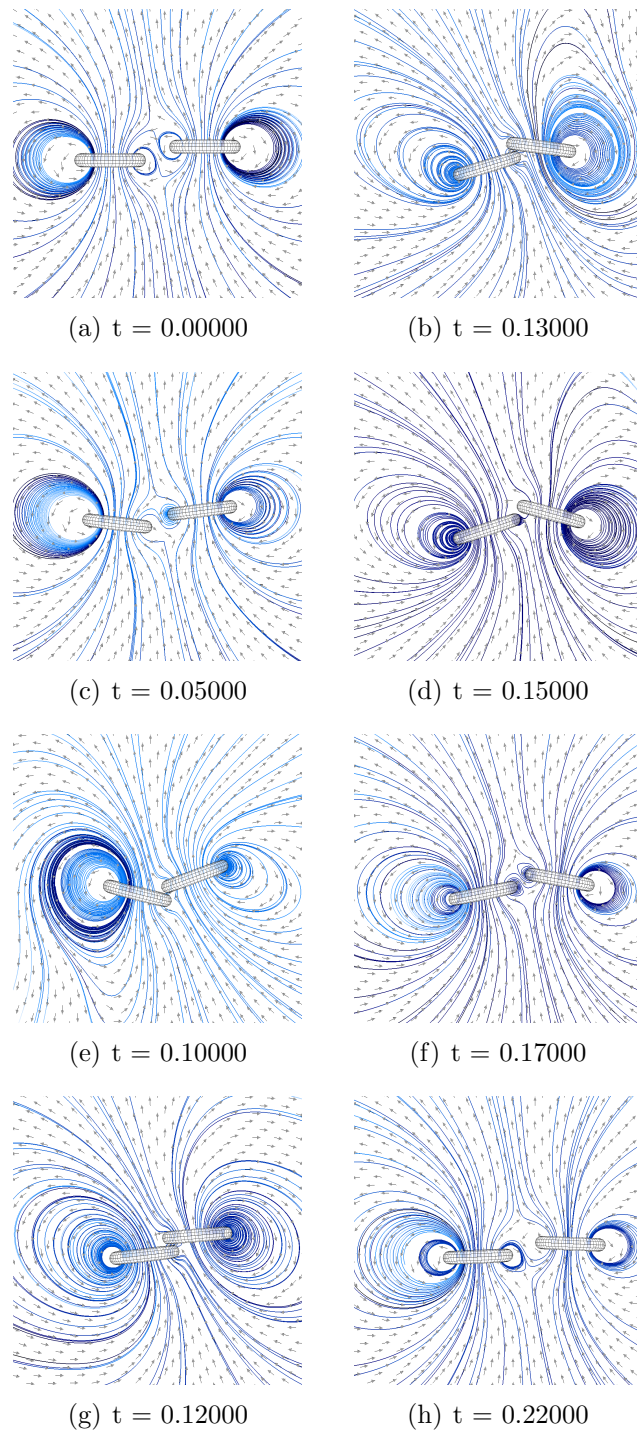
(f) t = 0.17000

(g) t = 0.12000

(h) t = 0.22000

Figure 3.21: Two tori are placed in the perturbed face-to-back case. They are moving with a periodic trajectory in this case. The figures are shown with a up-moving focus frame of a speed 30. Figure (c) is shown up close in Figure 3.22(b) to show that no collision happens even though they seem very close. The arrow implies the direction of the fluid at that point, and not the magnitude of the velocity. The streamlines are shown as solid lines.
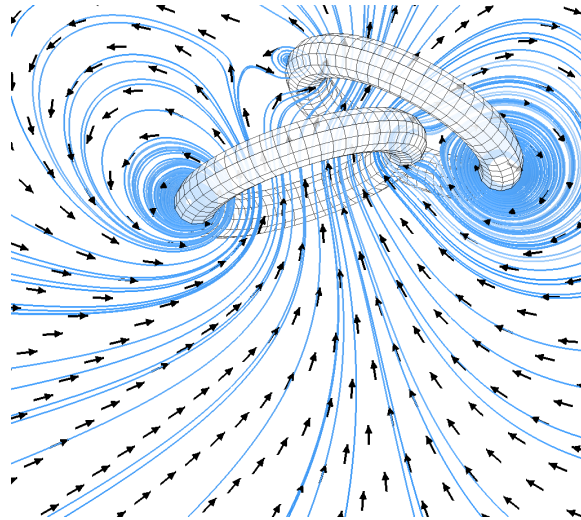
(a) Perturbed face to back case
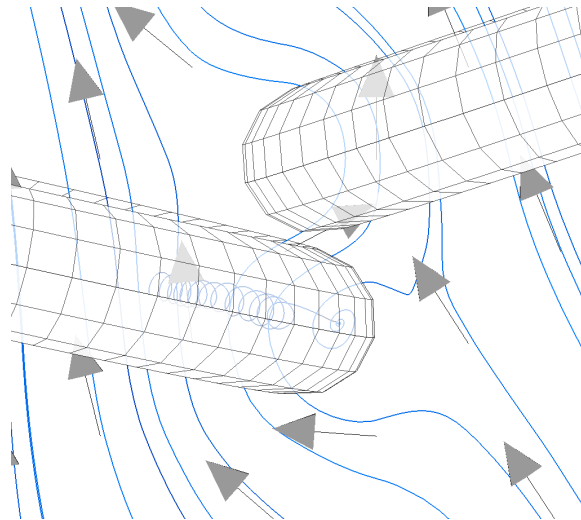
(b) Periodic case

Figure 3.22: Figure 3.22(a) is another view of the figure 3.17(d). It shows that the two tori do not collide with each other. Figure 3.22(b) is obtained from the figure 3.21(c) with camera zoomed in. The gap between two tori is evident, which means the two tori do not collide with each other.
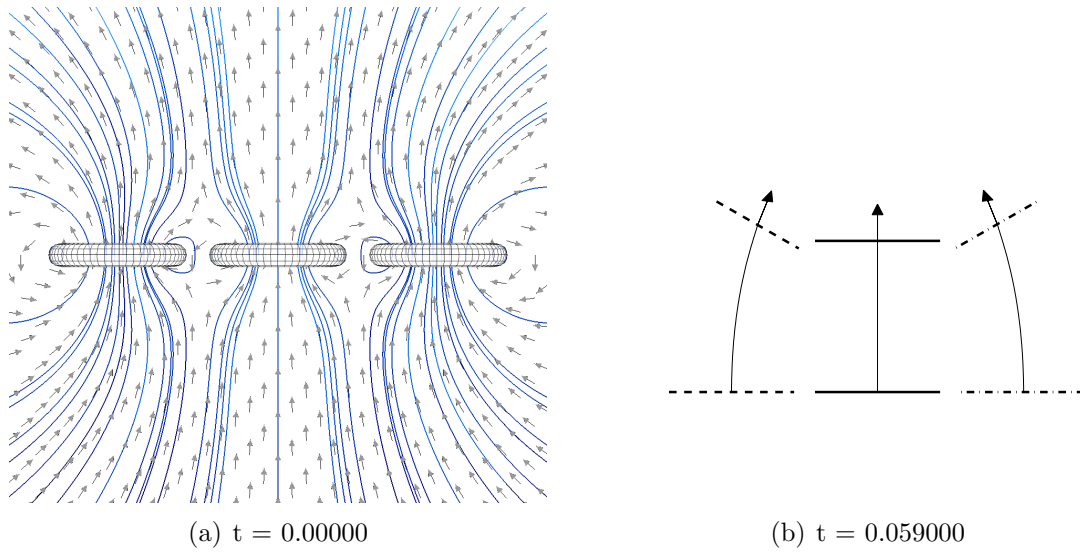
(a) t = 0.00000   (b) t = 0.059000

Figure 3.23: Three tori are placed abreast. Figure (a) shows the initial placement of the three tori with streamlines and flow fields around them. Figure (b) shows the three tori represented by segments(the leftmost by dash, the rightmost by dash-dot and the middle one by solid line), and the trajectories (in solid lines) of the centers of the three tori within a limited time. The figure is obtained from the numerical data. It shows that the outer two move and rotate toward the middle one, which translates upward in between. All the views are seen from the negative y axis.

Each one of them rotates toward the other two if the interaction of only two tori is considered. The combination of the effects from the other two tori to one of them results in the rotation in the direction of the angle bisector of the equilateral triangle (formed by the centers of the three tori). We are expecting the three tori will rotate until they form a equilateral triangle from the view of the positive z axis. However, a finer discretization mesh and a smaller time step are required for them to proceed in this numerical experiment.

When the three of tori are placed in tandem with all their normals pointing upward (see figure 3.25), the three co-rotating tori experience zero rigid rotation, but translate with different translational velocities. The middle one is boosted from the

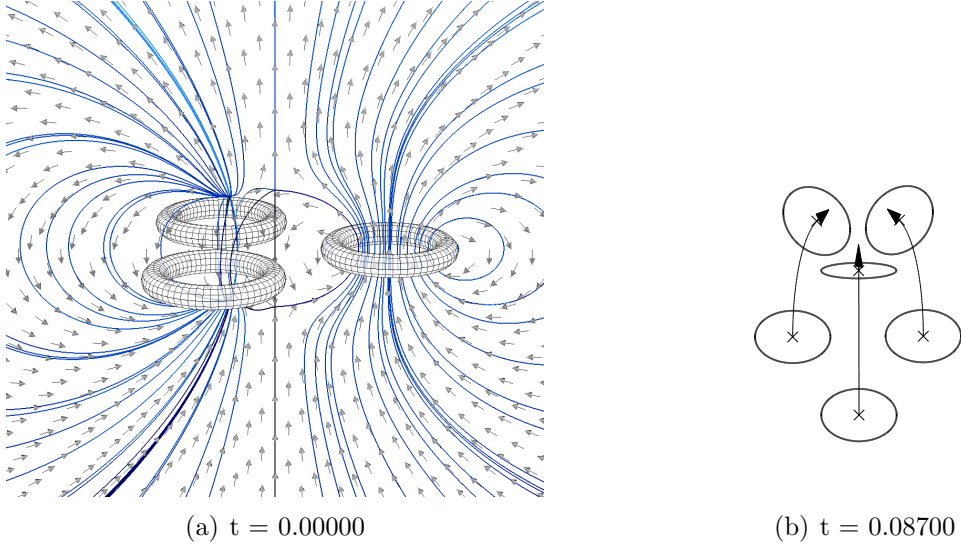(a) t = 0.00000   (b) t = 0.08700

Figure 3.24: Three tori are placed in x-y plane with centers forming an equilateral triangle with all normals pointing upward. Figure (a) shows the streamlines and flow fields in the plane y = 0. Figure (b), which is obtained from the numerical data, shows that the relative motion of each torus (represented by a circle) is to rotate to face the direction of the center of the triangle, and move towards it. The marker 'x' shows the center of each torus.

top one and the bottom one and it will move faster than the other two. Between the top one and the bottom one, when the middle one is located below the middle point of the segment connecting two centers of the the top one and the bottom one, the bottom one is moving faster than the top one. Otherwise, the top one is moving faster than the bottom. However, since the middle one is always faster than the top one, collision between the top one and the middle one might be expected to happen in this case.

Lastly, we study the pattern that inserting a rotating torus with normal pointing upward between two counter-rotating tori (see figure 3.26). The top one is inhibited from both the bottom and the middle ones. Its speed will be the slowest among the three. Since the middle is inhibited more from the top than the bottom one, the
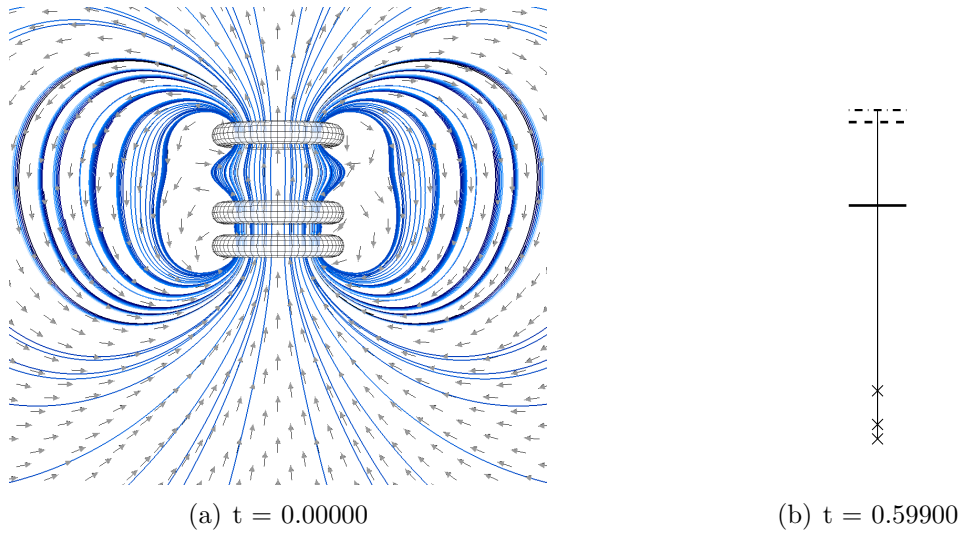
(a) t = 0.00000   (b) t = 0.59900

Figure 3.25: Figure (a) shows the three co-rotating tori placed in tandem with all normals pointing upward. The streamlines and flow fields are shown too. In figure (b), the three parallel segments represent the positions of the three tori at time 0.599. The marker 'x' shows the initial location of the center of each torus. The vertical lines are the trajectories of the centers of the three tori, which are moving upward.

bottom one will have the largest speed. Both the middle and the bottom ones are moving upward, but the moving direction of the top one is affected by the distances to the other two tori. Figure 3.26 shows that the top one is moving downward and the rest are moving upward at the begining. When the top one and the middle one are becoming close, all three are moving upward. As time evolves, the velocity of the top is increasing, but that of the middle and that of the bottom are decreasing. When the top one and the middle are very very close, the three almost attain the same translational velocities. Finally, collision might occur because the middle one is always moving faster than the top one.

Above all, we have shown that the interaction of three tori can be roughly analyzed from the superposition of the interaction of two tori. The same analysis can give insight on the interaction of four or more tori. For example, having n tori with
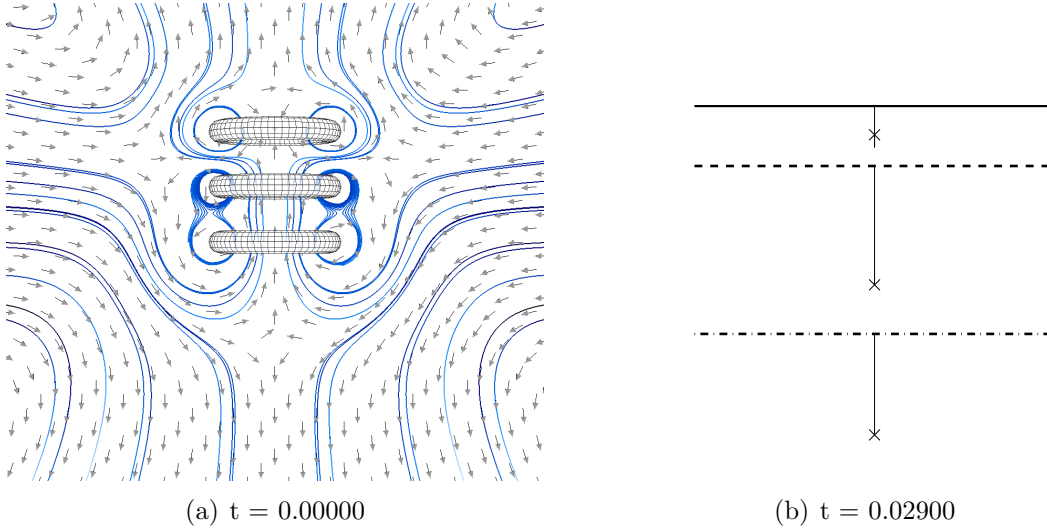
(a) t = 0.00000   (b) t = 0.02900

Figure 3.26: Figure (a) shows three tori placed in tandem with the top one moving downward and the other two upward at the beginning. The marker 'x' in figure (b) shows the initial location of the center of each torus. The vertical lines are the trajectories of the centers of three tori. Figure (b) shows that the top one changes moving direction to upward at some time (the top trajectory has a part below the top marker 'x'). Finally, all three tori are moving upward with different velocities. The bottom one is the fastest, the middle one second and the top the slowest. Collision might occur.

all normals pointing upward and centers forming an equilateral polygon on the x-y plane, we expect that they will rotate toward the direction of the angular bisector, which behave like a flower folding its petals.

3.5 Comparison between interaction of finite vortex dipoles and that of tori

In this section, we first reproduce the numerical results of the finite vortex dipole interaction in [33]. Then we argue that between these minimal swimmers in 2D and the 3D toroidal swimmers result in similar trajectories of pairs.

The numerical results of the dynamic interactions of finite vortex dipoles are presented here and for parameters, we take them the same as in [33]. Each finite vortex dipole is specified with a self-induced speed equal to 1 by assigning vortex strength $\Gamma_n = 1$ for each n and fixed dipole length $l_n = l = 1/(2\pi)$ for each n. All other parameters or placements are taken directly from the paper [33]. For each case below, we initially place the two finite vortex dipoles a horizontal distance b and vertical distance h apart, and solve the equations (2.38) and (2.39) numerically by applying ODE45 in MATLAB with relative and absolute tolerances of 10^{-6} and 10^{-8} respectively. The trajectory of the center of each dipole is plotted for a total time $t = 5$.

Our results shown in figure 3.27 is exactly the same as the figure 7 in [33]. The only difference is to obtain the figure (e), we set the final time $t = 6$. In order to show the similarity of interaction between tori and finite vortex dipoles, we intentionally increase the length of the each finite vortex dipole to $l_n = 1$. With a height $h = 1$ fixed, figure 3.28(a) shows the changes of the transaltional speed and the rate of change of the angle $\dot{\theta}$ of the upper dipole with respect to the horizontal distance b. The self propelled speed is also plotted for reference. As we can see, the translational velocity of the finite vortex dipole decreases to a speed less than the self-propelled speed and then increases and approaches to the self-propelled speed as the horizontal distance b increases. However, the effect of the distance to the angle speed of the upper finite vortex dipole is deceasing to the global minimum (negative), then increasing to a global maximum (positive), and eventually decreasing to 0. Let's denote the horizontal distance d_1 where the translational speed is equal to the self-propelled speed, and d_2 where the angle speed is equal to zero. Then, d_1, d_2 are different from different length l_n. Moreover, d_1 and d_2 both are increasing as the
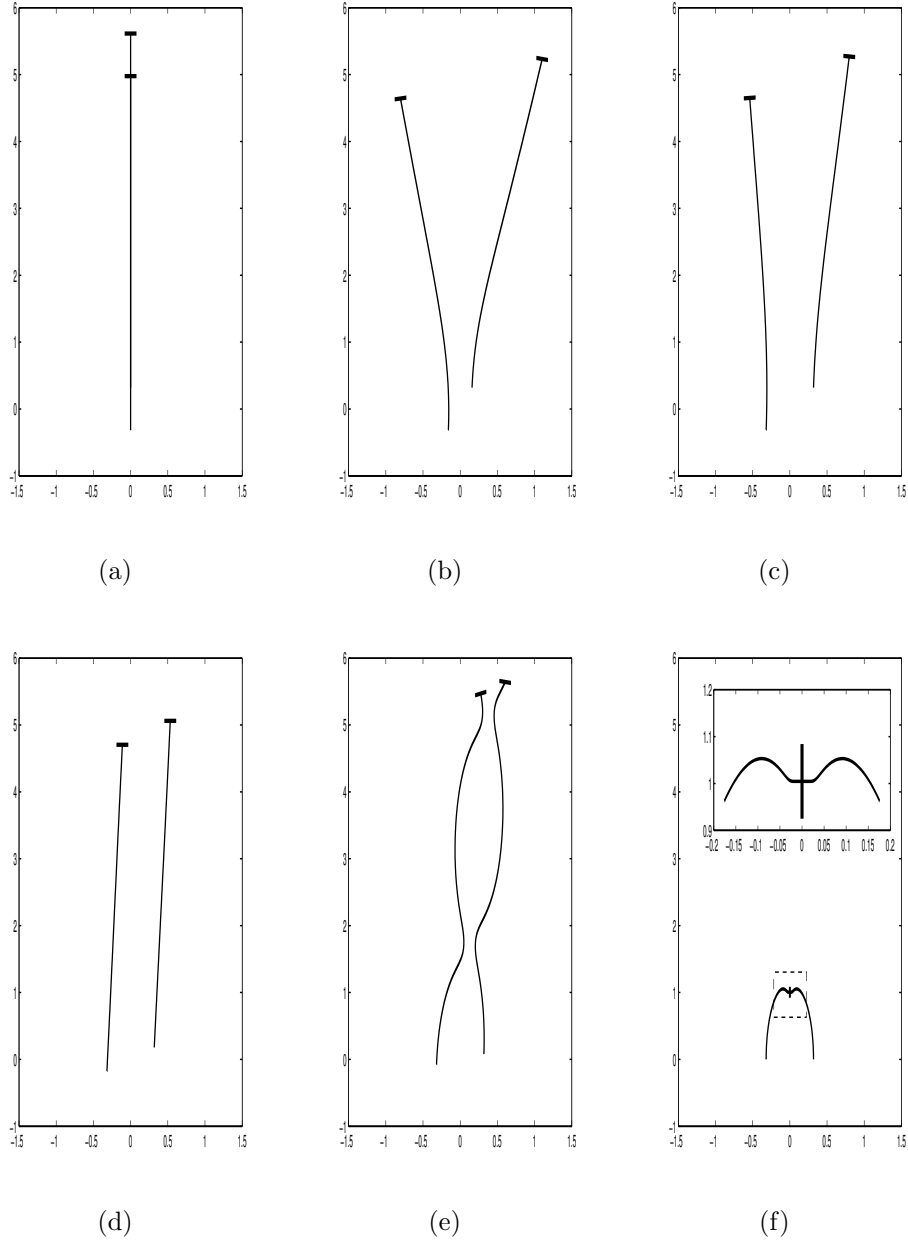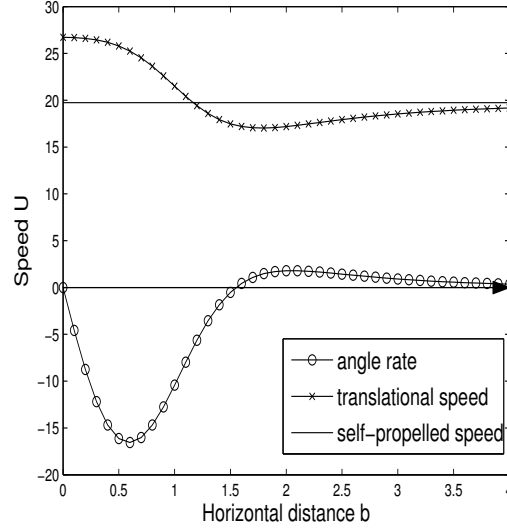
Figure 3.27: Interaction of two finite vortex dipoles in two dimensional space aligned with different vertical distance h and horizontal distance b is shown. The line is the trajectory of the center of each dipole, and the bold line segment at the end of each trajectory is used to represent each dipole at final time t = 5. The final time for (e) is t = 6. The ends of the line segment in bold are where the vortices are located. (a) $h = 4l, b = 0$ (b) $h = 4l, b = 2l$ (c) $h = 4l, b = 4l$ (d) $h = 2.25l, b = 4l$ (e) $h = 1l, b = 4l$ and (f) $h = 0, b = 4l$.

height h is increasing. Similar figure (figure 3.28(b)) can be obtained from the study of the tori with $h = 0.3$. The similarity in change of speed and rate of change of the angle implies the similarity in the interaction patterns would be possible. Figure 3.29 shows six patterns from the interaction of two tori with equal radius of centerline $r_c = 0.5$ and equal radius of tube $r_h = 0.1$. Comparing figure 3.27 and figure 3.29, they are almost the same, but with different initial placements.

When two finite vortex dipoles are placed in tandem ($d = 0$), the angle speed is zero. Thus, the dipoles do not rotate. The "dipole drafting" phenomena, which means the dipoles help each other in translating forward, happens to both dipoles (figure 3.27(a)) and so do tori (Figure 3.13 and 3.29(a).). As the horizontal distance d increases, the angle speed (upper one) is negative. The upper one (torus or dipole) rotate clockwise and the lower one acts in opposite way. Divergence or eventually collision (Figure 3.17, 3.29(b), 3.29(c) for tori and 3.27(b), 3.27(c) for finite vortex dipoles) will be observed. When d increases to d_2, they (dipoles or tori) will translate without rotation (Figure 3.27(d) for dipoles and figure 3.29(d) for tori. When $d > d_2$, the upper one will rotate counterclockwise and the lower one will rotate clockwise at first. The dipoles (figure 3.27(e)) or tori (figure 3.21and figure 3.29(e).) begin to oscillate with periodic trajectories. However, since the translational speed of the torus is usually much larger (at least 10 times in our cases) than its angular speed, it is not so immediate to observe this oscillation in most cases. When d goes to infinity, their interaction is so trivial that the objects will move much like a single object. This coincides with the tendency of the translational speed and the angular speed in figure 3.28. When two finite vortex dipoles (figure 3.27(f)) or tori (figure 3.20 and figure 3.29(f).) are placed abreast (h = 0), they will translate and rotate toward each other. Same comparison can also be observed from the study of three dipoles and

(a) Interaction between two finite vortex dipoles
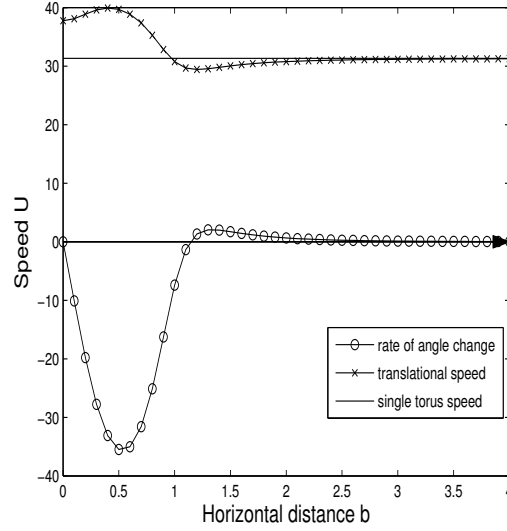
(b) Interaction between two tori

Figure 3.28: The translational speed and angular speed of (a) a pair of dipoles with height $h = 1$ and (b) tori with height $h = 0.3$ are plotted against the horizontal distance b. The translational speed increases, decreases, and then again increases. However, here the angular speed is decreasing, then increasing and finally decreasing. The distance, d_1, is the distance where the translational velocity is equal to the self-propelled speed and d_2 is the distance where no rotation happens to each torus.
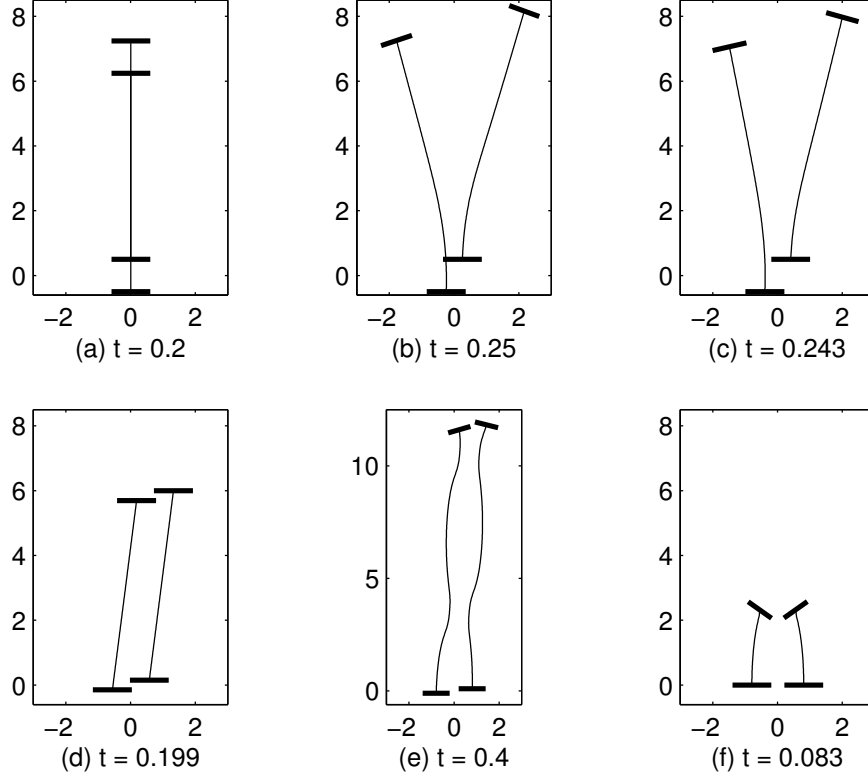
three tori.

Figure 3.29: Interaction of two tori in three dimensional space aligned with different vertical distance h and horizontal distance b. The line is the trajectory of the center of each dipole, and the bold line segment at the beginning or the end of each trajectory is used to represent each torus. The tori here have equal radius of centerline $r_c = 0.5$ and radius of tube $r_h = 0.1$. (a) $h = 1, b = 0$ with final time t $= 0.2$. (b) $h = 1, b = 0.5$ with final time t $= 0.25$. (c) $h = 1, b = 0.8$ with final time t $= 0.243$. (d) $h = 0.3, b = 1.13796$ with final time t $= 0.199$. (e) $h = 0.2, b = 1.6$ with final time t $= 0.4$ and (f) $h = 0, b = 1.6$ with final time t $= 0.083$.

Chapter 4

Models of dinoflagellate

4.1   Motion of dinoflagellate

In this section, we choose an idealized model of a dinoflagellate to be a sphere surrounded by a thin torus (see Figure 4.1(a) and 4.1(b)) with a prescribed surface tangential velocity on the surface of the torus. The radius of the sphere is represented by r_s with default value equal to 0.4. The number of points on the sphere is $N_s = 1600$. The radius of the centerline of torus is $r_c = 0.5$ and the radius of the tube is $r_h = 5.7498e - 02$. The number points in each cross-sectional circle is $M = 12$ and the number of cross-sections along the centerline is $N = \lceil \frac{12r_c}{r_h} \rceil = 105$. The numerical result shows that the new model still moves in its normal direction, which is defined in last section as the moving direction of the inner part of the torus. However, its translational speed, which is 1.7228e+01, is larger than that of a single torus, which is 1.3280e+01, with the same surface tangential velocity. Thus, the existence of the sphere boosts the translational speed of the torus. Moreover, the streamlines and the flow field around the torus-sphere object in the plane $y = 0$ are shown in figure 4.1(c) and figure 4.1(d).

Let $s_0 = \frac{r_c}{r_h}$, which is the aspect ratio, $\lambda = \frac{r_s}{r_h}$, and ratio $U = \frac{U_{ts}}{U_t}$, where U_{ts}
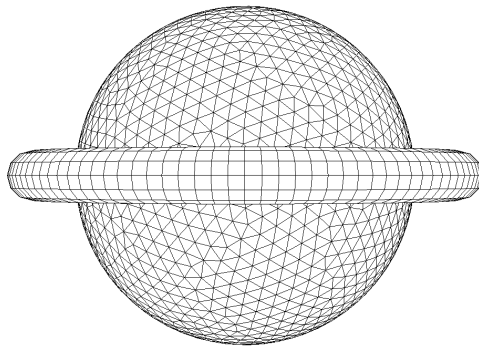
(a) model of dinoflagellate
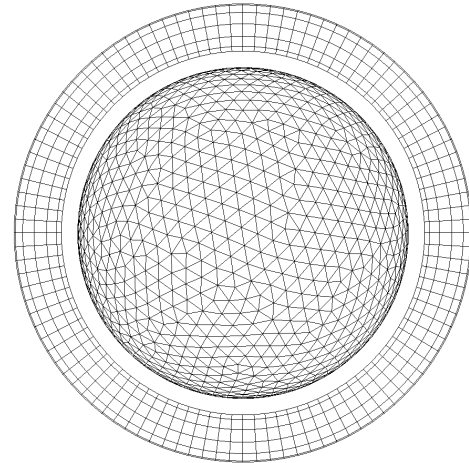
(b) the model viewed from the top
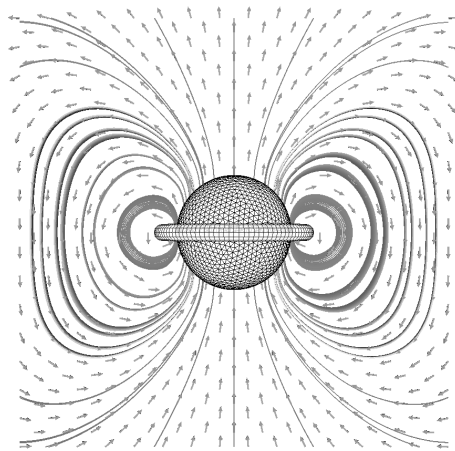
(c) streamlines and flow field around the model of dinoflagellate in the plane y = 0
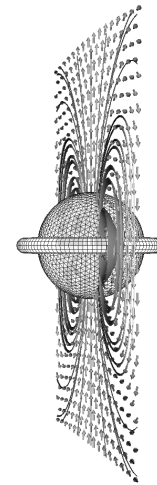
(d) streamline and flow field around the model of dinoflagellate in the plane y = 0 viewed from another angle

Figure 4.1: Model of dinoflagellate ((a) and (b)) are shown here from different view angles. Streamlines are shown with solid lines in (c) and (d) from two different view points. The arrows show the flow field not with the magnitude but the direction only.

and U_t are the translational velocities of the torus-sphere and the torus respectively. From the geometry of the model, $s_0 > 1$ and $0 < \lambda < s_0 - 1$. The choice of s_0 and λ are shown in colors in figure 4.2. The different color corresponds that different magnitude of the ratio U (see color bar). The closer the point (s_0, λ) is to the line $\lambda = s_0 - 1$, the larger the ratio U is. In other words, if the sphere filled in the whole hole of the torus, i.e. $\lambda = s_0 - 1$, the translational velocity of the torus-sphere will be the largest with fixed aspect ratio s_0. Independently, λ has a positive effect on the translational speed (see the right one in figure 4.3(c)), but s_0 shows a negative effect (see the left one in figure 4.3(c)). These facts imply that the increase in translational velocity depends on how narrow the gap between the torus and the sphere is. In figure 4.3(a) and 4.3(b), the ratio U is plotted with respect to s_0 or $\frac{1}{s_0}$ in x-axis and λ in y-axis respectively.
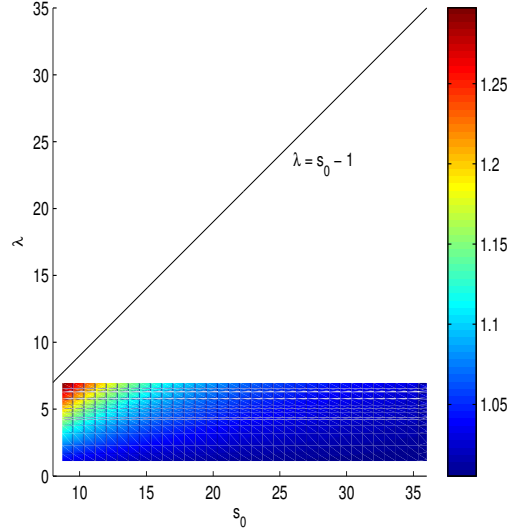
Figure 4.2: The restriction of s_0 and λ is that the points should be contained in the region $0 <= \lambda < s_0 - 1$. And our choice of s_0 and λ are shown in the color area. The color shows the magnitude of the ratio U between translational velocity of torus-sphere and torus.
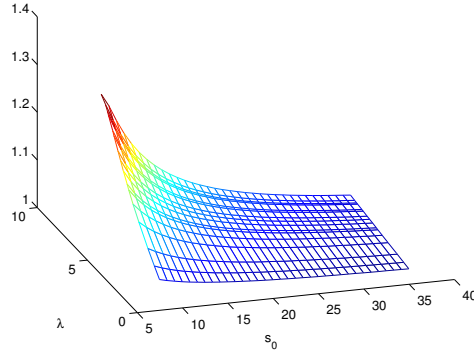
(a) The ratio U between the translational velocities of the torus-sphere and the torus v.s. s_0 in x-axis and λ in y-axis.
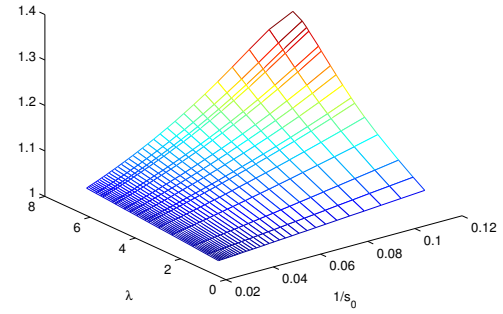
(b) The ratio U between the translational velocities of the torus-sphere and the torus v.s. $\frac{1}{s_0}$ in x-axis and λ in y-axis.
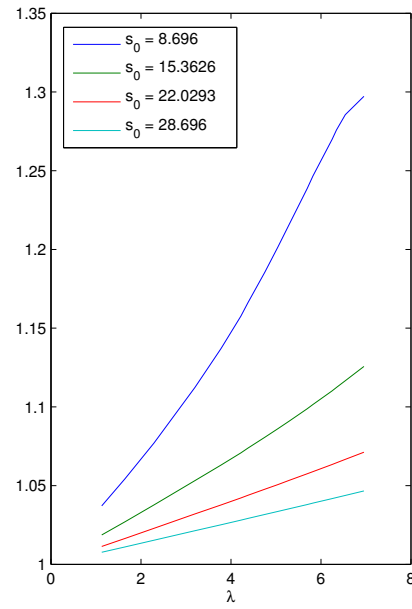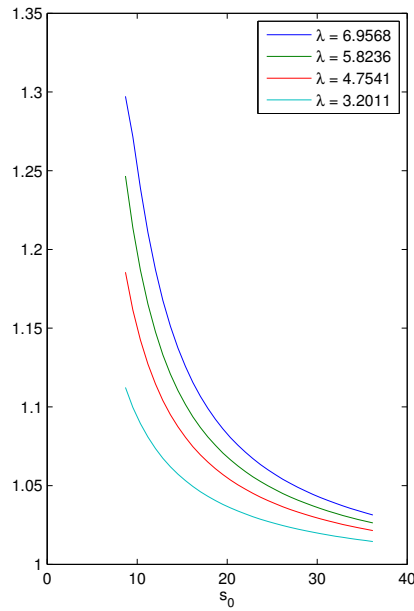
(c) The ratio U between the translational velocities of the torus-sphere and the torus v.s. s_0 (left) or λ (right) respectively.

Figure 4.3: Note that the larger the sphere is, the larger λ and the larger the boost in translational velocity to the torus-sphere when the aspect ratio is fixed. The effect decreases when the aspect ratio increases with fixed λ.

4.2   Swimming efficiency

Although the translational velocity is increased when a spherical body is placed inside the torus, we do not know whether the power needed to rotate the surface is increased or not. Thus, we would like to determine how efficient each swimmer is. In this part, the efficiency of a swimmer (see [12]) will be defined by the ratio between the power P_t expended by dragging the rigid body at velocity $\mathbf{U}$ and rotating it with a rotational velocity $\mathbf{\Omega}$ and the power P dissipated by the fluid viscosity, which is given by the integral over the boundary surface S:

$$P = \int_S (\sigma \cdot \mathbf{n}) \cdot \mathbf{u} dS$$

where $\mathbf{u}$ is the surface tangential velocity and σ are the surface stress tensor. And the other power P_t is given as follows:

$$P_t = \int_S (\sigma^t \cdot \mathbf{n}) \cdot (\mathbf{U} + \mathbf{\Omega} \times (\mathbf{x} - \mathbf{x}_c)) dS$$

where $\mathbf{U}$ and $\mathbf{\Omega}$ are the translational velocity and the rotational velocity respetively, and σ^t are the surface stress tensor when the object moves with a translational velocity $\mathbf{U}$ and rotational velocity $\mathbf{\Omega}$. Let the swimming efficiency be δ, then

$$\delta = \frac{P_t}{P}$$

If the object has only constant rigid translation motion, then

$$\delta = \frac{P_t}{P} = \frac{\int_S (\sigma^t \cdot \mathbf{n}) \cdot \mathbf{U} dS}{P} = \frac{\int_S (\sigma^t \cdot \mathbf{n}) dS \cdot \mathbf{U}}{P} = \frac{F^{(g)} \cdot \mathbf{U}}{P}$$

which is the definition of Lighthill's swimming efficiency δ (see [12]). Here $F^{(g)}$ is the external force used to drag the glider with translational velocity $\mathbf{U}$. Thus, the swimming efficiency defined here is a generalized formula which can be applied not only to the glider case but also to any body with rigid translation and rigid rotation.

From the definition, the power efficiency is a dimensionless scalar. The higher δ is, the more efficiency the swimmer is. With the definition of efficiency, we compare several models by their efficiencies: single torus, co-rotating tori, torus with sphere located at its center and helical ring. Figure 4.4 shows that although the translational velocity for each torus in co-rotating tori is larger than that of a single torus (see figure 4.4(a)), the total power expanded (see figure 4.4(b)) is more than twice as much as that of the single torus. Thus the efficiency of co-rotating tori is always less than that of a single torus, and the further the distance between two tori in co-rotating tori is, the closer the efficiency is to a single torus (see figure 4.4(c)). Therefore, although the co-rotating tori increase the swimming speed, the power dissipated by the fluid viscosity is increased even more, which results in less efficiency.

When comparing the efficiency of the single torus with that of the torus with a sphere at its center, the torus with a sphere placed at its center shows more efficient than a single torus (figure 4.5(a)). The larger λ is, the more efficient the torus-sphere swimmer is (figure 4.5(b)). This implies that the hole in the torus decreases the efficiency of the torus. When the torus were blocked by the sphere ($\lambda = s_0 - 1$), the swimmer will attain the maximum efficiency.

All in all, comparing between single torus, co-rotating tori and torus with sphere, the model of torus with sphere is superior over the other two cases. In fact,
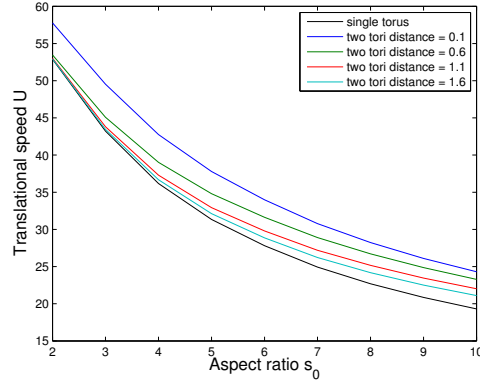
(a) aspect ratio v.s. translational velocity
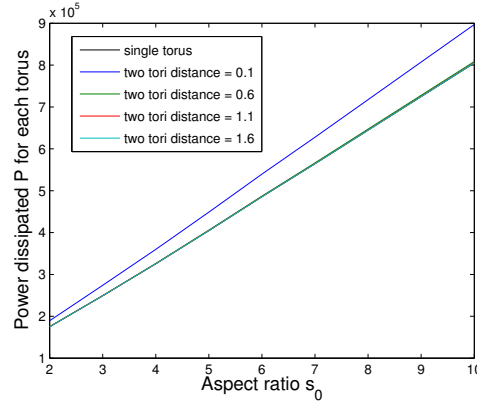
(b) aspect ratio v.s. power dissipated
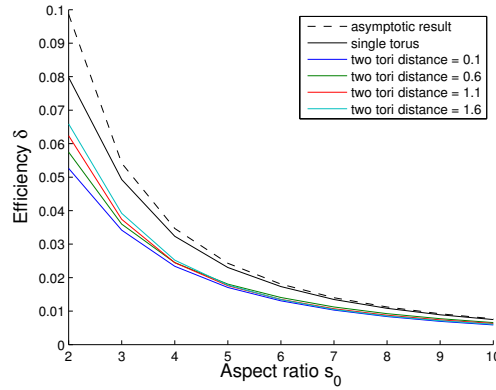
(c) aspect ratio v.s. efficiency

Figure 4.4: These figures show the translational velocity (figure 4.4(a)), power dissipated by the fluid viscosity (figure 4.4(b)) and the efficiency (figure 4.4(c)) v.s. aspect ratio s_0 of two co-rotating tori placed in tandem. Figure 4.4(a) and 4.4(b) shows the boost of the translational velocity for them and also the increase of the power dissipated by the fluid viscosity respectively. This results in the lower efficiency for the co-rotating tori (figure 4.4(c)). The dashed line in figure 4.4(c) is the asymptotic result of efficiency of a single torus, which was presented in formula (23) in [12].
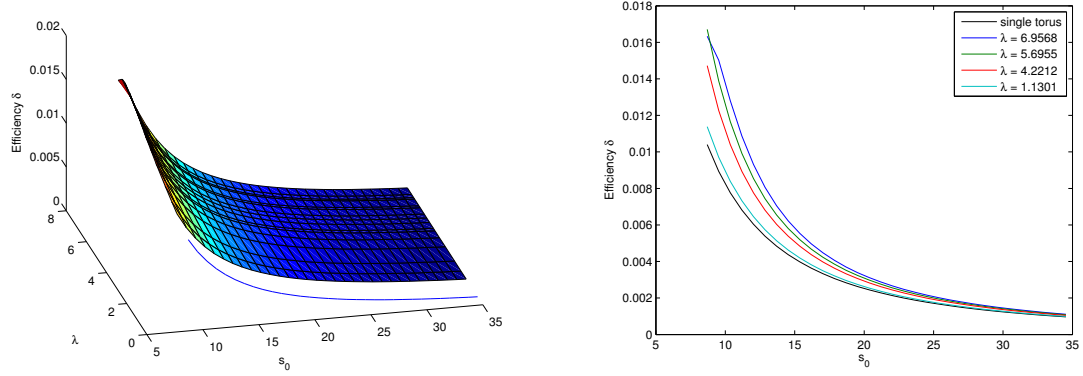
(a) The efficiency of torus-sphere and torus is plotted with respect to different s_0 in x-axis and λ in y-axis. The single curve displays the results from $\lambda = 0$.

(b) Comparison of efficiency between a single torus and a torus with a sphere. The curve in black is the efficiency (y-axis) of a single torus with respect to different aspect ratios (x-axis). The rest of the curves are the efficiencies of the torus with a sphere under several different λ.

Figure 4.5: The swimming efficiency decreases as the aspect ratio increases. For the torus with a sphere located at its center the efficiency is always larger than that of the torus without a sphere. The larger λ is, the more efficient the swimmer is.

[12] shows that the torus swimming with extensible surface tank treading obtains the largest efficiency when compared with the torus with constant surface rotation velocity (model used in this thesis), the torus with tank treading of incompressible membrane, the rotating helical flagellum [36], beating flexible filament [37], the Purcell's three-link swimmer [38, 39], locomotion by virtue of shape strokes [40, 41] and others. Taking our comparison into consideration, we expect to see that the torus with extensible surface tank treading and a rigid body inside will be superior to all mentioned above.

4.3 Helical tube near wall

4.3.1 Introduction

In the section, we return to the model of a dinoflagellate to study the effect of a nearby wall to the movement of its flagellum as a helical tube. The helical tube

has been introduced in section 3.2.2 and the equations for its centerline are given in equation (3.4). Here, we are going to study the helical tube with the baseline located at the y-z plane

$$
\begin{cases}
x(s,t) &= R\cos\left(\frac{2\pi s}{\lambda} - \omega t\right) \\
y(s,t) &= \left[r - R\sin\left(\frac{2\pi s}{\lambda} - \omega t\right)\right]\cos\left(\frac{s}{r}\right) \\
z(s,t) &= \left[r - R\sin\left(\frac{2\pi s}{\lambda} - \omega t\right)\right]\sin\left(\frac{s}{r}\right).
\end{cases}
$$

The helical tube is a cylindrical tube along its centerline with a radius r_h. The movement of the helical tube under the effect of the wave amplitude, the number of pitches and slenderness had been studied in [7] and is also presented in section 3.2.2. However, the effect of the nearby wall to the motion of the dinoflagellate is also of importance from the view of their living enviroment. We are going to study the effect of the wall from two models: toroidal glider and force free swimmer. Sometimes, an object with symmetric shape will be used to isolate different types of effects from the total effect. Following the parameters in [7], number of pitches is $n_p = 3$, amplitude is $R = 0.09$, radius of centerline is $r = 0.5$, angular speed is $\omega = 0.1$ and radius of tube is $r_h = 0.035$. The velocity on the centerline $\mathbf{u} = (u,\ v,\ w)$ is computed from the derivative of the equations of the centeline with respect to time t.

$$
u(s,t) = R\omega \sin\left(\frac{2\pi s}{\lambda} - \omega t\right)
$$
$$
v(s,t) = R\omega \cos\left(\frac{2\pi s}{\lambda} - \omega t\right)\cos\left(\frac{s}{r}\right)
$$
$$
w(s,t) = R\omega \cos\left(\frac{2\pi s}{\lambda} - \omega t\right)\sin\left(\frac{s}{r}\right).
$$

Then, we introduce the three vectors $\{\mathbf{t}, \mathbf{n}, \mathbf{b}\}$ which form a right-handed orthonormal triad at position s along the curve at time t. First, let $\alpha(s, t) = (x_s, \ y_s, \ z_s)$, where

$$x_s(s, t) = -\frac{2\pi R}{\lambda} \sin\left(\frac{2\pi s}{\lambda} - \omega t\right)$$

$$y_s(s, t) = -\left(r - R\sin\left(\frac{2\pi s}{\lambda} - \omega t\right)\right) \sin\left(\frac{s}{r}\right) / r - \frac{2\pi R}{\lambda}\cos\left(\frac{2\pi s}{\lambda} - \omega t\right)\cos\left(\frac{s}{r}\right)$$

$$z_s(s, t) = \left(r - R\sin\left(\frac{2\pi s}{\lambda} - \omega t\right)\right) \cos\left(\frac{s}{r}\right) / r - \frac{2\pi R}{\lambda}\cos\left(\frac{2\pi s}{\lambda} - \omega t\right)\sin\left(\frac{s}{r}\right).$$

Then, we define the triad $(\mathbf{t}, \ \mathbf{n}, \ \mathbf{b})$ as

$$\mathbf{t} = (t_1, t_2, t_3) = \frac{\alpha(s)}{|\alpha(s)|}$$

$$\mathbf{n} = (0, \frac{t_3}{\sqrt{t_3^2 + t_2^2}}, -\frac{t_2}{\sqrt{t_3^2 + t_2^2}})$$

$$\mathbf{b} = \mathbf{t} \times \mathbf{n}$$

Note that the tangent $\mathbf{t}$ would never be $(1, 0, 0)$ or $(-1, 0, 0)$ that the above definition of $\mathbf{n}$ is well-defined. Under the triad $(\mathbf{t}, \ \mathbf{n}, \ \mathbf{b})$, the points $\mathbf{x}$ on the helical tube can be represented as:

$$\mathbf{x} = (x(s, t), y(s, t), z(s, t)) + r_h\mathbf{n} \cdot \cos(\phi) + r_h\mathbf{b} \cdot \sin(\phi) \qquad (4.1)$$

where (x, y, z) is the point on the centerline and ϕ is the angle in the cross-sectional plane. Here, $\mathbf{t}$ is the tangential vector. We remark that these definitions are different from the actual "normal" and the actual "binormal"

$$\tilde{\mathbf{n}} = \frac{\mathbf{t}'(s)}{|\mathbf{t}'(s)|}$$

$$\tilde{\mathbf{b}} = \mathbf{t} \times \mathbf{n}$$

Although different set of sample points are obtained, they just represent the surface the helical ring in different way. However, we do not know whether they will make a difference in the results. Then the velocity at the point $\mathbf{x}$ on the surface of the helical tube will be

$$\mathbf{u} = \frac{d\mathbf{x}}{dt} = (x_t, y_t, z_t) + r_h \cos(\phi)\frac{d\mathbf{n}}{dt} + r_h \sin(\phi)\frac{d\mathbf{b}}{dt} \tag{4.2}$$

The method of regularized Stokeslets with images will be implemented here and the blob size will be chosen as $\frac{7}{12}\varepsilon_0$, where ε_0 is the average distance between linked points on the discretized surface, the blob size validated as the closest agreement between velocities computed using the slender body theory and those computed using the method of regularized Stokeslet in [7]. The number of points in each cross-sectional plane is $M = 6$ and the number of cross-sections is $N = 110$. The total points on the surface of the helical ring is $N_p = 660$.

Before starting the validation of our numerical method, first we examine how a point on the helical tube moves in time. Figure 4.6 and 4.7 show that each point in the centerline moves along a circle and the trajectory of the centerline forms a torus. Also, the points on the surface are not rotating along the normal to the centerline plane, but are moving along the centerline of the helical ring (see figure 4.6).

4.3.2 Validation

The strength of the image method has been introduced in [31] by studying several examples. One of the examples in that paper that we are going to present here is a ball moving parallel and perpendicular to an infinite wall in Stokes flow with velocity 0 on the wall. We examine how the wall affects the drag force on the ball. In [42], a non-dimensionalized force F^* is computed with analytic formula ob-

(a) t = 0   (b) t = 10   (c) t = 30

(d) t = 40   (e) t = 50   (f) t = 63
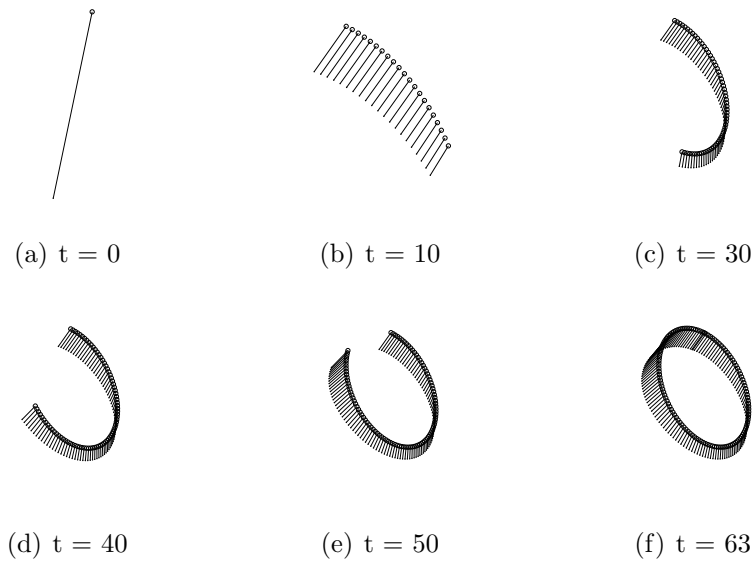
Figure 4.6: The particle line (dot plot) of a point on the surface of the helical tube is plotted with comparison to the trajectory of the centerline point (circle plot), which is on the same cross-sectional plane as the point on the surface. The trajectory of the centerline point is a circle. The trajectory of the surface point is an ellipse.

(a) t = 0   (b) t = 10   (c) t = 30

(d) t = 40   (e) t = 50   (f) t = 63
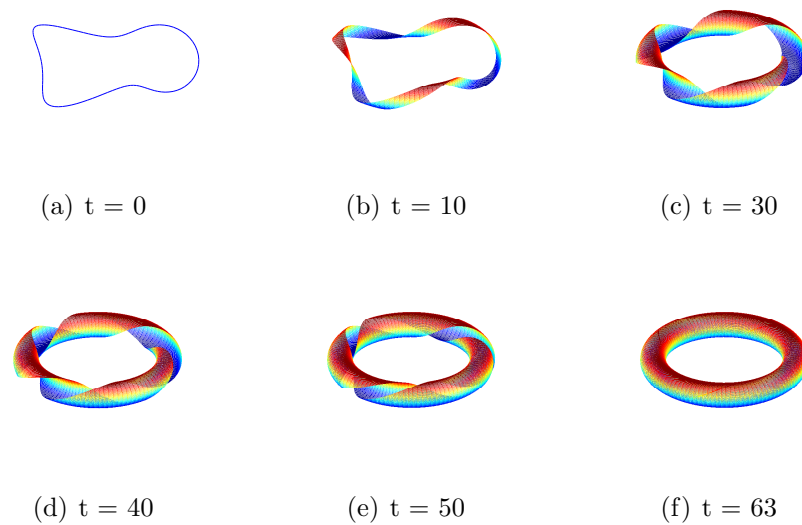
Figure 4.7: The non-hydrodynamic trajectory of the points on the centerline is plotted against the time. All trajectories form a torus over the course of one period.

tained by employing the bispherical coordinates when studying the fluid motion in highly viscous flow generated by the rigid sphere of radius a. In [43, 44], The exact solution to the slow viscous flow with a rigid sphere moving perpendicular to the infinite wall is obtained by applying bipolar coordinates. The analytical formula of non-dimensional force F^* will be computed with the analytical formula provided in [43] (for $d/a \geq 1.02$) and [44] (for $d/a < 1.02$). A comparison between the analytical solution and numerical result will be presented in both cases. In [31], the authors used the blob size $\delta = 0.22h^{0.9}$ and $\delta = 0.4h^{0.9}$ for the ball moving parallel to a wall and the ball moving perpendicular to the wall respectively, where $h = \sqrt{\frac{4\pi a^2}{N}}$ and N is the number of points on the sphere. Here [31], it was mentioned that these choices may not be the best, but we still expect to see our answer approches the exact answer as the finer discretization is applied. In [31], the authors used spherical coordinates to sample the points on the sphere, which are relatively even, and found that it turns out to be fine. However, the distribution of points on the sphere affects the results. Since an area with a cluster of points will result in over regularization in this area and the gap between clusters will be less represented by the sample points. Both cases will lead to the increase of the error in the result. Thus theoretically, a relatively evenly distributed points is preferred, so **Spherical Centroidal Voronoi Tessalation** (SCVT) [45, 46] is applied under this situation.

In free space, the draging force needed to move the ball with translatonal velocity $\mathbf{U}$ in the Stokes flow is $\mathbf{F} = 6\pi\mu\mathbf{U}a$, where μ is the fluid dynamic viscosity ($\mu = 1$ in our case) and a is the radius of the ball. However, with the existence of the wall, the dragging force will change. Following [31], a dimensionless force $\mathbf{F}^* = \frac{\mathbf{F}}{6\pi\mu\mathbf{U}a}$ will be used to analyze results.

Ball moving parallel to the wall

Table 4.2 and table 4.4 show the results from the method of regularized Stokeslet with images incoporated with SCVT, and table 4.1 and table 4.3 are the results taken from paper [31]. The gap size d is the distance from the center of the ball to the wall. Comparing table 4.1 with table 4.2, we can see that the results are almost the same. Thus, those two distributions of the points on the sphere make little difference in the results. Moreover, in order to make it convergent, a finer discretization is required especially when the ball is quite close to the wall.

d/a	Gap size	F^* from polar coordinate				F^* [42]
		S = 468(h = 0.0161)	S = 812(h = 0.0124)	S = 1486 (h = 0.00920)	S = 2718 (h = 0.0068)	
11013.2	1101.22	0.9933	0.9960	0.9980	0.9991	1.0000
10.0677	0.90677	1.0515	1.0545	1.0567	1.0580	1.0591
3.7622	0.27622	1.1644	1.1681	1.1708	1.1725	1.1738
1.5431	0.05431	1.5459	1.5537	1.5595	1.5632	1.5675
1.1276	0.01276	2.0614	2.0851	2.1056	2.1205	2.1515
1.0453	0.00453	2.4226	2.4621	2.5007	2.5007	2.6475
1.0050	0.00050	3.6581	3.4548	3.3999	3.3945	3.7863

Table 4.1: Non-dimensional forces of sphere moving along the wall with radius a = 0.1. S is the number of points on the sphere.

d/a	Gap size	F^* from Spherical Centroidal Voronoi Tessalation				F^* [42]
		S = 468(h = 0.0161)	S = 812(h = 0.0124)	S = 1486 (h = 0.00920)	S = 2718 (h = 0.0068)	
11013.2	1101.22	0.9935	0.9962	0.9981	0.9992	1.0000
10.0677	0.90677	1.0518	1.0547	1.0568	1.0581	1.0591
3.7622	0.27622	1.1647	1.1684	1.1710	1.1726	1.1738
1.5431	0.05431	1.5461	1.5540	1.5598	1.5635	1.5675
1.1276	0.01276	2.0581	2.0843	2.1057	2.1208	2.1515
1.0453	0.00453	2.4103	2.4566	2.4991	2.5322	2.6475
1.0050	0.00050	3.2826	3.2998	3.3373	3.3593	3.7863

Table 4.2: Non-dimensional forces of sphere moving along the wall with radius a = 0.1. S is the number of points on the sphere.

Ball moving perpendicular to the wall

Table 4.3 shows the results by using the spherical coodinate [31], and table 4.4 shows the results from the Spherical Centroidal Voronoi Tessalation. Althogh the results in both ways do not appear to be close to the asymptotic value F^* when the distance between the ball and the infinite wall is too close (Gap size equal to $d = 0.00050$), both results are reasonable since the gap size is smaller than the blob size δ. To obtain a closer result, a finer discretization is necessary.

d/a	Gap size	F^* from polar coordinate				F^* [43, 44]
		S = 468(h = 0.0161)	S = 812(h = 0.0124)	S = 1486 (h = 0.00920)	S = 2718 (h = 0.0068)	
11013.2	1101.22	1.0240	1.0187	1.0142	1.0108	1.0000
10.0677	0.90677	1.1556	1.1488	1.1431	1.1388	1.1253
3.7622	0.27622	1.4605	1.4497	1.4408	1.4341	1.4129
1.5431	0.05431	3.2441	3.1952	3.1557	3.1266	3.0361
1.1276	0.01276	10.2872	10.0943	9.9413	9.8021	9.2518
1.0453	0.00453	19.7071	19.4680	20.2478	21.2626	23.6605
1.0050	0.00050	2010.4400	736.6270	326.6780	180.3810	201.8640

Table 4.3: Non-dimensional forces of sphere moving perpendicular to the wall with radius a = 0.1. S is the number of points on the sphere.

d/a	Gap size	F^* from Spherical Centroidal Voronoi Tessalation				F^* [43, 44]
		S = 468(h = 0.0161)	S = 812(h = 0.0124)	S = 1486 (h = 0.00920)	S = 2718 (h = 0.0068)	
11013.2	1101.22	1.0240	1.0187	1.0142	1.0108	1.0000
10.0677	0.90677	1.1556	1.1487	1.1431	1.1388	1.1253
3.7622	0.27622	1.4604	1.4496	1.4408	1.4308	1.4129
1.5431	0.05431	3.2409	3.1938	3.1552	3.1264	3.0361
1.1276	0.01276	9.9416	9.9421	9.8914	9.7859	9.2518
1.0453	0.00453	17.9657	18.3139	19.5678	20.8616	23.6605
1.0050	0.00050	496.8323	353.3202	236.4403	146.7698	201.8640

Table 4.4: Non-dimensional forces of sphere moving perpendicular to the wall with radius a = 0.1. S is the number of points on the sphere.

4.3.3 Numerical results

In this section, we use the cylindrical helical tube to study the effect of the nearby wall by applying the method of regularized Stokeslets with images. The baseline circle of the helical tube here is located on the y-z plane as introduced at the beginning of this section. Models such as helical ring (a helical tube with tube radius $r_h = 0$) or circle (a helical tube with tube radius $r_h = 0$ and amplitude $R = 0$) are used to distinguish different types of effects. The distance d is the distance between the center of the helical ring and the infinite wall. The effect of the infinite wall on the motion of the helical ring, treated as a free swimmer, will be shown numerically.

Effects from the wall

The helical ring, which is the helical tube with the tube radius $r_h = 0$, is forced to move in the x-direction with an uniform translational velocity $\mathbf{U} = 1$. Without the wall, the helical ring will experience a total dragging force $F^* = 6.3358$ and a total torque $\tau^* = -7.7906e - 02$ in x direction and zero in the other two directions for both force and torque. With the wall from different distances, the total force F and

the total torque τ in y and z diretions are still zeros. Figure 4.8 shows that both the relative change of the total force with respect to F^* in x-direction, which is defined as $\frac{F-F^*}{F^*}$ and the relative change of the total torque in x direction, which is defined as $\frac{\tau-\tau^*}{\tau^*}$, decrease to zero as the distance between the helical ring and the wall increases. If the helical ring moves in the negative x direction, the absolute value of the relative change of the dragging force and of the total torque will be shown the same as the figure 4.8(a) and the figure 4.8(b). Thus, the existence of the wall increases not only the magnitude of the dragging force, but also the torque magnitude. In other words, the wall shows a baffling effect on the moving helical ring whether going toward or away from the wall. Applying the non-linear regression fit to both cases with the model function $y = \frac{1}{ax+b}$ by using **nlinfit** in MATLAB, $\hat{a} = 2.3077$ and $\hat{b} = -0.0123$ for the relative dragging force, and $\hat{a} = 2.2670$ and $\hat{b} = 0.2833$ for the relative total torque. All their variances are less than $4e-4$ and mean square error (mse) is approximately $1e-5$ in both cases. Figure 4.8(a) and figure 4.8(b) show that the model fits both data very well, which imply that the total force and the total torque in toroidal glider case are decreasing with respect to the distance at a rate approximately equal to -1. When the model function $y = \frac{1}{ax^c+b}$ is selected, then under the best fit, the estimate of the power $\hat{c}$ is around 1.1, which is close to 1. The decreasing rate found in this case is different from the quadratically decreasing to the distance between the center of the sphere to the wall when studying the sphere moving near the wall [31]. For easily reference in the future, we call the increased drag force and torque here as "**self-induced force**" and "**self-induced torque**".

In parallel motion of the helical ring, say in z direction (normal is in the z direction too), without the infinite wall, the forces on the helical ring perform not only the role of dragging it with drag F^* but also of preventing it from rotation with
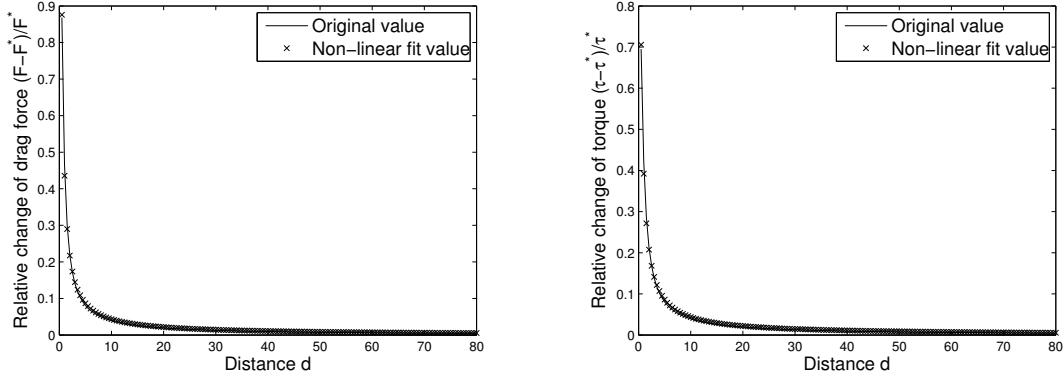
(a) The relative total force, $\frac{F-F^*}{F^*}$, is plotted with respect to the distance d.

(b) The relative total torque, $\frac{\tau-\tau^*}{\tau^*}$, is plotted against the distance d.

Figure 4.8: The helical ring is in perpendicular motion to the wall. The relative total force and the relative total torque are shown with respect to the distance between the helical ring and the infinite wall. Both decrease when the distance increases. The values with marker 'x' are obtained by the non-linear regression fit with model $y = \frac{1}{ax+b}$.

torque τ^* in the z direction. With the existence of the wall, the dragging force (z component) needed to maintain the uniform translation increases in a way similar to the figure 4.8(a) reciprocally corresponding to the distance d, and the torque required to prevent the rotation of the helical ring (only with z component) increases the same as shown in figure 4.8(b). This is easy to explain that the drag and the torque here are the self-induced drag and self-induced torque. One interesting thing is the total force and the torque are not pointing to z-direction exactly. This phenomemon implies the existence of the wall will produce the translation and the rotation if the helical ring moves in a direction parallel to the wall. In order to understand the force preventing the translation and the torque preventing the rotation, both of which are produced by the exsistence of the wall, we consider a more symmetric idealized helical ring with amplitude $R = 0$ and radius of centerline $r_c = 1$. This idealized helical ring is actually a circle.

In perpendicular motion of a circle, the total torque is zero everywhere, and the dragging force F in x direction is decreasing approximately reciprocally with respect to the distance, which is the same as the conclusion to the self-induced force. In the motion with the circle plane parallel to the wall, the torque in the y direction is produced (see figure 4.9(a)). Figure 4.9(b) shows the excellent match of the numerical datum and the non-linear regression approximation with model $y = \frac{a}{x^2+bx+c}$. This implies that the magnitude of the torque is decreasing at the rate of -2 with respect to the distance between the center of the circle and the wall. From the setting of the experiment, the existence of the wall does not change the symmetry of the object with respect to the y axis. The torque in the y-direction is created only because of the movement of the circle in the z-direction with the existence of the wall. It is because of the different gap distance to the wall and to infinity, which we call it "**Gap toruqe**". In the other way around, the rotation in y-axis will produce a drag force in the z-direction, and this drag force will be quadratically proprotional to the distance between the center of the object and the wall. In the same manner, let's called it "**Gap drag**". Thus, "Gap drag" and "gap torque" are formed because of the introduction of the infinite wall into the system. They usually are perpendicular to the rotation and the translaton in the wall plane. Their magnitudes are affected by the distance between the wall in a quadratic way.

What we know now is the existence of the wall baffles the translation of the swimmer in any direction 4.8(a) at the rate close to -1. The closer the swimmer to the wall, the more impediment the wall exerts. This impediment reflects in the reduction of the magnitude of the velocity. If the swimmer has a tendency to rotate in a certain direction 4.8(b), the wall intensifies the rotational tendency at a rate close to -1, which makes it harder to keep the object unrotated. Moreover, the wall
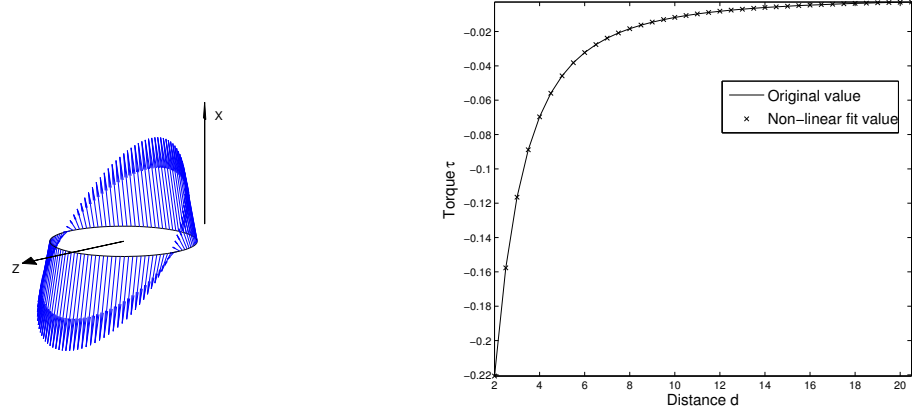
(a) The force profile. The x direction is plotted pointing upward, and the black arrow shows the moving direction of the circle, which is the z axis. The blue arrow represents the force.

(b) The numerical data (solid line) is plotted with comparison of approximation value from non-linear regression with model $y = \frac{a}{x^2+bx+c}$.

Figure 4.9: Parallel motion of a circle in the z direction. From the symmetry of the force profile (a), the circle has a tendency to rotate about the y-direction. The figure (b) shows that the magnitude of the torque is inverserly proportional to the square of the distance d from the center of the circle to the wall.

produces a torque on the plane parallel to the wall and in the direction perpendicular to the moving direction parallel to the wall (see figure 4.9(a)). This created torque is proportional to the magnitude of the translational velocity on that plane, but inversely proportional to the square of the distance from the center of the object to the wall (see figure 4.9(b)). So is the drag force created by a torque in the plane parallel to the wall. The **self-induced force** from the wall and the **self-induced torque** are reciprocally proportional to the distance between the wall and the centere of the object. However, the **gap torque** and the **gap drag** are quadratically proportional to the reciprocal of the distance.

Let's go back to the discussion of the motion of the helical ring. If the helical ring is pulled in x direction (its normal vector is in the x-direction, and remember that the given wall is perpendicular to the x-axis), the helical ring will translate only

in x direction and rotate only about the x-axis. However, if pulled in the z-direction (normal vector is in the z-direction), it not only translates in z-direction, rotates about the z-axis, but also translates and rotates about y axis. The translation in y-axis comes from the rotation in z-axis. The rotation along the y-axis is generated by the translation in z direction resulting from the effect of the wall. Interestingly, there are net force and net torque in x-direction observed in the numerical results. These changes purely come from the shape of the immersed object because no observation of these forces and torques for a symmetric objects were observed. Let's call them "**form drag**" and "**form torque**" respectively. Apply the non-linear regression fit with the model

$$y = \frac{a}{x^3 + bx^2 + cx + d},$$

we find that this model fits extremely well with MSE less than 10^{-15}. The comparison between the numerical results in form drag and form torque with the non-linear regression fits are shown in figure 4.10. The inverse of the form drag and the inverse of the form torque are related to the distance between the center of the object and the wall in a cubic way. In fact, in each direction, the drag (self-induced, gap) and the torque (self-induced or gap) will more or less be affected by the form drag and the from torque, however, they are much smaller than the other two in magnitude. Therefore, in the non-linear regression fit, no cubic term is observed in the given models.

Above all, we find that the wall affects the motion of an immersed object in several ways: self-induced force, self-induced torque, gap force, gap torque, even form drag and from torque. All of them increase in magnitude as the object gets closer to the wall. The increase of the self-induced force implies it is harder to drag the object with constant translational velocity. The increase in all others means a
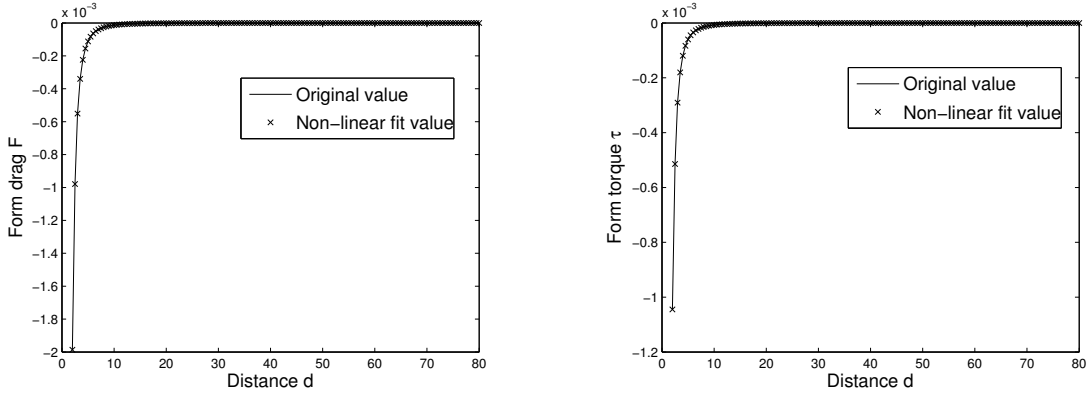
(a) The form drag (solid line) is plotted with respect to the distance between the center of the helical ring and the wall. The stars show the values from the non-linear regression fit.

(b) The form torque (solid line) is plotted with respect to the distance between the center of the helical ring to the wall. The stars show the values from the non-linear regression fit.

Figure 4.10: Parallel motion of a helical ring in the z direction. The form drag (a) and form torque (b) in the x direction are shown here. Non-linear regression with a model of $y = \frac{a}{x^3+bx^2+cx+d}$ is used here to estimate the rate of decreasing. Both figures show that their magnitude are inversely proportional to the cubic of the distance d from the center of the circle to the wall.

larger tendency to rotate or translate in certain directions. The self-induced force or torque does not change the moving direction. The direction of the gap force and the direction of the gap torque are easily predicted since they are parallel to the wall and perpendicular to the rotation axis and the translation direction on the wall respectively. However, the form drag and torque are difficult to predict because it comes from the change of its shape.

Motion of the helical tube

From the conclusion in the toroidal glider part, if the free swimmer is moving in a certain direction, we expect to see the reduction in magnitude of the translational velocity since the wall has baffling effect on the translational velocity. We also expect an increment of the rotational velocity in magnitude or the creation of the rotational velocity and translational velocity when comparing to the case without the wall. Fig-

ure 4.11 shows that the transaltional velocity and the rotational velocity change with respect to the distance between the center of the helical tube and the wall when the helical tube is moving in the positive x direction. Only translational velocity and rotational velocity in the x-direction are observed. In figure 4.11(a), the translational velocity is proportional to the reciprocal of the distance. Figure 4.11(b) shows that the rotational velocity is decreasing reciprocally with respect to the distance.
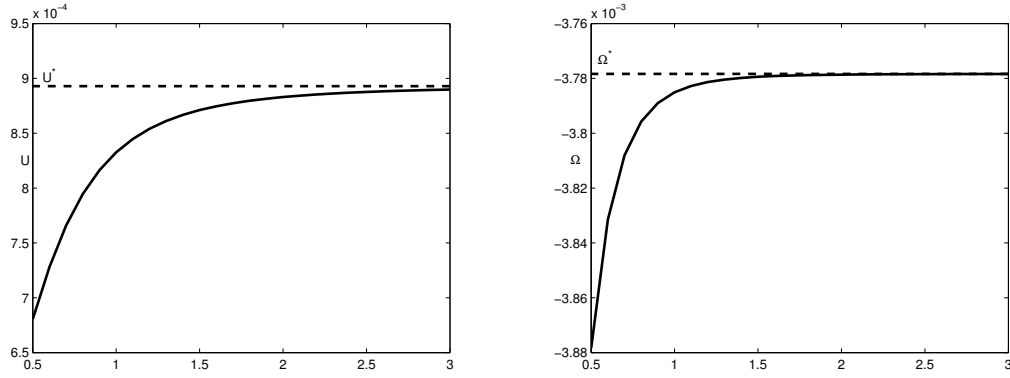
(a) The translational velocity, U, of the free swimmer with a wall is plotted compared with the velocity, U^*, of the swimmer without a wall.

(b) The rotational velocity, Ω, of the free swimmer with a wall is plotted compared with the rotational velocity Ω^* of the swimmer without a wall

Figure 4.11: The x-axis prepesents the distance between the center of the helical ring and the wall. The transaltional velocity U increases as the free swimmer moves away from the wall, but the magnitude of the rotational velocity Ω deceases.

When the helical ring moves in the z-direction with the wall parallel to the y-z plane, then from the discussion in toroidal swimmer, this movement will produce forces and torques in both x and z directions. Thus, as a force free swimmer, the helical tube will experience translations and rotations in both x and z direction besides in y direction.

Chapter 5

Summary

In this thesis we consider the hydrodynamic interaction between two toroidal swimmers with surface tangential velocity by applying the method of regularized Stokeslets. The torus as a toroidal swimmer was first introduced by G. I. Taylor in 1952 and then was discussed by Purcell in 1977 with a swimming mechanism with prescribed surface tangential velocity. The underlying mechanism of propulsion comes from the momentum squeezing the fluid through a hole. As a free swimmer, the torus must exert zero net force and zero net torque instantaneously. This results in a rigid translation and rotation of the toroidal swimmer in Stokes flow. Note that, because of symmetry, a single torus in an infinite three-dimensional domain would experience zero rotation, which is confirmed in our results. Moreover, we have validated our numerical method by comparing our results to the analytical solution in [12] and reproduce the numerical results in [7].

It is demonstrated that two tori, initially placed in tandem, stay in tandem. The perturbation of two counter-rotating tori, face to face in tandem, will rotate in the same direction and moves towards each other with a tendency of alignment. However, the perturbation of two co-rotating in tandem tori poses different results: moving apart, translation without rotation, periodic movement or even collision. When two

tori are initially placed abreast, we find that they rotate with opposite rotational velocities and move towards each other with mirror-symmetric translational velocities. It also has been shown that pairs of tori in 3D experience trajectories similar to pairs of finite vortex dipoles in 2D. Moreover, we have examined the overall swimming velocity of a single torus and the torus coupled with a sphere placed at its center. We find that a torus coupled with a sphere inside moves forward faster than a single torus model, and no rotional velocities were observed in either model. The efficiency of a torus with sphere is larger than that of a single torus with no centered sphere.

In the study of the effect of the nearby wall, we used a model of waving cylindrical ring introduced in [7]. Several simple experiments have been studied numerically and we show that three types of drag forces and torques are introduced to the motion of the immersed object: self-induced drag and torque, gap drag and torque, and form drag and torque. They depend on the distance between the immersed object to the wall in different rates. The inverse of the self-induced drag and torque is linearly dependent on the distance. The inverse of the gap drag and torque is quadratically proportional to the distance. However, the form drag and torque decrease at a cubic rate with respect to the distance. All these show that the wall has a baffling effect on the motion of the immersed object.

Chapter 6

Future work

Interaction between multiple microorganisms and surface interactions

One natural extension of the work I have done is to examine the interaction between multiple tori and boundaries. Spermatozoa cells have showed a preference for swimming near surfaces [47]. Surface accumulation behavior and colonial dynamics of multiple microorganism [48] will be studied with multiple tori.

Nutrient uptake by swimming tori

I propose to couple the fluid dynamic model of a swimming tori to the advection, diffusion and uptake of a chemical species. Within the context of the method of regularized Stokeslets, we will choose a particle strength exchange approach to model the scalar chemical equation [49]. The concentration of nutrient will be considered as "particles", the movement of which will be governed by the advection-diffusion-reation equation. We may also apply a torque to the tori to have their motion directed, the phenomenon of which is called chemotaxis, and will also be pushed by the flow of the fluid [50].

Inclusion of 'sensory' feedback

Our current model of toroidal swimming imposes a tangential velocity that does not

depend upon the state of the coupled system. For instance, as two tori approach each other, or as a torus approaches a wall, the input tangential velocities are not altered. We propose to develop a model whereby the actuation of the torus depends upon its proximity to other objects or on its current power expenditure. In this manner, we can choose feedback models that optimize swimming in some way.

Interaction of toridal swimmers in non-zero Reynolds number flow

From a purely fluid dynamic point of view, I propose to examine how the inclusion of inertia would affect the dynamics of a toroidal swimmer. An immersed boundary method [51] will be applied to study them, and the simulation under different Reynolds number will be analyzed.

Model of dinoflagellate

A real dinoflagellate has two flagella, a transverse helical shape wrapping around a notched sphere and a longitudinal one shaped like a tail. One goal of our collaboration with Hoa Nguyen is to develop a whole model of the dinoflagelalte, that employs realistic geometry. The movement and efficiency of the new model will be studied.

References

[1] Taylor, F. J., "Non-helical transverse flagella in dinoflagellates", *Phycologia* **14** (1975), no. 1, 45–47.

[2] Leblond, P. H. and F. J. Taylor, "The propulsive mechanism of the dinoflagellate transverse flagellum reconsidered", *BioSystems* **8** (1976), no. 1, 33–39.

[3] Gaines, G. and F. J. Taylor, "Form and function of the dinoflagellate transverse flagellum", *J. Protozool* **32** (1985), no. 2, 290–296.

[4] Cachon, M., et al., "Dinoflagellate flagella adopt various conformations in response to different needs", *Biology of the Cell* **71** (1991), no. 1-2, 175–182.

[5] Fenchel, T., "How dinoflagellates swim", *Protist* **152** (2001), no. 4, 329–338.

[6] Miyasaka, I., et al., "Functional roles of the transverse and longitudinal flagella in the swimming motility of prorocentrum minimum (dinophyceae)", *The Journal of Experimental Biology* **207** (2004), no. 17, 3055–3066.

[7] Nguyen, H., et al., "The action of waving cylindrical rings in a viscous fluid", *J. Fluid Mech.* **671** (2011), 574–586.

[8] Taylor, G. I., "The action of waving cylindrical tails in propelling microscopic organisms", *Proceedings of the Royal Society of London. Series A, Mathematical and Physical Sciences* **211** (1952), no. 1105, 225–239.

[9] Purcell, E. M., "Life at low Reynolds number", *American Journal of Physics* **45** (1977), no. 1, 3–11.

[10] Chwang, A. T. and W.-S. Hwang, "Rotation of a torus", *Phys. Fluids A* **2** (1990), no. 8, 1309–1311.

[11] Thaokar, R. M., H. Schiessel, and I. M. Kulic, "Hydrodynamics of a rotating torus", *Eur. Phys. J. B* **60** (2007), 325–336.

[12] Leshansky, A. M. and O. Kenneth, "Surface tank treading: Propulsion of purcell's toroidal swimmer", *Physics of Fluids* **20** (2008), 063104.

[13] Kulic, I., R. Thaokar, and H. Schiessel, "Twirling DNA rings–Swimming nano motors ready for a kickstart", *Europhys. Lett.* **72** (2005), no. 4, 527–533.

[14] Dewitz, J., "Ueber gesetzm assigkeit in der ortsver anderung der spermatozoen und in der vereinigung derselben mit dem ei", *Archiv f ur der Gesellschaft Physiologisch* **38** (1886), 358–385.

[15] Rothschild, L., "Non-random distribution of bull spermatozoa in a drop of sperm suspension nature london", *The Mathematical Scientist* **198** (1963), 1221–1222.

[16] Smith, D. J. and J. R. Blake, "Surface accumulation of spermatozoa: A fluid dynamic phenomenon", *The Mathematical Scientist* **34** (2010), no. 2, 74–87.

[17] Janosi, I. M., et al., "Chaotic particle dynamics in viscous flows: The three-particle stokeslet problem", *Phys. Rev. E* **56** (1997), 2858–2868.

[18] Ishikawa, T., M. P. Simmonds, and T. J. Pedley, "Hydrodynamics interaction of two swimming model micro-organism", *J. Fluid Mech.* **568** (2006), 119–160.

[19] Ishikawa, T. and M. Hota, "Interaction of two swimming paramecia", *The Journal of Expeimental Biology* **209** (2006), 4452–4463.

[20] Batchelor, G. K., "The stress system in a suspension of force-free particles", *J. Fluid Mech.* **41** (1970), 545–570.

[21] Brady, J. F. and G. Bossis, "Stokesian dynamics", *Annu. Rev. Fluid Mech.* **20** (1988), 111–157.

[22] Claeys, I. L. and J. F. Brady, "Lubrication singularities of the grand resistance tensor for two arbitrary particles", *PhysicoChemi. Hydrodyn.* **11** (1989), 261–293.

[23] Claeys, I. L. and J. F. Brady, "Suspensions of prolate spheroids in stokes flow. part 1. dynamics of a finite number of particles in an unbounded fluid", *J. Fluid Mech.* **251** (1993), 411–442.

[24] Durlofsky, L., J. F. Brady, and G. Bossis, "Dynamics simulation of hydrodynamically interacting particles", *J. Fluid Mech.* **180** (1987), 21–49.

[25] Nott, P. R. and J. F. Brady, "Pressure-driven flow of suspensions: simulation and theory", *J. Fluid Mech.* **275** (1994), 157–199.

[26] Pozrikidis, C., *Boundary integral and sigularity methods for linearized viscous flow*, Cambridge University Press, 1992.

[27] Thaokar, R. M., "Hydrodynamics interaction between two rotating tori", *Eur. Phys. J. B* **61** (2008), 47–58.

[28] Cortez, R., "The method of regularized Stokeslets", *SIAM J. SCI. COMPUT.* **23** (2001), no. 4, 1204–1225.

[29] Cortez, R., L. Fauci, and A. Medovikov, "The method of regularized Stokeslets in three dimensions: Analysis, validation, and application to helical swimming", *Physics of Fluid* **17** (2005), no. 3, 031504.

[30] Pozrikidis, C., *Introduction to theoretical and computational fluid dynamics*, Oxford University Press, 2011.

[31] Ainley, J., et al., "The method of images for regularized Stokeslets", *Journal of Computational Physics* **227** (2005), 4600–4616.

[32] Blake, J. R., "A note on the image system for a Stokeslet in a no-slip boundary", *Proc. Camb. Philos. Soc.* **70** (1971), 303.

[33] Tchieu, A. A., E. Kanso, and P. K. Newton, "The Finite-dipole dynamical system", *Proceedings of the Royal Society A: Mathematical, Physical and Engineering Sciences* **468** (2012), no. 2146, 3006–3026.

[34] Batchelor, G., *An introduction to fluid dynamics*, Cambridge Mathematical Library, 2000.

[35] Johnson, R. E. and T. Y. Wu, "Motion of a slender torus", *J. Fluid Mech.* **95** (1979), 263.

[36] Purcell, E. M., "The efficiency of propulsion by a rotating flagellum", *Proc. Natl. Acad. Sci. U.S.A.* **94** (1997), 11307.

[37] Wiggins, C. H. and R. E. Goldstein, "Flexive and propulsive dynamics of elastica at low Reynolds numbers", *Phys. Rev. Lett.* **80** (1998), 3879.

[38] Becker, L. E., S. A. Koehler, and H. A. Stone, "On self-propulsion of micro-machines at low Reynolds number: Purcell's three-link swimmer", *J. Fluid Mech.* **490** (2003), 15.

[39] Tam, D. and A. E. Hosoi, "Optimal stroke patterns for Purcell's three-link swimmer", *Phys. Rev. Lett.* **98** (2007), 068105.

[40] Shapere, A. and F. Wilczek, "Geometry of self-propulsion at low Reynolds number", *J. Fluid Mech.* **198** (1989), 557.

[41] Avron, J. E., O. Gat, and O. Kenneth, "Optimal swimming at low Reynolds numbers", *Phys. Rev. Lett.* **93** (2004), 186001.

[42] O'Neill, M. E., "A slow motion of viscous liquid caused by a slowly moving solid sphere", *Mathematika* **11** (1964), 67–74.

[43] Brenner, H., "The slow motion of a sphere through a viscous fluid towards a plane surface", *Chem. Eng. Sci.* **16** (1961), 242–251.

[44] Cooley, M. and M. O'Neill, "On the slow motion generated in a viscous fluid by the approach of a sphere to a plane wall or stationary sphere", *Mathematika* **16** (1969), 37–49.

[45] Du, M., V. Faber, and M. Gunzburger, "Centroidal voronoi tessellations: Applications and algorithms", *SIAM Review* **41** (1999), no. 4, 637–676.

[46] Du, Q., M. D. Gunzburger, and L. Ju, "Constrained centroidal voronoi tessellations for surfaces", *SIAM J. Sci. Comput.* **24** (1999), no. 5, 1488–1506.

[47] Smith, D. J., et al., "Human sperm accumulation near surfaces: a simulation study", *J. Fluid Mech.* **621** (2009), 289–320.

[48] Lushi, E. and C. S. Peskin, "Modeling and simulation of active suspensions containing large numbers of interacting micro-swimmers", *Computers and Structures* **122** (2013), 239–248.

[49] Hamlington, K. I., et al., "Evaluation of grid-based and grid-free methods to model microchannel transport-reaction", *SIAM J. Sci. Comput.* **35** (2013), no. 4, 846–867.

[50] Hopkins, M. M. and L. J. Fauci, "A computational model of the collective fluid dynamics of motile micro-organisms", *J. Fluid Mech.* **455** (2002), 149–174.

[51] Peskin, C. S., "The immersed boundary method", *Acta Numerica* (2002), 479–517.

[52] Majumdar, S. R. and M. E. O'Neill, "On axisymmetric flow past a torus", *Z. Angew. Math. Phys.* **28** (1977), 541.

Biography

Jianjun Huang was born in 1983 in Putian, Fujian, China. He attended the School of Mathematics and Applied Mathematics at Xiamen University where he studied applied mathematics. In 2006 he received his Bachelor of Science in Mathematics and Applied Mathematics. In the same year he enrolled in a Master of Mathematics program at Xiamen University specializing in Partial Differential Equations with Dr. Zhong Tan, and received his Master of Science in 2009 with the thesis, "Concentration Phenomenon of Variational Problem". Jianjun enrolled in the Ph.D. program at Tulane University in 2009. He has been working on applied mathematics and biological fluid dynamics with his advisor, Dr. Lisa Fauci since 2012 in modeling microorganisms swimming in low Reynolds number flow. During his study at Tulane, he was thoroughly trained in theoretical partial differential equations and theoretical and computational fluid dynamics. He also has extensive experience in visualization software VisIt and parallel programming with C++.